2013

# Bioinspired synthesis and characterization of organic/inorganic nanocomposite materials

Xunpei Liu
*Iowa State University*

# Bioinspired synthesis and characterization of organic/inorganic nanocomposite materials

by

Xunpei Liu

A dissertation submitted to the graduate faculty
In partial fulfillment of requirements for the degree of

DOCTOR OF PHILOSOPHY

Major: Chemical Engineering

Program of Study Committee

Surya K. Mallapragada, Major Professor
Monica H. Lamm
Jennifer Heinen
Mufit Akinc
Klaus Schmidt-Rohr

Iowa State University

Ames, Iowa

2013

# Table of Contents

# List of Figures

# List of Tables

# Acknowledgements

I would like to take this opportunity to express my sincere appreciation to all the people who have inspired and helped me throughout my PhD study. Without their supports, I could not finish this.

First of all, I would like to thank my major professor, Surya Mallapragada. Her enthusiastic, direction and encouragement have been a powerful source for my PhD study. I also sincerely thank my program of study committee members, Monica Lamm, Jennifer Heinen, Mufit Akinc, and Klaus Schmidt-Rohr, for their continuous support and valuable suggestions.

Next, I wish to thank my family members: my husband, Feng Jia, who has accompanied me for college, master and PhD study for the past ten years as a classmate and best friend; my parents and my younger sister, who have been always supportive, and allow me to pursue my dream at a long distance. I am so lucky to have them aside.

My project is a multi-discipline collaborative project, and I really appreciate our collaborative professors, Prof. Mufit Akinc, Prof. Klaus Schmidt-Rohr, Dr. Tanya Prozorov, Prof. Marit Nilsen-Hamilton, and Dr. David Vaknin. They have provided many unique opinions and suggestions for my research, which have helped me learned more knowledge in different research field and inspired me to explore more on our project. I also thank my colleagues on this project, Honghu Zhang, Xing Ma, Shuren Feng, Qinwen Ge, German Parada, Dr. Lijun Wang, Dr. Yanyan Hu, and Dr. Wenjie Wang. I really appreciate their help and hard work on this project, as well. I also want to thank the group members from Prof. Mallagragada's group: Feng Jia, Dr. William Colonna, Justin Adams, Dr. Bingqi Zhang, Dr. Robert J Lipert, Dr. Mustafa Marti, Anup Dutt Sharma, Metin UZ and Dr. Natia Ochkhikidze and Dr. Vikash Malik.

I also would like to thank the faculty and staff members as well as the friends in the chemical and biological engineering department, because they have made me feel like to be part of the whole family. I really enjoyed the happy and peaceful life in Ames.

# Abstract

In Nature, hybrid materials with hierarchical structure are formed by biomineralization of organic macromolecules that act as templates for the nucleation and/or growth of the inorganic component. The building blocks of the natural organic macromolecules provide the template architectures that result in chemical and morphological diversity in the inorganic phases. Inspired by the formation of biominerals in living organisms, novel organic-inorganic hybrid materials have been designed and developed by biomimetic routes. There is a growing interest in using synthetic polymers, engineered proteins, and various polymer-based hybrid architectures as templates for bioinspired synthesis.

In this work, we have used amphiphilic block copolymers as well as block copolymer-protein conjugates that undergo hierarchical self-assembly to form nanoscale micelles and macroscale gels as templates for controlled nanocomposite formation within the polymeric matrix. The amphiphilic block copolymers that were generated based on Pluronics are unique systems that can reversibly self-assemble into macroscale elastic solids in solution, based on pH and temperature changes. The efforts were focused on three systems—calcium phosphate nanocomposites, zirconia nanocomposites, and magnetic nanocomposites.

We have developed a robust method with control over the formation as well as placement of an inorganic phase in the nanocomposite structure, for a variety of different inorganic nanoparticles, such as calcium phosphate, zirconia and magnetic nanoparticles. The future work will be focused on using biominerlization proteins to create functional dynamic magnetic materials and nanostructures both in solution and on surfaces.

# Chapter 1 General Introduction

## 1.1 Introduction

In Nature, hybrid materials with hierarchical structure, such as bone,[1] shell,[2] and sea sponge skeleton,[3] are formed by biomineralization of organic macromolecules that act as templates for the nucleation and/or growth of the inorganic component. The building blocks of the natural organic macromolecules provide the template architectures that result in chemical and morphological diversity in the inorganic phases that they form.[4,5] Calcium carbonate,[6,7] calcium phosphate,[8,9] silica,[10,11] and iron oxide,[12] etc. are synthesized by organisms from simple precursors under mild reaction conditions, resulting in highly ordered hierarchical structures, ranging from the nano-level to the macro-level. Inspired by the formation of biominerals in living organisms, novel organic-inorganic hybrid materials have been designed and developed by biomimetic routes. These materials have the potential to be used in catalysis, biosensing, optics, electronics, medicine and as structure-supporting materials.[13–16] Synthetic polymers,[17] polysaccharides,[18] peptides,[19] DNA molecules,[20] and proteins[21] have been used in bio-inspired syntheses as matrices, scaffolds and templating agents.

There is a growing interest in using synthetic polymers, engineered proteins, and various polymer-based hybrid architectures as templates for bioinspired synthesis.[22–24] Polymer templates have the advantage of molecular-level control and exhibiting macroscale hierarchical order.[25] Block copolymers, which consist of two or more covalently bonded single polymer blocks with different physical and chemical properties, have attracted researchers' attention as templates for the controlled synthesis of multi-scale hybrid inorganic materials.[26–28] Block copolymers have the capability of self-assembling into a variety of microdomain morphologies (lamellae, hexagonally packed cylinders, spheres, etc.) in both solution and bulk. These structures usually fall in the range of a few nanometers up to several micrometers.[26,28,29] Many block copolymers undergo

micellization and gelation processes in solvent media. The micellization process in block copolymers mainly depends on the critical micelle temperature (CMT) and the critical micelle concentration (CMC). Self-assembly of block copolymers will occur when the CMT and the CMC are reached.[26] Recent advances in living radical polymerization methods have allowed for the facile synthesis of block copolymers from functional monomers, and for adding functional blocks to the existing block copolymers. Therefore, desired functional block copolymers can be built to control the interfaces with very different chemical nature, polarity, and cohesion energy.[30]

Self-assembling, nontoxic, biocompatible, and inexpensive block copolymers are under investigation for use as templates for biomineralization. Pluronics belong to this category of polymers. They are a family of amphiphilic triblock copolymers with hydrophilic polyethylene oxide (PEO) end segments, and a hydrophobic polypropylene oxide (PPO) mid-segment.[31] Pluronics exhibit reversible thermoresponsive micellization and gelation.[32] The hydrophobic segments pack together to form the inner cores of micelles, driven by the hydrophobic effect. The hydrophilic parts, however, preferentially dissolve in water. The balance between these forces drives the formation of micelles in aqueous solution.[33] The CMC and CMT decrease with an increase of PPO content or molecular weight in the copolymer. The CMC of aqueous Pluronic solutions decreases with increasing temperature.[34] Previously in our group, atom transfer radical polymerization (ATRP) was used to add poly(2-diethylaminoethyl methacrylate) (PDEAEM) blocks to each end of triblock Pluronic F127 to obtain an amphiphilic, polycationic pentablock copolymer. This pentablock copolymer retains the thermoresponsive micellization and gelation of the original Pluronic, and has added pH sensitivity from the PDEAEM blocks.[35]

However, the use of synthetic polymer templates alone does not provide enough biological specificity for controlled growth of the inorganic phase. Biomolecules, such as proteins, polypeptides, cellulose, chitosan, and nucleic acids are used to control assembly and formation of

functional organic-inorganic hybrid materials.[7,36–38] Conjugation of synthetic polymers and biomolecules allows combining the structural and functional control of biomolecules with the versatility of synthetic polymer.

In this work, we have used amphiphilic block copolymers as well as block copolymer-protein conjugates that undergo hierarchical self-assembly to form nanoscale micelles and macroscale gels as templates for controlled nanocomposite formation within the polymeric matrix. The amphiphilic block copolymers that were generated based on Pluronics are unique systems that can reversibly self-assemble into macroscale elastic solids in solution, based on pH and temperature changes. The efforts were focused on three systems—calcium phosphate nanocomposites, zirconia nanocomposites, and magnetic nanocomposites.

Calcium phosphates, notably HAp [$Ca_{10}(PO_4)_6(OH)_2$], exhibit many levels of hierarchical structures in bone, from nano to macro scales.[39] Bone is a highly ordered, dynamic, and highly vascularized tissue that exhibits excellent strength, hardness and fracture toughness. It is a biocomposite of 70% mineral (mostly nanoscale calcium phosphate crystals) and 30% organics (including collagen, glycoproteins, proteoglycans, and sialoproteins) by dry weight.[40,41] Nanoscale collagen fibrils are templates for the growth of the calcium phosphate inorganic phase, thereby forming a hierarchically ordered structure with unique properties.

Magnetic nanoparticles of about 50 nm are in great demand for many applications, such as magnetic recording, drug delivery and quantum computing.[42] Magnetotactic bacteria form magnetite nanoparticles *in vivo* with various morphologies.[43] The *magnetospirillum magneticum* strain AMB-1 produces a chain of cuboctahedral magnetite nanocrystals, each surrounded by a lipid bilayer membrane. Several proteins isolated from the magnetosome membranes showed common features in their amino acid sequences, which contain hydrophobic N-terminal and

hydrophilic C-terminal regions. The C-terminal regions in Mms5, Mms6, Mms7, and Mms13 contain clustered carboxyl and hydroxyl groups that bind iron ions. Nano-sized magnetic particles similar to those in magnetotactic bacteria were prepared *in vitro* by chemical synthesis of magnetite in the presence of the protein Mms6.[44] These proteins may be directly involved in biological magnetite crystal formation in magnetic bacteria. We have used Mms6 along with the block copolymers as templates for magnetic nanocomposite synthesis.

Many efforts to synthesize zirconia have been made, because of its applications in catalyst, adsorbents, biosensors, and fuel cells.[45] Templating is one of the most promising methods, because of low cost and mild synthesis conditions. We have developed a bio-inspired bottom-up approach to synthesize zirconia nanocomposite using our unique self-assembled cationic block copolymer as well as block copolymer-lysozyme conjugates as templates in completely aqueous media. Furthermore, removing the organic component of the hybrid material creates high surface area mesoporous zirconia.

## 1.2 Overall Objectives

Biomimetic synthetic routes offer the opportunity to control size, shape, composition, crystal structure, orientation, distribution and hierarchical organization of nanoscale assemblies, which is difficult to achieve using conventional techniques. The objectives of this doctoral work are to design functional templates, and explore biomimetic routes for the development of hierarchically self-assembled unique functional materials suitable for a variety of different applications.

We have designed hierarchically self-assembling polymer templates as well as their conjugates with mineralization proteins and peptides to provide bioinspired templates for hybrid nanocomposites with hierarchical order. We have used the developed templates and the bioinspired synthesis approach to synthesize three different classes of materials: calcium

phosphate nanocomposites, mesoporous zirconia, and magnetic nanoparticles. The synthesized materials were characterized by thermogravimetric analysis (TGA), X-ray diffraction (XRD), transmission electron microscopy (TEM), scanning electron microscopy (SEM), and small angle scattering techniques. Our collaborators have also characterized the materials by surface area measurement and solid state nuclear magnetic resonance (NMR).

### 1.3 Dissertation organization

The thesis is organized into eight chapters. Chapter 2 is a literature review about bioinspired synthesis of organic/inorganic nanocomposites mediated by different biomolecules, which include protein, peptides, DNA and polysaccharides. This chapter has been published as a book chapter in the book "On Biomimetics" (ISBN: 978-953-307-271-5). Chapter 3 is modified from a paper published in *Chemistry of Materials*. It focused on the use of small amounts of citrate in the bioinspired synthesis to control the size of the calcium phosphate nanocrystals in the nanocomposites, similar to what is seen in bone growth. Chapters 4 and 5 are focused on synthesis of mesoporous zirconia templated by cationic pentablock copolymers and block copolymer-lysozyme conjugates. Chapter 4 is focused on the synthesis of the templated mesoporous zirconia formed in completely aqueous media, and has been published in *Science of Advanced Materials*. Chapter 5 is focused on the effects of various parameters, such as temperature, pH and precursor concentration, on the Pluronic-lysozyme templated mesoporous zirconia. Chapter 6 deals with investigation of the biomineralization protein Mms6 found in magnetotactic bacteria, and optimization of the conditions of using this protein to mediate shape and size selective synthesis of magnetite and other magnetic nanocrystals. Chapter 7 is focused on the investigation of Mms6 and its interaction with iron ions in solution. Chapter 8 covers the conclusions and ongoing work of the project.

## References


(1) Buckwalter, J. A.; Glimcher, M. J.; Cooper, R. R.; Recker, R. Bone Biology. *JBJS* **1995**, *77*, 1256–1275. why caps?

(2) Addadi, L.; Joester, D.; Nudelman, F.; Weiner, S. Mollusk Shell Formation: A Source of New Concepts for Understanding Biomineralization Processes. *Chem. Eur. J.* **2006**, *12*, 980–987.

(3) Aizenberg, J.; Weaver, J. C.; Thanawala, M. S.; Sundar, V. C.; Morse, D. E.; Fratzl, P. Skeleton of Euplectella sp.: Structural Hierarchy from the Nanoscale to the Macroscale. *Science* **2005**, *309*, 275 –278.

(4) Andre, R.; Tahir, M. N.; Natalio, F.; Tremel, W. Bioinspired synthesis of multifunctional inorganic and bio-organic hybrid materials. *FEBS Journal* **2012**, *279*, 1737–1749.

(5) Estroff, L. A.; Hamilton, A. D. At the Interface of Organic and Inorganic Chemistry: Bioinspired Synthesis of Composite Materials. *Chemistry of Materials* **2001**, *13*, 3227–3235.

(6) Arias, J. L.; Fernández, M. S. Polysaccharides and Proteoglycans in Calcium Carbonate-based Biomineralization. *Chemical Reviews* **2008**, *108*, 4475–4482.

(7) Zhao, J.; Li, Y.; Cheng, G. Synthesis of CaCO3 crystals using hydroxypropylmethyl cellulose hydrogel as template. *CHINESE SCIENCE BULLETIN* **2007**, *52*, 1796–1801.

(8) Enlow, D.; Rawal, A.; Kanapathipillai, M.; Schmidt-Rohr, K.; Mallapragada, S.; Lo, C.-T.; Thiyagarajan, P.; Akinc, M. Synthesis and characterization of self-assembled block copolymer templated calcium phosphate nanocomposite gels. *J. Mater. Chem.* **2007**, *17*, 1570.

(9) Hu, Y.-Y.; Yusufoglu, Y.; Kanapathipillai, M.; Yang, C.-Y.; Wu, Y.; Thiyagarajan, P.; Deming, T.; Akinc, M.; Schmidt-Rohr, K.; Mallapragada, S. Self-assembled calcium phosphate nanocomposites using block copolypeptide templates. *Soft Matter* **2009**, *5*, 4311.

(10) Bansal, V.; Rautaray, D.; Bharde, A.; Ahire, K.; Sanyal, A.; Ahmad, A.; Sastry, M. Fungus-mediated biosynthesis of silica and titania particles. *J. Mater. Chem.* **2005**, *15*, 2583.

(11) Luckarift, H. R.; Dickerson, M. B.; Sandhage, K. H.; Spain, J. C. Rapid, Room-Temperature Synthesis of Antibacterial Bionanocomposites of Lysozyme with Amorphous Silica or Titania. *Small* **2006**, *2*, 640–643.

(12) Prozorov, T.; Mallapragada, S. K.; Narasimhan, B.; Wang, L.; Palo, P.; Nilsen-Hamilton, M.; Williams, T. J.; Bazylinski, D. A.; Prozorov, R.; Canfield, P. C. Protein-Mediated Synthesis of Uniform Superparamagnetic Magnetite Nanocrystals. *Adv. Funct. Mater.* **2007**, *17*, 951–957.

(13) Drisko, G. L.; Luca, V.; Sizgek, E.; Scales, N.; Caruso, R. A. Template Synthesis and Adsorption Properties of Hierarchically Porous Zirconium Titanium Oxides. *Langmuir* **2009**, *25*, 5286–5293.

(14) Bhushan, B.; Bhushan, B. Biomimetics: Lessons from Nature–an Overview. *Phil. Trans. R. Soc. A* **2009**, *367*, 1445–1486.

(15) Ball, P. Natural strategies for the molecular engineer. *Nanotechnology* **2002**, *13*, R15–R28.

(16) Munch, E.; Launey, M. E.; Alsem, D. H.; Saiz, E.; Tomsia, A. P.; Ritchie, R. O. Tough, Bio-Inspired Hybrid Materials. *Science* **2008**, *322*, 1516–1520.

(17) Kanapathipillai, M.; Yusufoglu, Y.; Rawal, A.; Hu, Y.-Y.; Lo, C.-T.; Thiyagarajan, P.; Kalay, Y. E.; Akinc, M.; Mallapragada, S.; Schmidt-Rohr, K. Synthesis and Characterization of Ionic Block Copolymer Templated Calcium Phosphate Nanocomposites. *Chemistry of Materials* **2008**, *20*, 5922–5932.

(18) Khan, F.; Walsh, D.; Patil, A. J.; Perriman, A. W.; Mann, S. Self-organized structural hierarchy in mixed polysaccharide sponges. *Soft Matter* **2009**, *5*, 3081.

(19) Sarikaya, M.; Tamerler, C.; Schwartz, D. T.; Baneyx, F. Materials assembly and formation using engineered polypeptides. *Annu. Rev. Mater. Res.* **2004**, *34*, 373–408.

(20) Park, D.-H.; Kim, J.-E.; Oh, J.-M.; Shul, Y.-G.; Choy, J.-H. DNA Core@Inorganic Shell. *Journal of the American Chemical Society* **2010**, *132*, 16735–16736.

(21) Amemiya, Y.; Arakaki, A.; Staniland, S. S.; Tanaka, T.; Matsunaga, T. Controlled formation of magnetite crystal by partial oxidation of ferrous hydroxide in the presence of recombinant magnetotactic bacterial protein Mms6. *Biomaterials* **2007**, *28*, 5381–5389.

(22) Dickerson, M. B.; Sandhage, K. H.; Naik, R. R. Protein- and Peptide-Directed Syntheses of Inorganic Materials. *Chemical Reviews* **2008**, *108*, 4935–4978.

(23) Ulijn, R. V.; Woolfson, D. N. Peptide and protein based materials in 2010: from design and structure to function and application. *Chem. Soc. Rev.* **2010**, *39*, 3349.

(24) Das, S. K.; Bhunia, M. K.; Sinha, A. K.; Bhaumik, A. Self-Assembled Mesoporous Zirconia and Sulfated Zirconia Nanoparticles Synthesized by Triblock Copolymer as Template. *The Journal of Physical Chemistry C* **2009**, *113*, 8918–8923.

(25) Yusufoglu, Y.; Hu, Y.; Kanapathipillai, M.; Kramer, M.; Kalay, Y. E.; Thiyagarajan, P.; Akinc, M.; Schmidt-Rohr, K.; Mallapragada, S. Bioinspired synthesis of self-assembled calcium phosphate nanocomposites using block copolymer-peptide conjugates. *Journal of Materials Research* **2008**, *23*, 3196–3212.

(26) Rodríguez-Hernández, J.; Chécot, F.; Gnanou, Y.; Lecommandoux, S. Toward [`]smart' nano-objects by self-assembly of block copolymers in solution. *Progress in Polymer Science* **2005**, *30*, 691–724.

(27) Nakashima, K.; Bahadur, P. Aggregation of water-soluble block copolymers in aqueous solutions: Recent trends. *Advances in Colloid and Interface Science* **2006**, *123-126*, 75–96.

(28) Forster, S. Amphiphilic block copolymers for templating applications. *COLLOID CHEMISTRY 1* **2003**, *226*, 1–28.

(29) Förster, S.; Plantenberg, T. From Self-Organizing Polymers to Nanohybrid and Biomaterials. *Angew. Chem. Int. Ed.* **2002**, *41*, 688.

(30) Förster, S.; Antonietti, M. Amphiphilic Block Copolymers in Structure-Controlled Nanomaterial Hybrids. *Adv. Mater.* **1998**, *10*, 195–217.

(31) Husseini, G. A.; Pitt, W. G. Micelles and nanoparticles for ultrasonic drug and gene delivery. *Advanced Drug Delivery Reviews* **2008**, *60*, 1137–1152.

(32) Gil, E. S.; Hudson, S. M. Stimuli-reponsive polymers and their bioconjugates. *Progress in Polymer Science* **2004**, *29*, 1173–1222.

(33) Smart, T.; Lomas, H.; Massignani, M.; Flores-Merino, M. V.; Perez, L. R.; Battaglia, G. Block copolymer nanostructures. *Nano Today* **June**, *3*, 38–46.

(34) Alexandridis, P.; Alan Hatton, T. Poly(ethylene oxide)---poly(propylene oxide)---poly(ethylene oxide) block copolymer surfactants in aqueous solutions and at interfaces: thermodynamics, structure, dynamics, and modeling. *Colloids and Surfaces A: Physicochemical and Engineering Aspects* **1995**, *96*, 1–46.

(35) Determan, M. D.; Cox, J. P.; Seifert, S.; Thiyagarajan, P.; Mallapragada, S. K. Synthesis and characterization of temperature and pH-responsive pentablock copolymers. *Polymer* **2005**, *46*, 6933–6946.

(36) Iwahori, K.; Yamashita, I. Bio-template Synthesis of Nanoparticle by Cage-shaped Protein Supramolecule, Apoferritin. *J Clust Sci* **2007**, *18*, 358–370.

(37) Sun, Y.; Zhou, Y.; Wang, Z. Novel Hybrid Materials Obtained During the Crystalline Growth of Layered Double Hydroxides Using Grafted Chitosan as a Template. *J Inorg Organomet Polym* **2009**, *19*, 436–442.

(38) Zhou, X.; Xia, S.; Lu, Z.; Tian, Y.; Yan, Y.; Zhu, J. Biomineralization-Assisted Ultrasensitive Detection of DNA. *Journal of the American Chemical Society* **2010**, *132*, 6932–6934.

(39) Rey, C.; Combes, C.; Drouet, C.; Glimcher, M. J. Bone mineral: update on chemical composition and structure. *Osteoporos Int* **2009**, *20*, 1013–1021.

(40) Palmer, L. C.; Newcomb, C. J.; Kaltz, S. R.; Spoerke, E. D.; Stupp, S. I. Biomimetic Systems for Hydroxyapatite Mineralization Inspired By Bone and Enamel. *Chemical Reviews* **2008**, *108*, 4754–4783.

(41) Salgado, A. J.; Coutinho, O. P.; Reis, R. L. Bone Tissue Engineering: State of the Art and Future Trends. *Macromolecular Bioscience* **2004**, *4*, 743–765.

(42) Prozorov, T.; Palo, P.; Wang, L.; Nilsen-Hamilton, M.; Jones, D.; Orr, D.; Mallapragada, S. K.; Narasimhan, B.; Canfield, P. C.; Prozorov, R. Cobalt Ferrite Nanocrystals: Out-Performing Magnetotactic Bacteria. *ACS Nano* **2007**, *1*, 228–233.

(43) Bazylinski, D. A.; Frankel, R. B. Magnetosome formation in prokaryotes. *Nat Rev Micro* **2004**, *2*, 217–230.

(44) Arakaki, A.; Webb, J.; Matsunaga, T. A Novel Protein Tightly Bound to Bacterial Magnetic Particles in Magnetospirillum magneticum Strain AMB-1. *Journal of Biological Chemistry* **2003**, *278*, 8745 –8750.

(45) Deng, D.; Liao, X.; Liu, X.; Shi, B. Synthesis of hierarchical mesoporous zirconia fiber by using collagen fiber as a template. *Journal of Materials Research* **2008**, *23*, 3263–3268.

# Chapter 2 Bioinspired synthesis of organic/inorganic nanocomposite materials mediated by biomolecules

(Modified from a review paper published as a book chapter in "On Biomimetics", ISBN: 978-953-307-271-5, InTech, 2011)

Xunpei Liu and Surya K. Mallapragada

## Abstract

This review will discuss the use of biomolecules such as proteins/peptides as templates for bioinspired synthesis in different organic/inorganic hybrid material systems. Nature provides elegant examples of hierarchical structures that are hybrid materials formed by the mineralization of inorganic phases on organic templates, such as bones and shells, which are produced by natural organisms for support or protection purposes. In Nature, organic templates such as proteins, peptides, and polysaccharides, with ordered functional groups can facilitate and direct the structure and morphology of the inorganic phase. Bioinspired synthetic routes mimic the process of biomineralization, using biomolecules to develop novel advanced materials. This will offer an opportunity to create materials under mild conditions with controlled size, shape, crystal structure, and orientation in nanoscale. Proteins and peptides have attracted much attention for serving as the organic templates in bioinspired synthesis, because of their highly ordered molecular assemblies, various functions, and the rapid development of protein and peptide technologies. Mediated by spontaneously organized proteins or peptides, materials with hierarchical structure in nanoscale can be fabricated in vitro. For instance, collagen and other proteins have been used as templates in vitro to mimic the natural bone forming process, where calcium phosphate nanocrystals precipitate on collagen fibril templates. Magnetotactic bacteria can produce magnetite nanocrystals with uniform size and shape. Mms6 and other proteins cloned from

magnetotactic bacteria have been used for bioinspired synthesis of magnetite nanocrystals in vitro. These organic/inorganic hybrid materials can be used for biomedical, orthopedic, catalytic and magnetic applications.

## 2.1 Introduction

Many organisms are capable of synthesizing organic/inorganic composites for protective or support purposes, such as bones, shells, and teeth. They exert a remarkable level of molecular control on particle size, structure, morphology, aggregation, and crystallographic orientation of these organic/inorganic structured materials. These materials often hierarchically arrange from nanoscale to the macroscale [1–6]. For example, mollusks produce shells or nacres that contain a single distinct calcium carbonate crystalline phase, such as aragonite or calcite [7]. Magnetotactic bacteria produce $Fe_3O_4$ or $Fe_3S_4$ nanoparticles with well-defined sizes and shapes to recognize magnetic fields for alignment and migration [8,9]. Marine sponges produce silica spicules that have been demonstrated to possess light-guiding characteristics and may reach lengths of up to 3 m [10–12]. In each of the examples listed above, and in many more examples in nature (Figure 2.1), specialized biomolecules, such as proteins, peptides, deoxyribonucleic acid (DNA), ribonucleic acid (RNA), and polysaccharides, have been found or are thought to play a critical role in directing the formation of these hierarchically assembled inorganic structures [13,14]. The participation of biomolecules in the nucleation and growth of crystals has attracted much research attention. Most notably, the proteins involved in directing the shape of these biomaterials have often evolved to recognize and bind selectively to one or more faces of the growing crystal. For instance, important matrix proteins involved in bone growth contain different function domains that orient the protein on hydroxyapatite nanocrystals and interact with target cell receptors [15].

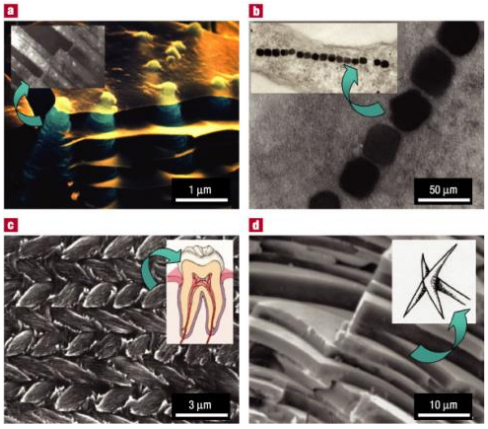


Figure 2.1 a, Scanning electron microscopy (SEM) image of a growth edge of abalone (*Haliotis rufescens*) displaying aragonite platelets (blue) separated by organic film (orange) that eventually becomes nacre. (inset: transmission electron microscope (TEM) image). b, Magnetite nanoparticles formed by magnetotactic bacterium (*Aquaspirillum magnetotacticum*, inset: TEM image). c, Mouse enamel (SEM image) is a hard, wear-resistant material with highly ordered micro/nano architecture consisting of hydroxyapatite crystallites that assemble into woven rod structure (inset: schematic cross-section of a human tooth). d, SEM image of sponge spicule (with a cross-shaped apex shown in inset) has layered silica with excellent optical and mechanical properties. (Reproduced from *Nature Materials*, 2003, volume 2, issue 9, 578. Copyright © 2003 Nature Publishing Group.)

Nature has always been a source of inspiration for technical developments. Materials scientists consider the hierarchical structure of natural materials as a model for the development of new types of high-performance engineered materials [16]. The biomimetic approach could lead to the development of the controlled synthesis of inorganic nanophases, the crystal engineering of bulk solids, and the assembly of organized composite and ceramic materials [3]. During the past decades, many inorganic crystals or hybrid inorganic/organic materials with special sizes, shapes, organization, complex forms, and hierarchies have been synthesized via bioinspired methods with the assistance of various templates, such as synthetic polymers, self-assembling peptides, proteins, and some low mass surfactant molecules [17,18]. Routine and reliable synthesis of self-assembled

hybrid materials with tunable functionalities are urgently required for real-life applications and economic commercialization [19,20].

There are mainly two mechanisms by which organisms control the self-assembled hierarchical organic/inorganic structures. First, the organic matrix serves as template on which to form a specific mineral. Second, inorganic materials usually appear in cells at the protoplasmic surface boundary layer. Therefore, the arrangement of the biominerals is controlled by the surface tension between the cells, the vesicles, and the growing mineral [5]. Recent work in the field of bioinspired synthesis has achieved varying degrees of success in both of these strategies, especially the first mechanism, in which the self-assembling organic structures are used to template the growth of inorganic materials. The structural information from the organic assembly is directly transcribed to the inorganic materials, or used to modify the morphology of the inorganic phases.

This review will focus on the recent successes in using self-assembling biomolecules as the organic matrix templates to direct and facilitate the formation of different kinds of structured organic/inorganic composite materials. The biomolecules are either natural or synthetic, including proteins, peptides, DNA, RNA and polysaccharides.

## 2.2 The advantage of using biomolecules for bioinspired synthesis, and their sources

The use of biomolecules to direct the *in vitro* syntheses of inorganic materials is promising due to a number of reasons. The first of these potential benefits is the production of materials under mild reaction conditions (neutral pH, room temperature, aqueous solution etc.), while traditional methods require severe reaction conditions. The reduction of energy input and avoidance of harmful solvents makes bioinspired syntheses inherently “green” processing. The second major advantage of using biomolecules for materials synthesis is the elegant control on

the size, shape, chemistry, and crystal structure of the inorganic product. These characteristics often impact or determine the properties of the synthesized material, making them have specific applications. Third, biomolecules offer the potential to produce materials with highly specific or multiple functions. Additionally, the large diversity of natural and synthetic biomolecules provides a high possibility of finding a biomolecule that can recognize, interact with, or direct the formation of an inorganic material [21].

The primary sources to obtain the biomolecules used for the bioinspired synthesis of materials include: biomolecules isolated or derived from biomineralizing organisms, biomineralizing biomolecule analogs, and peptides identified for biomineralization [21]. Biomolecules isolated or derived from biomineralizing organisms have been widely used for biomimetic synthesis of inorganic materials, however, the use of biomineral-isolated biomolecules has several drawbacks. For example, the biomolecules may be difficult to obtain or limited by the yield, may require specialized facilities to grow, and may provide few if any opportunities to modify or engineer protein sequences. Many of these difficulties may be overcome through the recombinant expression and subsequent purification of mineralizing proteins from bacterial cells [22]. Some of the sequence characteristics native to biomineralizing proteins may also be found in readily available and inexpensive proteins, such as hen egg white lysozyme (HEWL) or bovine serum albumin (BSA), making them popular candidates for biomimetic studies [23,24]. According to these recognized sequences, biomineralizing biomolecule analogs can be developed. The analogs are not restricted to biomolecules, for instance, synthetic polymers are also developed as templates for bioinspired inorganic synthesis [25,26]. The development of peptide, DNA, and RNA identification, separation, and synthesis techniques provides more opportunity to design templates for the bioinspired inorganic material synthesis,

for example, phage display is used for identifying peptides and systematic enrichment of ligands by exponential enrichment (SELEX) is used for recognize RNA [1].

Different types of biomolecules used in bioinspired synthesis can be broadly categorized into four categories: proteins, peptides, nucleic acids, and polysaccharides. The role of these different types of biomolecules in the bioinspired synthesis and fabrication process is discussed in greater detail using specific cases as examples in the following sections.

## 2.3 Protein-mediated bioinspired synthesis

Proteins provide functional building blocks for the development of multi-functional materials[27]. The self-assembly property of proteins would allow controlled organization of the organic/inorganic interface based on molecular recognition, resulting in hierarchical organization with desirable properties at multiple length scales. Proteins have superior specificity for target binding with complex molecular recognition mechanism [28]. Through their unique and specific interactions with other macromolecules and inorganics, they process the ability to control structures and functions of biological hard and soft tissues in organisms [29]. In the following sections, several examples of protein-mediated bioinspired synthesis of structured organic/inorganic materials *in vitro* are highlighted.

### 2.3.1 Protein mediated hydroxyapatite (HAp) formation

Bone is a highly ordered, dynamic, and highly vascularized tissue that exhibits excellent strength, hardness and fracture toughness. It is a biocomposite of 70% mineral (mostly nanoscale calcium phosphate crystals) and 30% organics (including collagen, glycoproteins, proteoglycans, and sialoproteins) by dry weight [4,30,31]. Calcium phosphates, notably HAp [$Ca_{10}(PO_4)_6(OH)_2$], exhibit many levels of hierarchical structures in bone from nano to macro scales [32]. Mineralized collagen fibrils are the basic building block for bone formation. More than 20 human collagens

have been reported. In collagens, the amino acids glycine, proline, and hydroxyproline account for more than 50% of the amino acid composition, often presented as the Gly-X-Y repeat unit (where X and Y are either proline or hydroxyproline) [33]. Most collagens display a 67 nm periodicity due to the axial packing of the individual collagen molecules [34]. Collagens also serve as extracellular matrix molecules for many other soft and hard tissues, such as cartilage tendons, and ligaments.

We highlight some recent studies focused on the collagen-HAp interactions in the bioinspired synthesis of HAp composite materials. A nanocomposite of collagen and HAp was prepared in a continuous flow system, mimicking the situation *in vivo*, and resulted in a direct nucleation of HAp on the self-assembled collagen matrix. The biomineralization process of collagen and the self-organization mechanism were also analyzed. The inorganic crystals formed along the collagen fiber have similar a Ca-P ratio, crystalline degree, and carbonation extent to that observed in bone [35]. Another study investigated the function of osteonectin in the formation of HAp. Osteonectin was added into the collagen solution, and results indicated that spindle-like nano-HAp could be deposited on collagen I/osteonectin and pure osteonectin (control) groups, but not on collagen II/osteonectin [36]. This may help in understanding the biomineralization process in nature.

Another collagen templated HAp nanocomposite showed equal or better biocompatibility than HAp ceramics, which was known to have excellent biocompatibility. The c-axes of HAp nanocrystals were regularly aligned along collagen fibrils, which was similar to natural bone orientation. The composite promoted the osteoclastic resorption of the composite, followed by new bone formation by osteoblasts, which was very similar to the reaction of a transplanted autogenous-bone. Therefore, the HAp/collagen composite can be potentially used as an artificial bone material in medical and dental fields [37].

In another study, two different bioinspired methods were used to fabricate HAp on collagen templates: dispersion of synthetic HAp in a solution of telopeptide-free collagen molecules and direct nucleation of HAp into reconstituted collagen fibers during their assembly. Composite materials obtained by direct nucleation showed similar composition, morphology, and structure to natural bone, and also indicated an intimated interaction between the inorganic phase and protein components [38]. This proved the template function of the collagen during the bone formation.

Proteins other than collagen are also used in bioinspired HAp synthesis. A novel human hair proteins and HAp composite was synthesized for using as a biomineral-scaffolding material. The human hair protein was soaked to a $CaCl_2$ solution for fabrication into flat films. The flat films mainly consisted of α-keratin, which could bind 3 $Ca^{2+}$ ions per 1 keratin molecule. The composite of the human hair protein and calcium phosphate was prepared via alternate soaking processes using $CaCl_2$ and $Na_2HPO_4$ solutions. The diameters of deposited calcium phosphate particles were about 2–4 μm. The human hair proteins were not soluble and degraded during the soaking processes.[39] Synthetic proteins have also been developed as templates for bioinspired synthesis. Self-assembled chimeric protein hydrogels comprising leucine zipper motifs flanking a dentin matrix protein 1 domain were developed to act as a HAp nucleator for the formation of highly oriented apatite similar to bone mineral [27].

### 2.3.2 Protein mediated magnetic materials formation

Magnetotactic bacteria form magnetite nanoparticles *in vivo* with various morphologies [8]. The magnetospirillum magneticum strain AMB-1 produces a chain of cuboctahedral magnetite nanocrystals, each surrounded by a lipid bilayer membrane (Figure 2.1 b). Several proteins isolated from the magnetosome membranes showed common features in their amino acid sequences, which contain hydrophobic N-terminal and hydrophilic C-terminal regions. The C-terminal regions in Mms5, Mms6, Mms7, and Mms13 contain dense carboxyl and hydroxyl

groups that bind iron ions. Nano sized magnetic particles similar to those in magnetotactic bacteria were prepared *in vitro* by chemical synthesis of magnetite in the presence of the protein Mms6. These proteins may be directly involved in biological magnetite crystal formation in magnetic bacteria [40].

Similar *in vitro* synthesis of magnetite mediated by Mms6 was also achieved by other research groups. Recombinant Mms6 facilitated the formation of magnetite nanocrystals with uniform size (about 30 nm) in aqueous solution, which was verified by using TEM analysis and magnetization measurements. A polymeric gel was used to mimic the conditions at which magnetite nanocrystals were formed in magnetotactic bacteria and slow down the diffusion rates of the reagents. The nanocrystals formed in the presence of other proteins, as shown in Figure 2.2, did not exhibit the uniform sizes and shapes. Mms6-mediated magnetite nanoparticles demonstrated the largest magnetization values above the blocking temperature, and the largest magnetic susceptibility compared to those of the nanomaterials synthesized with other proteins. This study confirmed the hypothesis that Mms6 promotes the shape-selective formation of uniform superparamagnetic nanocrystals [41].

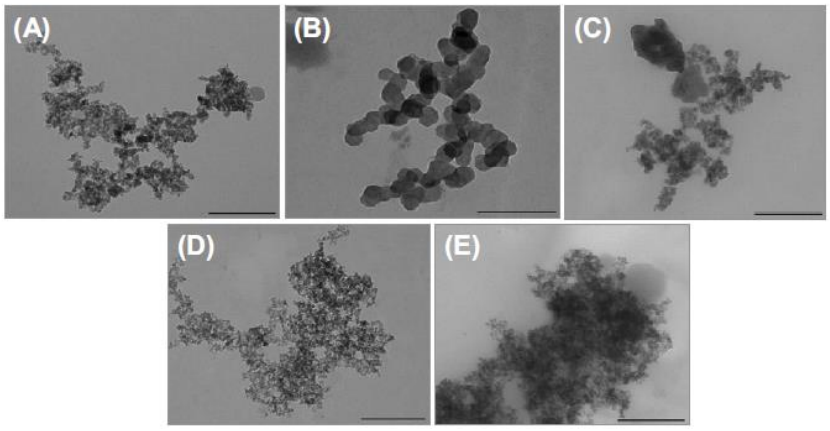


Figure 2.2 TEM images of magnetite nanoparticles obtained by co-precipitation of $FeCl_2$ and $FeCl_3$: A) without protein, B) with Mms6, C) with ferritin, D) with Lnc2, and E) with BSA.

(Adapted from *Advanced Functional Materials*, volume 17, issue 6, 952. Copyright © 2007 WILEY-VCH Verlag GmbH & Co. KGaA, Weinheim.)

Some inorganic magnetic materials which do not appear in living organisms, for example, cobalt ferrite ($CoFe_2O_4$) nanoparticles, were also synthesized *in vitro* by using Mms6 protein as a template. The recombinant full-length Mms6 protein or a synthetic C-terminal domain of Mms6 protein was covalently attached to self-assembling polymers (Pluronic F127) in order to template hierarchical growth of $CoFe_2O_4$ nanostructures, as shown in Figure 2.3. This new synthesis route enabled facile room-temperature shape-specific synthesis of complex magnetic crystalline nanomaterials with particle sizes of 40–100 nm, which were difficult to produce using conventional techniques [42].

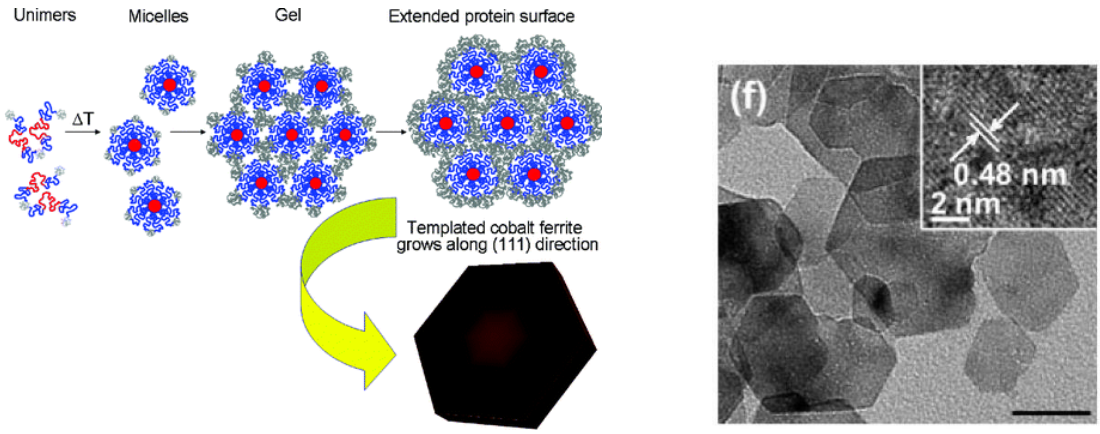


Figure 2.3 Left, scheme for the protein-templated synthesis of $CoFe_2O_4$ nanocrystals in the presence of the Pluronic-conjugated recombinant Mms6 (red and blue colors stand for the Pluronic, and grey color stands for the protein); right, TEM of $CoFe_2O_4$ nanocrystals obtainedin the presence of Pluronic-conjugated c25-mms6. (Inset) High-resolution TEM image of a fragment of the central particle. The scale bar in all images is 50 nm. (Reproduced from *ACS Nano*, volume 1, issue 3, 231. Copy right © 2007, American Chemistry Society.)

### 2.3.3 Protein mediated silica formation

Aizenberg et al. reported the structural hierarchy of biosilica observed in the hexactinellid sponge *Euplectella sp*. (see Figure 2.4). The ensuing design overcomes the brittleness of its constituent material, glass, and shows outstanding mechanical rigidity and stability [6].

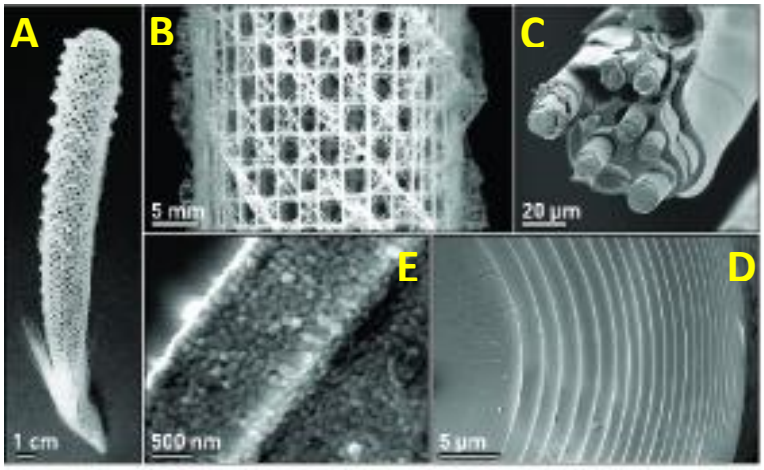


Figure 2.4 Structural analysis of the mineralized skeletal system of *Euplectella sp*. (A) Photograph of the entire skeleton, showing cylindrical glass cage. (B) Fragment of the cage structure showing the square-grid lattice of vertical and horizontal struts with diagonal elements arranged in a chessboard manner. (C) SEM of a fractured and partially HF-etched single beam revealing its ceramic fiber-composite structure. (D) SEM of a cross section through a typical spicule in a strut, showing its characteristic laminated architecture. (E) Bleaching of biosilica surface revealing its consolidated nanoparticulate nature. (Adapted from *Science*, volume 309, issue 5732, 276. Copyright © 2005, American Association for the Advancement of Science.)

Silicateins, or silica proteins, were found to be enzymes (structural and catalytic proteins) that promote biosilica formation in nature [43]. The silicateins exhibit catalytic activity at neutral pH and low temperature. They have also been used as templates to direct the growth of silica particles along the axial protein filament. It has been used to simultaneously catalyze and structurally direct the hydrolysis and condensation of tetraethyl orthosilicate *in vitro* to form silica [44]. Silicatein filaments also demonstrated the ability to form titanium dioxide, gallium oxohydroxide

(GaOOH) and gamma-gallium oxide (gamma-$Ga_2O_3$) *in vitro*, which are three inorganic semiconductors that biological species have never naturally produced[45–48]. An enzymatic biocatalyst from the marine sponge *Tethya aurantia*, was used to catalyze and template the hydrolysis and condensation of the molecular precursor $BaTiF_6$ at low temperature to form nanocrystalline $BaTiOF_4$ [49].

Amorphous silica (or silica glass) is widely used in different applications, such as membranes, columns, heat-proof materials, optical communication fibers, and catalysts in organic synthesis [50]. The catalyzing effect of the silicatein from the freshwater sponge *Cauxi* promoted the polymerization of this type of silica *in vitro*. Briefly, the sponge shot the axial protein filament in the desired growth direction, and then silicatein polymerized a thin silica layer around the filament. However, this silica deposition inhibited the transport of the siliceous acid to the axial filament, and a new set of silicatein were shot onto the newly synthesized silica deposition. This shooting process continued until the final diameter of spicules was reached. The process is shown by Figure 2.5. This study offered a new route for the development of mesoporous, amorphous silica with high purity under ambient condition [50].

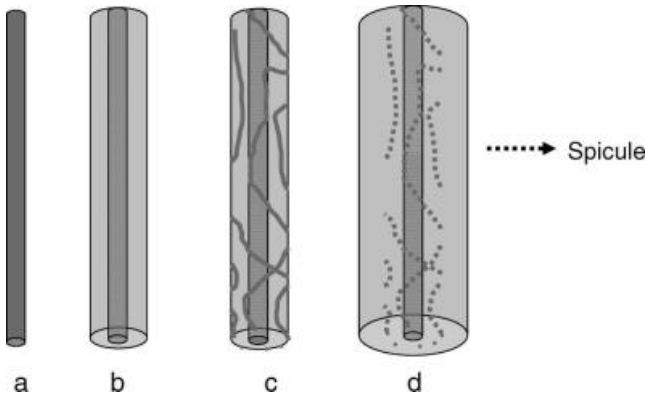


Figure 2.5 Schematic illustration of the growth mechanism of amorphous silica. (Reproduced from *Journal of the American Chemical Society*, volume 131, issue 7, 2720. Copy right © 2009, American Chemistry Society.)

Silicateins could be immobilized onto a template surface, while still preserving their catalytic activity. In a bioinspired approach, biosilica was synthesized on "inert" surfaces (matrices) from monomeric precursors [51]. The matrices were first functionalized with a reactive polymer that was subsequently able to chemisorb nitrilotriacetic acid (NTA), a required binder for His-tagged recombinant silicatein. Silicatein that had been immobilized onto this matrix using NTA-His tag linkage had the capability to synthesize nanoparticulate biosilica, biotitania, and biozirconia from monomeric precursors. The process is shown by Figure 2.6.

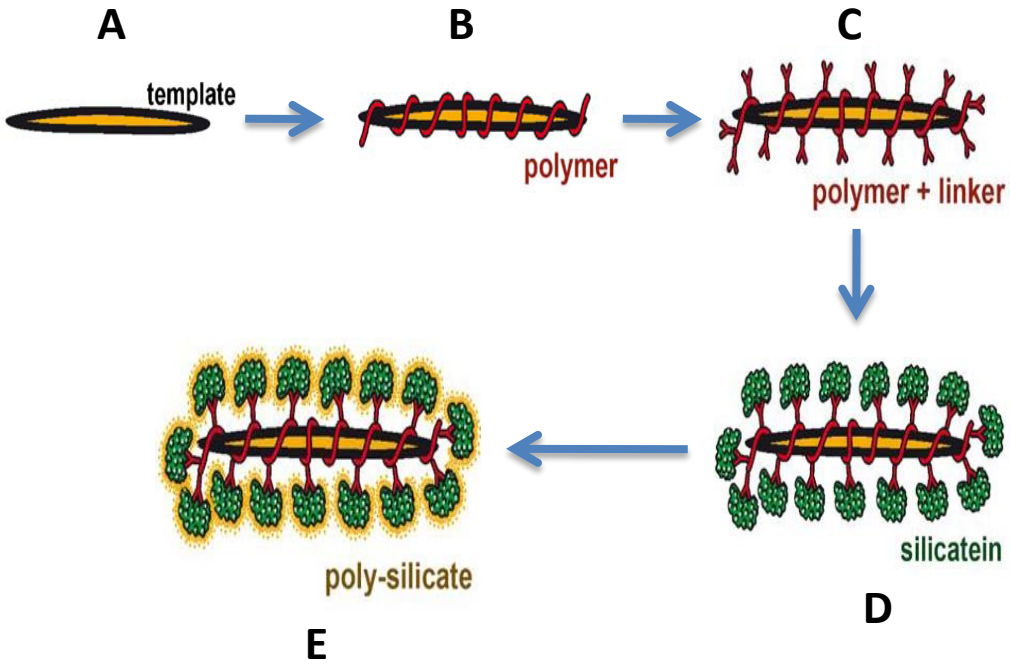


Figure 2.6 The biomimetic approach: The template (A) is successively functionalized with a reactive ester polymer (B) and the NTA linker (C). (D) Recombinant silicatein is bound via His-tag and $Ni^{2}+$ to the NTA-polymer and subsequently mediates formation and assembly of polysilica formation (E). (Adapted from *Applied Microbiology and Biotechnology*, volume 83, number 3, 408. Copyright © 2009, Springer-Verlag.)

Fungi have been used in bioinspired synthesis of inorganic materials. Silica, zirconia, and titania nanoparticles were produced by mixing the fungus *Fusarium oxysporum* with aqueous anionic complexes $SiF_6^{2-}$, $ZrF_6^{2-}$, and $TiF_6^{2-}$, respectively. It has been shown that the extra-cellular protein of the *Fusarium oxysporum* mediated hydrolysis of the anionic complexes. These studies introduced a facile room temperature synthesis of crystalline titania and zirconia particles, whereas calcination at 300 ℃ is required for crystallization of silica [52,53].

## 2.3 Peptide-mediated bioinspired synthesis

Peptides consist of short amino acid sequences that have less intricate functionality than proteins. Although peptides may not perform highly specialized functions compared to proteins, they can be synthesized more easily with desired amino acid sequences by well-established chemical and genetic engineering techniques. Therefore, they are widely used in the applications ranging from controlled gene and drug release, nanofabrication, biomineralization, and membrane protein stabilization to three-dimensional (3D) cell culture and tissue engineering. Peptides are designed to be folded in desired conformations, such as α-helix, β-sheet, etc. These 3D building blocks may yield supramolecular structures through self-assembly process. Moreover, the supramolecular structures can be controlled by changing the physicochemical properties of the environment such as pH, temperature, and salt content, which makes peptides versatile smart materials for the design of structured materials [28,54].

There are several possible ways of obtaining polypeptide sequences with specific affinity to inorganics. For example, well-established *in vivo* combinatorial biology protocols, phage display, and cell-surface display have been used to identify biological ligands and to map the molecular recognition site of antibodies. Table 1 shows the specific binding affinity of peptides for various inorganic materials.

Table 2.1 Examples of polypeptide sequences exhibiting affinity for various inorganics. (Reproduced from *Nature Materials*, 2003, volume 2, issue 9, 581. Copyright © 2003 Nature Publishing Group.)

| Materials | Sequences | Size | pI | MW | Charge |
|---|---|---|---|---|---|
| Au | MHGKTQATSGTIQS | 14 | 8.52 | 1446.60 | +1 |
| | SKTSLGQSGASLQGSEKLTNG | 21 | 8.31 | 2050.12 | +1 |
| | QATSEKLVRGMEGASLHPAKT | 21 | 8.60 | 2211.52 | +1 |
| Pt | DRTSTWR | 7 | 9.60 | 920.98 | +1 |
| | QSVTSTK | 7 | 8.75 | 749.82 | +1 |
| | SSSHLNK | 7 | 8.49 | 771.83 | +1 |
| Pd | SVTQNKY | 7 | 8.31 | 838.92 | +1 |
| | SPHPGPY | 7 | 6.46 | 753.81 | 0 |
| | HAPTPML | 7 | 6.74 | 765.93 | 0 |
| Ag | AYSSGAPPMPPF | 12 | 5.57 | 1221.39 | 0 |
| | NPSSLFRYLPSD | 12 | 6.09 | 1395.53 | 0 |
| | SLATQPPRTPPV | 12 | 9.47 | 1263.46 | +1 |
| SiO2 | MSPHPHPRHHHT | 12 | 9.59 | 1470.63 | +1 |
| | RGRRRRLSCRLL | 12 | 12.30 | 1541.89 | +6 |
| | KPSHHHHHTGAN | 12 | 8.87 | 1359.43 | +1 |

Table 2.1 Continued

| | | | | | |
|---|---|---|---|---|---|
| | VKTQATSREEPPRLPSKHRPG | 21 | 10.93 | 2371.68 | +3 |
| Zeolites | MDHGKYRQKQATPG | 14 | 9.70 | 1616.82 | +2 |
| | NTRMTARQHRSANHKSTQRA | 20 | 12.49 | 2351.59 | +4 |
| ZnO | YDSRSMRPH | 9 | 8.75 | 1148.26 | +1 |
| | HTQNMRMYEPWF | 12 | 6.75 | 1639.87 | 0 |
| CaCO3 | DVFSSFNLKHMR | 12 | 8.75 | 1480.90 | +1 |
| | VVRPKAATN | 9 | 11.00 | 955.13 | +2 |
| Cr2O3 | RIRHRLVGQ | 9 | 12.30 | 1134.35 | +3 |
| Fe2O3 | RRTVKHHVN | 9 | 12.01 | 1146.32 | +3 |
| | AQNPSDNNTHTH | 12 | 5.97 | 1335.31 | 0 |
| GaAs | RLELAIPLQGSG | 12 | 6.00 | 1253.46 | 0 |
| | TPPRPIQYNHTS | 12 | 8.44 | 1410.55 | +1 |
| ZnS | NNPMHQN | 7 | 6.74 | 853.91 | 0 |

A 12-residue peptide (NPYHPTIPQSVH-GGGK-biotin: CLP12 peptide) has been identified for HAp biomineralization using phage display. The sequence responsible for the mineralizing

activity resembled the tripeptide repeat (Gly-Pro-Hyp) of type I collagen. This peptide was capable of binding to single crystal HAp and templating the nucleation and growth of crystalline HAp mineral in a sequence- and composition-dependent manner[55]. In another study, polylysine and polyleucine based block copolypeptides ($K_{170}L_{30}$) were found to form gels at very low concentrations in aqueous media. The block copolypeptides have been used as templates for forming self-assembled calcium phosphate nanocomposites. The synthesis method allowed for simultaneous formation of the self-assembled block copolypeptide gel and of the inorganic phase. The inorganic contents accounted for over 50 wt% in the nanocomposite, approaching the inorganic content in bone[56]. Thermoreversibly gelling block copolymers (Pluronic F127) conjugated to hydroxyapatite-nucleating peptides (DSKSDSSKSESDSS) were used to template the growth of inorganic calcium phosphate in aqueous solutions. The inorganic phase in the organic/inorganic nanocomposite was confirmed to be HAp. This work offered a route for the development of novel, self-assembling, injectable nanocomposite biomaterials for potential orthopedic applications [57].

Self-assembling peptide amphiphiles have great potential as templates for nanofabrication. In 2001, a lipopeptide was designed and synthesized for biomineralization by the Stupp group [58]. In Figure 2.7 a and b, the $C_{16}$ tail was connected to the N terminal of a peptide sequence which contained four cysteines, three glycines, a single phosphorylated serine and a cell adhesion ligand RGD ($C_{16}$–$C_4G_3$S(p)RGD–OH). The $C_{16}$ tail was hydrophobic and the peptide sequences were hydrophilic. These peptide amphiphlies self-assembled into cylindrical micellar structures in aqueous phase. $C_{16}$ acyl tails packed themselves in the center of the micelle, while the peptide sequences formed β-sheets at the outside. There were disulfide bonds that formed by cross-linking of the four cysteine residues in the middle of the molecules, making the self-assembled nanofibers robust and impervious to pH variation (Figure 2.7 c). The nanofibers were then used to

direct the mineralization of HAp. The HAp nucleated on the surfaces of the lipopeptide nanofibers and its crystals grew with their c-axes oriented along the long axes of the nanofibers. This alignment was the same as that observed between collagen fibers and HAp crystals in bone[54,58].

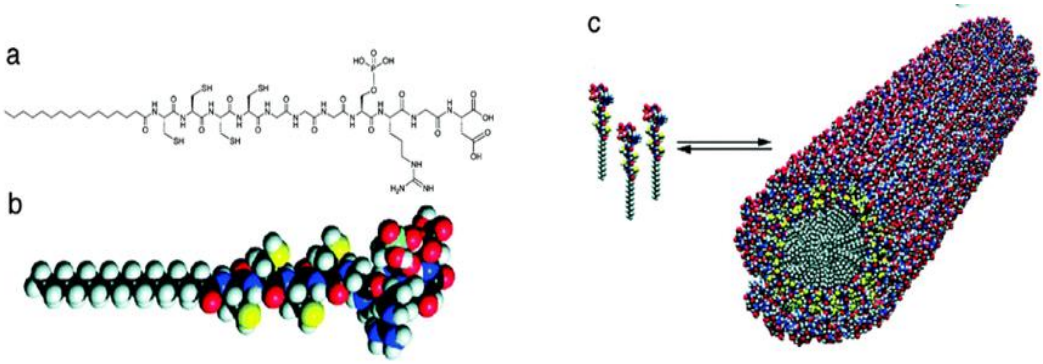


Figure 2.7 (a) Chemical structure of the peptide amphiphiles. (b) Molecular model of the peptide amphiphiles. (c) Schematic model of the self-assembly of peptide amphiphiles into a cylindrical micelle. (Reproduced from *Chemical Reviews*, volume 108, issue 11, 4776. Copyright © 2008, American Chemical Society.)

Shorter peptide $I_3K$ may form nanotubes with diameters about 10 nm and lengths over 5 mm. The nanostructure from this ultra-short peptide indicated that the amphiphilicity of a peptide amphiphile can be balanced between the length of a peptide sequence and the size of hydrophobic amino acids. $I_3K$ molecules were thought to initially interdigitate with each other through the hydrophobic interaction among the $I_3$ tails, forming bilayer fragments. The self-assembly was driven by the hydrophobic affinity between isoleucine residues with the $I_3$ tails packed in the middle and the K residues projected at the outside, facing the water. The peptide bilayer fragments then further assembled into twisted ribbons. The fusion of the helical ribbons resulted in the formation of stable nanotubes, indicating the strong driving force along the main axial direction of the nanotubular structure. Figure 2.8 shows the self-assembling process. Because of

their extreme stability against heating or exposure to organic solvents, $I_3K$ nanotubes were used as templates for silicification from the hydrolysis of TEOS (tetraethoxysilane) precusor. The lysine groups on the inner and outer nanotube surfaces catalyzed the silicification, leading to the formation of silica nanotubes [59].

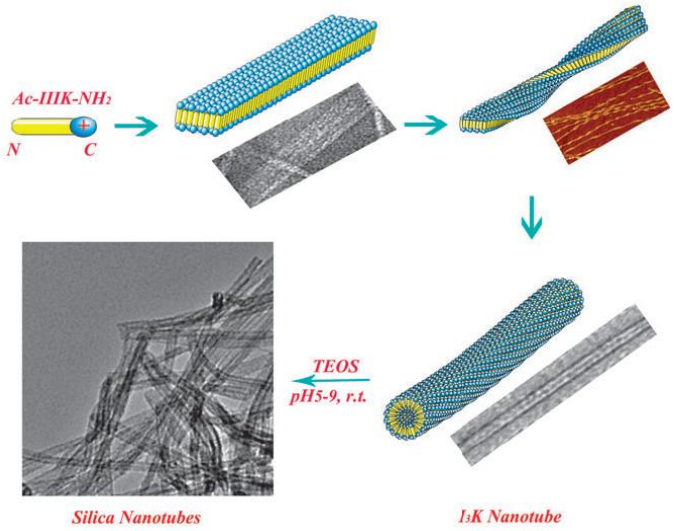


Figure 2.8 A schematic representation of $I_3K$ self-assembly process leading to the formation of peptide nanotubes which can then serve as templates for silicification. (Reproduced from *Chemical Society Reviews*, volume 39, issue 9, 3484. Copyright © Royal Society of Chemistry 2010.)

## 2.5 DNA and RNA-mediated bioinspired synthesis

DNA and RNA can self-assemble into well-defined secondary and tertiary structures at the nanoscale, which provide an ideal template for the formation of nanocrystals [60]. DNA templated gold nanoparticles have attracted much attention, as the self-assembled DNA nanostructures offer programmable scaffolds to organize the gold nanoparticles [60–63]. A self-assembled two-dimensional (2D) DNA nanogrid was used as a template to grow 5-nm gold nanoparticles (Au NPs) into periodic square lattices, as shown by Figure 2.9. The center-to-center distance between

neighboring particles was about 38 nm. These accurate controlled Au NPs distribution may find applications in nanoelectronic and nanophotonic devices [62].

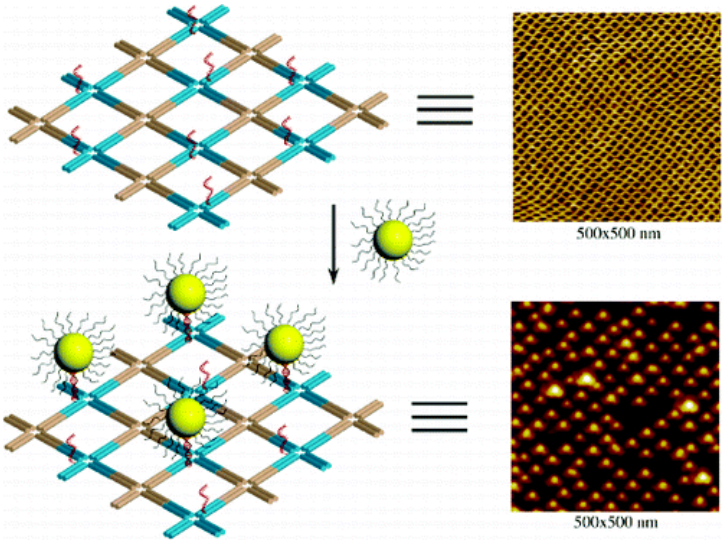


Figure 2.9 Top left: the 2D DNA nanogrids with the single strand $A_{15}$ out of the plane; Bottom left: assembly of 5-nm Au NPs on the DNA grids. The zigzag black lines surrounding the Au NPs represent the $T_{15}$ strands covalently linked to the surface of the particle through Au−S bonds. The right images are the AFM height data corresponding to each of their left. (Reproduced from *Nano Letters*, volume 6, issue 2, 248. Copyright © 2006, American Chemical Society.)

A chemically well-defined bio-core in an inorganic shell nanohybrid material was recently reported. It consisted of a DNA molecule as the bio-core with a size of 100 nm and a spherical inorganic nanoshell reassembled with exfoliated layered metal hydroxide (MH) with an overall thickness of 10 nm. The negatively charged DNA molecules can be encapsulated into a positively charged inorganic nanocavity of self-assembled MH nanosheets, as illustrated in Figure 2.10. Due to the pH-dependent solubility of the MH nanoshell, the DNA can be encapsulated and released, which play a crucial role in maximizing the stability of base sequence-manipulated and probe-functionalized DNA molecules with designed information. Therefore, these hybrid materials

could be used as advanced gene delivery systems and a biomedical diagnostics system for DNA-based information [64].

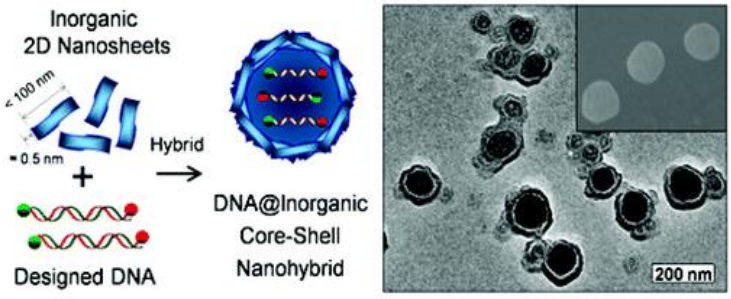


Figure 2.10 Scheme, TEM and SEM image for the designed DNA@Inorganic Core−Shell nanohybrid. (Reproduced from *Journal of the American Chemical Socciety*, volume 132, issue 47, 16735. Copyright © 2010, American Chemical Society.)

A multi-lamellar structure was formed by complexes of anionic DNA and cationic liposomes self-assembly. The two-dimensional lipid sheets confined a periodic one-dimensional lattice of parallel DNA chains, as shown by Figure 2.11. These simple DNA-membrane templates could be used for controlled CdS crystalline synthesis. $Cd^{2+}$ ions condensed on the DNA chains, and subsequently reacted with $H_2S$ to form CdS nanorods. Depending on the charge of the membrane, different concentrations of $Cd^{2+}$ ions condense onto the template, and different morphologies of CdS were formed. The degree of template overcharging was determined by the relative stoichiometry of DNA and cationic membrane lipids [65].

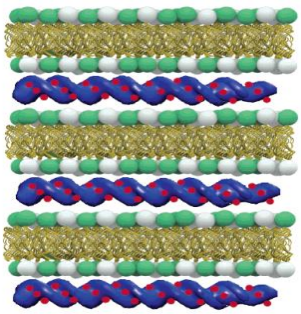

Figure 2.11 Schematic representation of CdS growth within DNA-membrane complexes: the $Cd^{2+}$ ions (red balls) are organized by DNA strands (blue) in the lamellar DNA−membrane complexes (side-view). (Reproduced from *Journal of the American Chemical Society*, volume 126, issue 43, 14158. Copyright © 2004, American Chemical Society.)

One kind of DNA molecules were reported to mediate the nucleation and growth of the calcium carbonate particles. $CaCO_3$ microspheres with different surface morphologies were prepared in the presence of the DNA, indicating that DNA could induce biomineralization in the biological system. It was found that the DNA concentration influenced on the surface structures of $CaCO_3$ particles significantly. This research provided new insight into the morphological control of $CaCO_3$ and other inorganic materials (Cheng et al. 2010).

The Kelley group investigated the role of RNA secondary structure on the growth of CdS nanocrystals. They showed that a folded wild-type tRNA (wtRNA) and an unfolded mutant tRNA (mtRNA) of identical length were both able to mediate the formation of CdS during its spontaneous precipitation from solution, but they saw differences in the average nanocrystal sizes and size distributions. A narrow distribution around 6 nm diameter particles was found for particles grown with wtRNA, while mtRNA generated a bimodal distribution of 7 and 11.5 nm diameter particles. This is a good illustration that a biomolecule can affect the nanocrystal size [66].

## 2.6 Polysaccharide-mediated bioinspired synthesis

A slow but increasing interest has been developing to explore the role of polysaccharides in biomineralization, despite the fact that they have been prevalent since the early stages of evolution. Single types of polysaccharides are typically not associated with biominerals. Only hydroxylated, carboxylated, or sulfated polysaccharides, or those containing a mixture of these functional moieties, are found in biominerals [67]. Chitin is the second most abundant natural polymer after cellulose on earth. It is a linear polysaccharide of β-(1-4)-2-acetamido-2-deoxy-d-

glucose. The chemical structure of chitin is very similar to that of cellulose, with a hydroxyl group replaced by an acetamido group. Pure chitin with 100% acetylation does not exist in nature. Chitin tends to form a co-polymer with its N-deacetylated derivative, chitosan. Chitosan is a polymer of β-(1-4)-2-amino-2-deoxy-d-glucose. The chemical structures of cellulose, chitin, and chitosan are shown in Figure 2.12 [68].

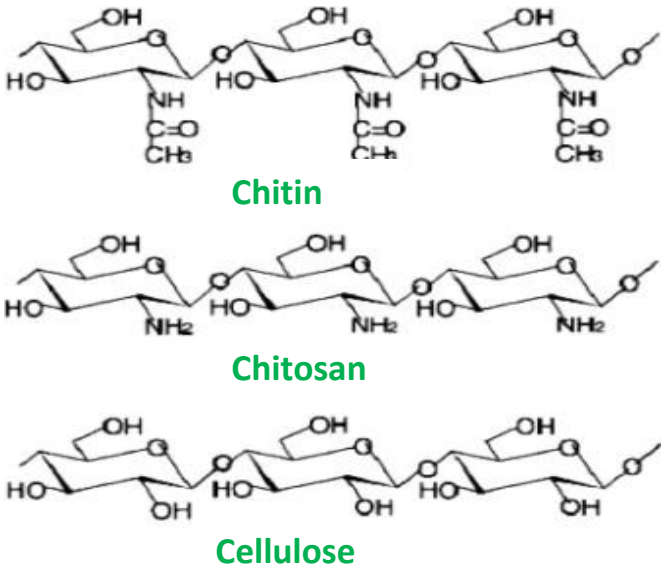


Figure 2.12 Chemical structures of chitin, chitosan, and cellulose.

Chitosan composite materials have attracted much research interest in bone tissue engineering due to their minimal foreign body reactions, intrinsic antibacterial nature, biocompatibility, biodegradability, and ability to be molded into various geometries and forms. Recently, grafted chitosan natural polymer with carbon nanotubes has been incorporated to increase the mechanical strength of artificial bone [69]. Laminated HAp/chitosan nanocomposites and nano-HAp/chitosan-pectin composites were prepared and showed improved strength, especially in moist environments. This combination can be expanded to other HAp-biopolymer systems, thus offer a new insight for fabricating biomimetic nanocomposites [70,71].

Chitosan was also used as organic template to form HAp nanocrystals. Spindle shaped HAp with 30- 40 nm length and 7- 8 nm width was synthesized through the biomimetic method with chitosan as template. The spindle shaped nano HAp grew in a 0.5wt% chitosan solution for 7 days. The crystallinity of samples increased with the aging time. The HAp powders synthesized with chitosan as templates had good thermal stability up to 800 ℃ [72].

Design and synthesis of bacterial cellulose/HAp nanocomposites was reported for bone healing applications using a bioinspired approach. Bacterial cellulose with various surface morphologies (pellicles and tubes) was negatively charged by the adsorption of carboxymethyl cellulose to initiate nucleation of calcium-deficient hydroxyapatite (cdHAp). The cdHAp was grown *in vitro* via dynamic simulated body fluid treatments for 7 days [73]. Cellulose also used to template the growth of silica. Through *in-situ* growth of silica nanoparticles on cotton fabrics, a dual-scaled surface with nanoscaled roughness of silica and microscaled roughness of cellulose fiber was generated [74].

## 2.7 Conclusions and outlook

In summary, in the recent past, there has been remarkable progress in the development of bioinspired procedures for controlling inorganic crystal nucleation and growth, especially at the nanoscale. Biomolecules have been successfully utilized to produce a variety of self-assembled structured inorganic materials under relatively mild conditions. Biomolecules have been found to be able to direct or modify the shapes, sizes, crystal structures, and other properties of the synthesized inorganic materials. Examples of such bioinspired inorganic nanostructures include HAp, $SiO_2$, $Fe_3O_4$, CdS, $TiO_2$, $ZrO_2$, gold and silver *etc.*, which have applications in biomedical, biosensor, bioceramic, and other fields. Modern biotechnology has also enabled the construction

of chimeric biomolecules with desired properties, which may be utilized to create hierarchical assembled and reinforced composite materials.

In the recent past, many biomolecules promoting materials synthesis have been identified. The number of inorganic materials that could be used for bioinspired synthesis has also been expanded. However, our fundamental understanding of these existing topics must be furthered in order to more fully harness the potential of biomolecules for material syntheses. There are also a number of interesting and powerful new concepts that have received only passing attention or remain unexplored. Design of more hierarchically self-assembled biomolecules that could template and direct the inorganic formation is also required. With the continued attention and ingenuity of researchers from diverse disciplines, the future of biomimetic materials syntheses promises to be exciting, dynamic, and rich in applications.

## Acknowledgements

This work was supported by the U.S. Department of Energy, Office of Basic Energy Science, Division of Materials Sciences and Engineering. The research was performed at the Ames Laboratory. Ames Laboratory is operated for the U.S. Department of Energy by Iowa State University under Contract No. DE-AC02-07CH11358.

## References

(1) Feldheim, D. L.; Eaton, B. E. Selection of Biomolecules Capable of Mediating the Formation of Nanocrystals. *ACS Nano* **2007**, *1*, 154–159.

(2) Dujardin, E.; Mann, S. Bio-inspired Materials Chemistry. *Adv. Mater.* **2002**, *14*, 775.

(3) Mann, S.; Archibald, D. D.; Didymus, J. M.; Douglas, T.; Heywood, B. R.; Meldrum, F. C.; Reeves, N. J. Crystallization at Inorganic-organic Interfaces: Biominerals and Biomimetic Synthesis. *Science* **1993**, *261*, 1286 –1292.

(4) Palmer, L. C.; Newcomb, C. J.; Kaltz, S. R.; Spoerke, E. D.; Stupp, S. I. Biomimetic Systems for Hydroxyapatite Mineralization Inspired By Bone and Enamel. *Chemical Reviews* **2008**, *108*, 4754–4783.

(5) Estroff, L. A.; Hamilton, A. D. At the Interface of Organic and Inorganic Chemistry: Bioinspired Synthesis of Composite Materials. *Chemistry of Materials* **2001**, *13*, 3227–3235.

(6) Aizenberg, J.; Weaver, J. C.; Thanawala, M. S.; Sundar, V. C.; Morse, D. E.; Fratzl, P. Skeleton of Euplectella sp.: Structural Hierarchy from the Nanoscale to the Macroscale. *Science* **2005**, *309*, 275 –278.

(7) Addadi, L.; Joester, D.; Nudelman, F.; Weiner, S. Mollusk Shell Formation: A Source of New Concepts for Understanding Biomineralization Processes. *Chem. Eur. J.* **2006**, *12*, 980–987.

(8) Bazylinski, D. A.; Frankel, R. B. Magnetosome formation in prokaryotes. *Nat Rev Micro* **2004**, *2*, 217–230.

(9) Komeili, A. Molecular Mechanisms of Magnetosome Formation. *Annu. Rev. Biochem.* **2007**, *76*, 351–366.

(10) Aizenberg, J.; Sundar, V. C.; Yablon, A. D.; Weaver, J. C.; Chen, G. Biological glass fibers: Correlation between optical and structural properties. *Proceedings of the National Academy of Sciences of the United States of America* **2004**, *101*, 3358 –3363.

(11) Sundar, V. C.; Yablon, A. D.; Grazul, J. L.; Ilan, M.; Aizenberg, J. Fibre-optical features of a glass sponge. *Nature* **2003**, *424*, 899–900.

(12) Cattaneo-Vietti, R.; Bavestrello, G.; Cerrano, C.; Sara, M.; Benatti, U.; Giovine, M.; Gaino, E. Optical fibres in an Antarctic sponge. *Nature* **1996**, *383*, 397–398.

(13) Söllner, C.; Burghammer, M.; Busch-Nentwich, E.; Berger, J.; Schwarz, H.; Riekel, C.; Nicolson, T. Control of Crystal Size and Lattice Formation by Starmaker in Otolith Biomineralization. *Science* **2003**, *302*, 282 –286.

(14) Müller, W. E. G.; Eckert, C.; Kropf, K.; Wang, X.; Schlossmacher, U.; Seckert, C.; Wolf, S. E.; Tremel, W.; Schröder, H. C. Formation of giant spicules in the deep-sea hexactinellid Monorhaphis chuni (Schulze 1904): electron-microscopic and biochemical studies. *Cell Tissue Res* **2007**, *329*, 363–378.

(15) Gilbert, M.; Giachelli, C. M.; Stayton, P. S. Biomimetic peptides that engage specific integrin-dependent signaling pathways and bind to calcium phosphate surfaces. *J. Biomed. Mater. Res.* **2003**, *67A*, 69–77.

(16) George, A.; Ravindran, S. Protein templates in hard tissue engineering. *Nano Today* **2010**, *5*, 254–266.

(17) Cai, Y.; Yao, J. Effect of proteins on the synthesis and assembly of calcium phosphate nanomaterials. *Nanoscale* **2010**, *2*, 1842.

(18) Xu, A.-W.; Ma, Y.; C?lfen, H. Biomimetic mineralization. *J. Mater. Chem.* **2007**, *17*, 415.

(19) Patil, A. J.; Mann, S. Self-assembly of bio–inorganic nanohybrids using organoclay building blocks. *J. Mater. Chem.* **2008**, *18*, 4605.

(20) Gower, L. B. Biomimetic Model Systems for Investigating the Amorphous Precursor Pathway and Its Role in Biomineralization. *Chemical Reviews* **2008**, *108*, 4551–4627.

(21) Dickerson, M. B.; Sandhage, K. H.; Naik, R. R. Protein- and Peptide-Directed Syntheses of Inorganic Materials. *Chemical Reviews* **2008**, *108*, 4935–4978.

(22) Tahir, M. N.; Théato, P.; Müller, W. E. G.; Schröder, H. C.; Borejko, A.; Faiß, S.; Janshoff, A.; Huth, J.; Tremel, W. Formation of layered titania and zirconia catalysed by surface-bound silicatein. *Chem. Commun.* **2005**, 5533.

(23) Yang, L.; Xing, R.; Shen, Q.; Jiang, K.; Ye, F.; Wang, J.; Ren, Q. Fabrication of protein-conjugated silver sulfide nanorods in the bovine serum albumin solution. *J Phys Chem B* **2006**, *110*, 10534–10539.

(24) Shiomi, T.; Tsunoda, T.; Kawai, A.; Mizukami, F.; Sakaguchi, K. Biomimetic Synthesis of Lysozyme−Silica Hybrid Hollow Particles Using Sonochemical Treatment: Influence of pH and Lysozyme Concentration on Morphology. *Chemistry of Materials* **2007**, *19*, 4486–4493.

(25) Enlow, D.; Rawal, A.; Kanapathipillai, M.; Schmidt-Rohr, K.; Mallapragada, S.; Lo, C.-T.; Thiyagarajan, P.; Akinc, M. Synthesis and characterization of self-assembled block copolymer templated calcium phosphate nanocomposite gels. *J. Mater. Chem.* **2007**, *17*, 1570.

(26) Kanapathipillai, M.; Yusufoglu, Y.; Rawal, A.; Hu, Y.-Y.; Lo, C.-T.; Thiyagarajan, P.; Kalay, Y. E.; Akinc, M.; Mallapragada, S.; Schmidt-Rohr, K. Synthesis and Characterization of Ionic Block Copolymer Templated Calcium Phosphate Nanocomposites. *Chemistry of Materials* **2008**, *20*, 5922–5932.

(27) Gajjeraman, S.; He, G.; Narayanan, K.; George, A. Biological Assemblies Provide Novel Templates for the Synthesis of Biocomposites and Facilitate Cell Adhesion. *Adv. Funct. Mater.* **2008**, *18*, 3972–3980.

(28) de la Rica, R.; Matsui, H. Applications of peptide and protein-based materials in bionanotechnology. *Chem. Soc. Rev.* **2010**, *39*, 3499.

(29) Sarikaya, M.; Tamerler, C.; Jen, A. K.-Y.; Schulten, K.; Baneyx, F. Molecular biomimetics: nanotechnology through biology. *Nat Mater* **2003**, *2*, 577–585.

(30) Salgado, A. J.; Coutinho, O. P.; Reis, R. L. Bone tissue engineering: state of the art and future trends. *Macromol Biosci* **2004**, *4*, 743–765.

(31) Hu, Y.-Y.; Rawal, A.; Schmidt-Rohr, K. Strongly bound citrate stabilizes the apatite nanocrystals in bone. *Proceedings of the National Academy of Sciences* **2010**, *107*, 22425 –22429.

(32) Rey, C.; Combes, C.; Drouet, C.; Glimcher, M. J. Bone mineral: update on chemical composition and structure. *Osteoporos Int* **2009**, *20*, 1013–1021.

(33) Cui, F.-Z.; Li, Y.; Ge, J. Self-assembly of mineralized collagen composites. *Materials Science and Engineering: R: Reports* **2007**, *57*, 1–27.

(34) Prockop, J. D. Collagens: Molecular Biology, Diseases, and Potentials for Therapy. *Annu. Rev. Biochem.* **1995**, *64*, 403–434.

(35) Wang, Y.; Yang, C.; Chen, X.; Zhao, N. Biomimetic Formation of Hydroxyapatite/collagen Matrix Composite. *Adv. Eng. Mater.* **2006**, *8*, 97–100.

(36) Liao, S.; Ngiam, M.; Chan, C. K.; Ramakrishna, S. Fabrication of nano-hydroxyapatite/collagen/osteonectin composites for bone graft applications. *Biomed. Mater.* **2009**, *4*, 025019.

(37) Kikuchi, M.; Ikoma, T.; Itoh, S.; Matsumoto, H. N.; Koyama, Y.; Takakuda, K.; Shinomiya, K.; Tanaka, J. Biomimetic synthesis of bone-like nanocomposites using the self-organization mechanism of hydroxyapatite and collagen. *Composites Science and Technology* **2004**, *64*, 819–825.

(38) Tampieri, A.; Celotti, G.; Landi, E.; Sandri, M.; Roveri, N.; Falini, G. Biologically inspired synthesis of bone-like composite: Self-assembled collagen fibers/hydroxyapatite nanocrystals. *J. Biomed. Mater. Res.* **2003**, *67A*, 618–625.

(39) Fujii, T.; Tanaka, T.; Ohkawa, K. Biomineralization of calcium phosphate on human hair protein film and formation of a novel hydroxyapatite-protein composite material. *J. Biomed. Mater. Res.* **2009**, *91B*, 528–536.

(40) Arakaki, A.; Webb, J.; Matsunaga, T. A Novel Protein Tightly Bound to Bacterial Magnetic Particles in Magnetospirillum magneticum Strain AMB-1. *Journal of Biological Chemistry* **2003**, *278*, 8745 –8750.

(41) Prozorov, T.; Mallapragada, S. K.; Narasimhan, B.; Wang, L.; Palo, P.; Nilsen-Hamilton, M.; Williams, T. J.; Bazylinski, D. A.; Prozorov, R.; Canfield, P. C. Protein-Mediated Synthesis of Uniform Superparamagnetic Magnetite Nanocrystals. *Adv. Funct. Mater.* **2007**, *17*, 951–957.

(42) Prozorov, T.; Palo, P.; Wang, L.; Nilsen-Hamilton, M.; Jones, D.; Orr, D.; Mallapragada, S. K.; Narasimhan, B.; Canfield, P. C.; Prozorov, R. Cobalt Ferrite Nanocrystals: Out-Performing Magnetotactic Bacteria. *ACS Nano* **2007**, *1*, 228–233.

(43) Wang, X.; Wiens, M.; Schröder, H. C.; Hu, S.; Mugnaioli, E.; Kolb, U.; Tremel, W.; Pisignano, D.; Müller, W. E. G. Morphology of Sponge Spicules: Silicatein a Structural Protein for Bio-Silica Formation. *Adv. Eng. Mater.* **2010**, *12*, B422–B437.

(44) Brutchey, R. L.; Morse, D. E. Silicatein and the Translation of its Molecular Mechanism of Biosilicification into Low Temperature Nanomaterial Synthesis. *Chemical Reviews* **2008**, *108*, 4915–4934.

(45) Kröger, N.; Dickerson, M. B.; Ahmad, G.; Cai, Y.; Haluska, M. S.; Sandhage, K. H.; Poulsen, N.; Sheppard, V. C. Bioenabled Synthesis of Rutile (TiO2) at Ambient Temperature and Neutral pH. *Angew. Chem.* **2006**, *118*, 7397–7401.

(46) Sumerel, J. L.; Yang, W.; Kisailus, D.; Weaver, J. C.; Choi, J. H.; Morse, D. E. Biocatalytically Templated Synthesis of Titanium Dioxide. *Chemistry of Materials* **2003**, *15*, 4804–4809.

(47) Curnow, P.; Bessette, P. H.; Kisailus, D.; Murr, M. M.; Daugherty, P. S.; Morse, D. E. Enzymatic Synthesis of Layered Titanium Phosphates at Low Temperature and Neutral pH by Cell-Surface Display of Silicatein-α. *Journal of the American Chemical Society* **2005**, *127*, 15749–15755.

(48) Kisailus, D.; Truong, Q.; Amemiya, Y.; Weaver, J. C.; Morse, D. E. Self-Assembled Bifunctional Surface Mimics an Enzymatic and Templating Protein for the Synthesis of a Metal Oxide Semiconductor. *PNAS* **2006**, *103*, 5652–5657.

(49) Brutchey, R. L.; Yoo, E. S.; Morse, D. E. Biocatalytic Synthesis of a Nanostructured and Crystalline Bimetallic Perovskite-like Barium Oxofluorotitanate at Low Temperature. *Journal of the American Chemical Society* **2006**, *128*, 10288–10294.

(50) Jensen, M.; Keding, R.; Höche, T.; Yue, Y. Biologically Formed Mesoporous Amorphous Silica. *Journal of the American Chemical Society* **2009**, *131*, 2717–2721.

(51) Tahir, M. N.; Theato, P.; Muller, W. E. G.; Schroder, H. C.; Janshoff, A.; Zhang, J.; Huth, J.; Tremel, W. Monitoring the formation of biosilica catalysed by histidine-tagged silicatein. *Chem. Commun.* **2004**, 2848.

(52) Bansal, V.; Rautaray, D.; Bharde, A.; Ahire, K.; Sanyal, A.; Ahmad, A.; Sastry, M. Fungus-mediated biosynthesis of silica and titania particles. *J. Mater. Chem.* **2005**, *15*, 2583.

(53) Bansal, V.; Rautaray, D.; Ahmad, A.; Sastry, M. Biosynthesis of zirconia nanoparticles using the fungus Fusarium oxysporum. *J. Mater. Chem.* **2004**, *14*, 3303–3305.

(54) Zhao, X.; Pan, F.; Xu, H.; Yaseen, M.; Shan, H.; Hauser, C. A. E.; Zhang, S.; Lu, J. R. Molecular self-assembly and applications of designer peptide amphiphiles. *Chem. Soc. Rev.* **2010**, *39*, 3480.

(55) Chung, W.-J.; Kwon, K.-Y.; Song, J.; Lee, S.-W. Evolutionary Screening of Collagen-like Peptides That Nucleate Hydroxyapatite Crystals. *Langmuir* **0**, *0*.

(56) Hu, Y.-Y.; Yusufoglu, Y.; Kanapathipillai, M.; Yang, C.-Y.; Wu, Y.; Thiyagarajan, P.; Deming, T.; Akinc, M.; Schmidt-Rohr, K.; Mallapragada, S. Self-assembled calcium phosphate nanocomposites using block copolypeptide templates. *Soft Matter* **2009**, *5*, 4311.

(57) Yusufoglu, Y.; Hu, Y.; Kanapathipillai, M.; Kramer, M.; Kalay, Y. E.; Thiyagarajan, P.; Akinc, M.; Schmidt-Rohr, K.; Mallapragada, S. Bioinspired synthesis of self-assembled calcium phosphate nanocomposites using block copolymer-peptide conjugates. *Journal of Materials Research* **2008**, *23*, 3196–3212.

(58) Hartgerink, J. D.; Beniash, E.; Stupp, S. I. Self-Assembly and Mineralization of Peptide-Amphiphile Nanofibers. *Science* **2001**, *294*, 1684 –1688.

(59) Xu, H.; Wang, Y.; Ge, X.; Han, S.; Wang, S.; Zhou, P.; Shan, H.; Zhao, X.; Lu, J. R. Twisted Nanotubes Formed from Ultrashort Amphiphilic Peptide I3K and Their Templating for the Fabrication of Silica Nanotubes. *Chemistry of Materials* **2010**, *22*, 5165–5173.

(60) Loweth, C. J.; Caldwell, W. B.; Peng, X.; Alivisatos, A. P.; Schultz, P. G. DNA-Based Assembly of Gold Nanocrystals. *Angew. Chem. Int. Ed.* **1999**, *38*, 1808–1812.

(61) Ding, B.; Deng, Z.; Yan, H.; Cabrini, S.; Zuckermann, R. N.; Bokor, J. Gold Nanoparticle Self-Similar Chain Structure Organized by DNA Origami. *Journal of the American Chemical Society* **2010**, *132*, 3248–3249.

(62) Zhang, J.; Liu, Y.; Ke, Y.; Yan, H. Periodic Square-Like Gold Nanoparticle Arrays Templated by Self-Assembled 2D DNA Nanogrids on a Surface. *Nano Letters* **2006**, *6*, 248–251.

(63) Wang, Z.; Zhang, J.; Ekman, J. M.; Kenis, P. J. A.; Lu, Y. DNA-Mediated Control of Metal Nanoparticle Shape: One-Pot Synthesis and Cellular Uptake of Highly Stable and Functional Gold Nanoflowers. *Nano Letters* **2010**, *10*, 1886–1891.

(64) Park, D.-H.; Kim, J.-E.; Oh, J.-M.; Shul, Y.-G.; Choy, J.-H. DNA Core@Inorganic Shell. *Journal of the American Chemical Society* **2010**, *132*, 16735–16736.

(65) Liang, H.; Angelini, T. E.; Braun, P. V.; Wong, G. C. L. Roles of Anionic and Cationic Template Components in Biomineralization of CdS Nanorods Using Self-Assembled DNA−Membrane Complexes. *Journal of the American Chemical Society* **2004**, *126*, 14157–14165.

(66) Ma, N.; Dooley, C. J.; Kelley, S. O. RNA-Templated Semiconductor Nanocrystals. *Journal of the American Chemical Society* **2006**, *128*, 12598–12599.

(67) Arias, J. L.; Fernández, M. S. Polysaccharides and Proteoglycans in Calcium Carbonate-based Biomineralization. *Chemical Reviews* **2008**, *108*, 4475–4482.

(68) Meyers, M. A.; Chen, P.-Y.; Lin, A. Y.-M.; Seki, Y. Biological materials: Structure and mechanical properties. *Progress in Materials Science* **2008**, *53*, 1–206.

(69) Venkatesan, J.; Kim, S.-K. Chitosan Composites for Bone Tissue Engineering—An Overview. *Marine Drugs* **2010**, *8*, 2252–2266.

(70) Li, J.; Zhu, D.; Yin, J.; Liu, Y.; Yao, F.; Yao, K. Formation of nano-hydroxyapatite crystal in situ in chitosan-pectin polyelectrolyte complex network. *Materials Science and Engineering: C* **2010**, *30*, 795–803.

(71) Zuo, G.; Wan, Y.; Wang, L.; Liu, C.; He, F.; Luo, H. Synthesis and characterization of laminated hydroxyapatite/chitosan nanocomposites. *Materials Letters* **2010**, *64*, 2126–2128.

(72) He, D.; Xiao, X. F.; Liu, F.; Liu, R. F. Hydroxyapatite nanospindles by biomimetic synthesis with chitosan as template. *Mats. Sci. Tech.* **2007**, *23*, 1228–1232.

(73) Zimmermann, K. A.; LeBlanc, J. M.; Sheets, K. T.; Fox, R. W.; Gatenholm, P. Biomimetic design of a bacterial cellulose/hydroxyapatite nanocomposite for bone healing applications. *Materials Science and Engineering: C* **2011**, *31*, 43–49.

(74) Chen, X.; Liu, Y.; Lu, H.; Yang, H.; Zhou, X.; Xin, J. H. In-situ growth of silica nanoparticles on cellulose and application of hierarchical structure in biomimetic hydrophobicity. *Cellulose* **2010**, *17*, 1103–1113.

# Chapter 3 Biomimetic Self-assembling Copolymer–Hydroxyapatite Nanocomposites with the Nanocrystal Size Controlled by Citrate

Y.-Y. Hu, X.P. Liu, X. Ma, A. Rawal, T. Prozorov, M. Akinc, S. K. Mallapragada,

K. Schmidt-Rohr*

This chapter is modified from a paper published in *Chemistry of Materials*, 2011, 23, 2481-2490. My contribution to this paper focused on the nanocomposite synthesis with different amounts of citrate, characterization and analysis of the nanocomposites using XRD, TEM and small angle neutron scattering.

## Abstract

Citrate binds strongly to the surface of calcium phosphate (apatite) nanocrystals in bone and is thought to prevent crystal thickening. In this work, citrate added as a regulatory element enabled molecular control of the size and stability of hydroxyapatite (HAp) nanocrystals in synthetic nanocomposites, fabricated with self-assembling block copolymer templates. The decrease of the HAp crystal size within the polymer matrix with increasing citrate concentration was documented by solid-state nuclear magnetic resonance (NMR) techniques and wide-angle X-ray diffraction (XRD), while the shapes of HAp nanocrystals were determined by transmission electron microscopy (TEM). Advanced NMR techniques were used to characterize the interfacial species and reveal enhanced interactions between mineral and organic matrix, concomitant with the size effects. The surface-to-volume ratios determined by NMR spectroscopy and long-range $^{31}P\{^{1}H\}$ dipolar dephasing show that 2, 10, and 40 mM citrate changes the thicknesses of the HAp crystals from 4 nm without citrate to 2.9, 2.8, and 2.3 nm, respectively. With citrate concentrations comparable to that in body fluids, HAp nanocrystals of similar sizes and morphologies as in avian and bovine bones have been produced.

**Keywords:** Bioinspired materials, biocompatibility, bone, crystal control, hybrid materials, nuclear magnetic resonance

## 3.1 Introduction

Bone, the primary supporting and protective organ of the mammalian body, is a nanocomposite of nano-sized carbonated apatite crystals and the fibrous protein collagen (ca. 40 vol% each), with smaller contributions from other proteins and water.[1–5] Human bone undergoes constant dynamic remodeling to repair fatigue damage, such as micro- cracks induced by stress.[6] However, when the damage is beyond the self-restoring ability of bone, therapeutic approaches to regenerate the mineralized tissues are desired. Ideal materials employed in tissue repair therapies should exhibit structural features similar to those in bone, be biocompatible, biodegradable, and bioactive.

A balance between mechanical properties and bioactivity should be considered in biomaterials science; composites of synthetic polymer and calcium phosphate provide a favorable combination. Among various synthesis schemes intended to mimic bone,[7] a bottom-up sol-gel method using inorganic ionic precursors and self-assembling polymers is advantageous since it can control the structure at the molecular level while inducing some hierarchical ordering as seen in bone.[8] With this method, our group has successfully demonstrated the synthesis of organic and inorganic self-assembling nanocomposites using Pluronic (polyethylene oxide-polypropylene oxide triblock copolymer) and its derivatives, polymers coupled to apatite-nucleating peptides, and $K_{170}L_{30}$ diblock copolypeptides as templates that precipitate apatite nanocrystals within the organic matrix.[9–11] Progress has been made to more closely mimic the structure of bone; for instance, hydroxyapatite has been stabilized, and the inorganic content has been increased from 15 wt% to over 50 wt%, compared to 65 wt% in bone. Similar research has been pursued by other groups. For instance, Pramanik and Kar synthesized thermoplastic apatite-poly(ether etherketone)

nanocomposites,[12] Song et al. used crosslinked polymethacrylamide and polymethacryalate hydrogels to template the formation of HAp nanoparticles,[13] and poly(lactic acid), poly(glycolic acid), and poly(ε-caprolactone)/HAp composites also have been constructed for their biodegradability.[14] However, although organic-inorganic nanocomposites have been fabricated, the regulation of the apatite crystal size and morphology has not been discussed. Nevertheless, the crystal dimensions, particularly the crystal thickness is critical to the mechanical properties of bone, in that a thickness of ~3 nm prevents the propagation of cracks.[15] Also, recent research implied that desirable osteoconductivity could be achieved with synthetic HAp resembling bone minerals in composition, size, and morphology.[16]

A most recent close examination of the interface between collagen and apatite crystals in bone by advanced solid state NMR techniques[17] has revealed that citrate, a small molecule, is the dominant organic molecule there, tightly bound to apatite and covering the surface with a density of one citrate molecule per 4 $nm^2$ (ca. 1/6 of the available area). About 80 wt% of the total citrate in the body is accumulated in bone. Carboxylate groups are key for regulating the formation of apatite[5,18] and citrate in bone provides more carboxylate groups than all the proteins other than collagen taken together. *In vitro* studies have shown that citrate at higher concentrations results in smaller HAp nanocrystals.[19,20] Moreover, citrate stabilizes HAp over other phosphates[21] and synthetic materials pretreated with citrate give better biocompatibility in tissue repair.[22,23] Despite these studies, the effect of citrate upon the local molecular composition and surface structure is not well understood. This is in part due to the challenge of selectively characterizing mineral surfaces, especially those buried in organic matrices. The surface- and structure- directing effect of small molecules is general to a wide variety of functionally important materials such as zeolites,[24] mesoporous materials,[25] and sol-gel based electronic materials,[26] in addition to biomaterials.

Inspired by the study of citrate-apatite in bone and *in vitro*, we have added citrate as a third component in our synthesis of self-assembled Pluronic polymer and HAp nanocomposites. This research allows more precise control over the crystal size and morphology of synthetic HAp within a polymer matrix in order to more closely mimic the structure and morphology of nanocrystals in bone.

## 3.2 Experimental section

### 3.2.1 Chemicals.

The Pluronic F127 block copolymer, poly(ethylene oxide)-b-poly(propylene oxide)-b-poly(ethylene oxide) (PEO-PPO-PEO), was purchased from Sigma Aldrich (St. Louis, MO). Its average molecular weight is about 12,600 kDa. An aqueous solution of the polymer can self-assemble into micelles at low temperature and concentration,[8] and transform to a viscous gel upon increase in temperature (typically above 25 ℃) or concentration. All the other chemicals in this study were purchased from Sigma Aldrich or Fisher Scientific, and used without further purification.

### 3.2.2 Nanocomposite Synthesis.

The calcium phosphate nanocomposites were prepared using self-assembling polymers as templates as follows: 0.01 mol of $Ca(NO_3)_2$ was dissolved in 10 mL of 30 wt% Pluronic F127 solution at 4 ℃, followed by addition of 0.2 mL of ammonium citrate at various concentrations and mixed for 2 hours at 4 ℃. 2 mL of 3 M $(NH_4)_2HPO_4$ was then added. The sample was brought to room temperature and allowed to form a gel with gentle stirring. $NH_4OH$ was then added to adjust the pH to 7.5-8; the pH was checked and re-adjusted to 7.5-8 after 24 h and beyond until it remained stable. Four hydrogel samples with citrate concentrations of 0, 2, 10, and 40 mM were prepared. The samples were freeze-dried and characterized.

In addition, samples were washed to remove free polymer and ammonium nitrate, as needed for characterization. The sample powder was suspended in pure water, centrifuged, and the supernatant was removed. This procedure was repeated three times in order to minimize the amount of residual free polymer and ammonium nitrate.

### 3.2.3 Characterization

**XRD.** The structure of the freeze-dried and washed samples was investigated by XRD (X'Pert PRO, PANalytical Inc., Westborough, MA,) and analyzed by X'pert Data collector. The diffractometer was operated at 45 kV and 40 mA. CuKα radiation with a wavelength of 0.15418 nm was employed. The scan rate was 0.021°/s with a step size of 0.017° over the range of $10° \leq 2\theta \leq 60°$.

**TEM**. Imaging of the samples was performed without staining with the Tecnai $G^2$ F20 Scanning Transmission Electron Microscope (STEM) (FEI Company, Hillsboro OR) equipped with High Angle Annular Dark Field (HAADF) and Energy Dispersive X-ray Spectroscopy (EDS) detectors at an operating voltage of 200 kV. Twenty microliters of a suspension of the sample were dispersed in 2 mL of distilled $H_2O$. A drop of the diluted suspension was placed on a holey carbon-supported copper grid. Multiple areas of each sample were examined to determine the average size of the particles in the nanocomposites, both in bright field TEM mode and in STEM mode.

**SANS.** Small-angle neutron scattering (SANS) was used to highlight the structure of the Pluronic block copolymer in the nanocomposite gels. 1 mL deuterium oxide ($D_2O$) was added to about 0.5 mL gel sample. The polymer phase has higher neutron scattering contrast than the inorganic phase in a deuterated solvent, since the scattering length of $^1H$ is negative while the scattering lengths of all other isotopes involved are positive and of similar magnitude.

The experiments were performed using the 30 m small angle scattering instrument on beamline NG7 at the National Center for Neutron Research, National Institute of Standards and Technology (NIST), Gaithersburg, MD. A cold neutron source with an average wavelength of 6 Å was used. The samples were sealed in quartz cylindrical cells with a 1-mm path length. The scattered neutrons were detected by a two-dimensional detector with three different sample-to-detector distances of 13, 4, and 1 m. The scattering vector, q, was varied between 0.004 $Å^{-1} < q <$ 0.56 $Å^{-1}$, where $q = (4\pi/\lambda) \sin\theta$, in which $\lambda$ is the neutron wavelength and $\theta$ is half the scattering angle. The I(q) data were placed on an absolute scale in units of $cm^{-1}$. Data reduction and plots were accomplished by using SANS reduction and analysis macros provided by NIST (http://www.ncnr.nist.gov/programs/sans/data/red_anal.html). [27]

**NMR.** The NMR study was done at Dr.Schmidt-Rohr's lab. All the NMR experiments were carried out on a Bruker Biospin DSX-400 spectrometer (Bruker-Biospin, Rheinstetten, Germany) at 400 MHz for $^{1}H$, 162 MHz for $^{31}P$, and 100 MHz for $^{13}C$. A Bruker 4-mm double resonance magic-angle spinning (MAS) probehead was used with spinning frequencies of 4.3 kHz for $^{1}H$-$^{31}P$ HetCor and $^{31}P$ spin diffusion experiments and 6.5 kHz for other experiments. The 90° pulse length was 4 μs for $^{1}H$, and 4.5 μs for $^{31}P$ and $^{13}C$.

A 200 s recycle delay was used in direct-polarization $^{31}P$ NMR experiments without or with two rotor periods of gated $^{1}H$-$^{31}P$ heteronuclear recoupling. The two-pulse phase-modulation (TPPM) $^{1}H$-$^{31}P$ heteronuclear decoupling strength was 60 kHz during $^{31}P$ detection. Hartman-Hahn cross-polarization (CP) of 1 ms was employed for experiments requiring polarization transfer from $^{1}H$ to $^{31}P$ or $^{13}C$. $^{13}C$ NMR spectra were acquired after cross polarization from $^{1}H$ and suppression of sidebands (TOSS), at $\nu_r$ = 5.3 kHz, with a 1-s recycle delay and 6700 scans per spectrum. $^{1}H$-$^{31}P$ HetCor experiments were carried out with MREV-8 for $^{1}H$-$^{1}H$ homonuclear

decoupling and $^{1}H$ chemical shifts were scaled by 0.47 accordingly during data processing. 160 $t_1$ increments of 60 μs were employed and multi-echo detection[28] was implemented to enhance signal sensitivity. In $^{31}P$ spin diffusion experiments, a short CP contact time of 0.1 ms was employed to generate $^{31}P$ magnetization selectively in phosphates close to protons with subsequent 0.1-ms and 1-s $^{31}P$ spin diffusion times. A spin diffusion time of 100 s was used in a sample without citrate and containing two phosphate phases. The duration of the z-period was incremented in 8 steps of $t_r/8 = 29.1$ μs in order to cancel dispersive contributions to the spinning sidebands, which would results in baseline distortions. $^{1}H$-$^{31}P$ HARDSHIP experiments[29] were performed with direct polarization and recoupling times of 0.3, 0.6, 0.9, 2.1, 3.0, 4.6, 6.1, 7.7, and 9.2 ms. Differential $T_2$ relaxation of surface and core phosphate signals in $S_0$ was corrected for as outlined in ref.[24]. The NIST hydroxyapatite $^{1}H$ peak at 0.18 ppm and $^{31}P$ peak at 2.8 ppm was used to calibrate $^{1}H$ and $^{31}P$ chemical shifts, respectively.

Avian and bovine bones used in HARDSHIP experiments were extracted from the mid-sections of femur bones from a mature hen and a 4-year-old cow. The surface was cleaned with a scalpel to remove muscle tissue and then washed with a solution of methanol and chloroform to remove lipids. The bone was ground to a powder and lyophilized to remove any traces of solvent and bulk water.

### 3.3 Results and Discussion

The properties of synthetic nanocomposites are strongly dependent on the mineral size, composition, and the surface structure as well as its interaction with the surrounding organic matrix. Mineralization of an organic matrix increases the mechanical strength provided that the mineral is distributed uniformly and has molecular-level interactions with the templating organic matrix. XRD, TEM, SANS, and NMR are a powerful set of complementary techniques that yield

information about the size of the mineral nanocrystals as well as the effect of mineralization on the structure of the templating organic polymer. 1D and 2D NMR techniques uniquely enable selective molecular characterization of the nanocrystal surface and core, as well as the mineral–organic interactions, from which insights about the influence of citrate and formation of the nanocomposites can be obtained.

**XRD.** XRD patterns of the four synthesized samples after freeze drying and after washing are shown in Figures 3.1 and 3.2, respectively. When compared to the pure NIST hydroxyapatite (HAp) pattern, the patterns show similarities and differences. The peaks in the diffraction pattern, in particular the intense bands at approximately $2\theta = 32°$ and $2\theta = 26°$, confirm that the mineralized phase is predominantly HAp. While the patterns of the synthesized materials differ from those of NIST HAp in showing much broader peaks, they are very similar to those of human bone and dentin.[30] The broad peak at approximately $2\theta = 32°$ is a composite band contributed from three of the most intense peaks of HAp [(211), (112), and (300) planes]. These broad peaks are indicative of the formation of HAp crystals in the low nanometer size range. Additional diffraction peaks seen in Figure 3.1 at $2\theta = 21°$ and $2\theta = 24°$ were assigned to crystalline polyethylene oxide[11] which was confirmed by the much reduced intensity of these two peaks after removal of the polymer by washing (see Figure 3.2). Most importantly, it is seen from Figure 3.2 that as the concentration of citrate in the synthesis was increased, the diffraction peaks broadened, which indicates that the size of the HAp nanocrystals is decreased. This is consistent with the NMR results, as discussed in more detail below.

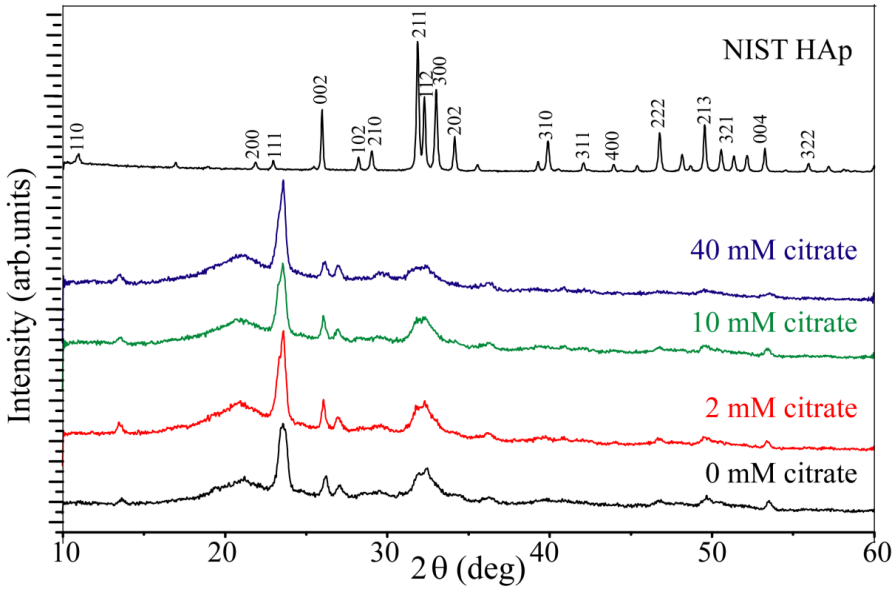


Figure 3.1 XRD patterns of Pluronic polymer-hydroxyapaite nanocomposite samples with different citrate concentrations after freeze drying. The diffraction pattern of NIST HAp is shown for reference.

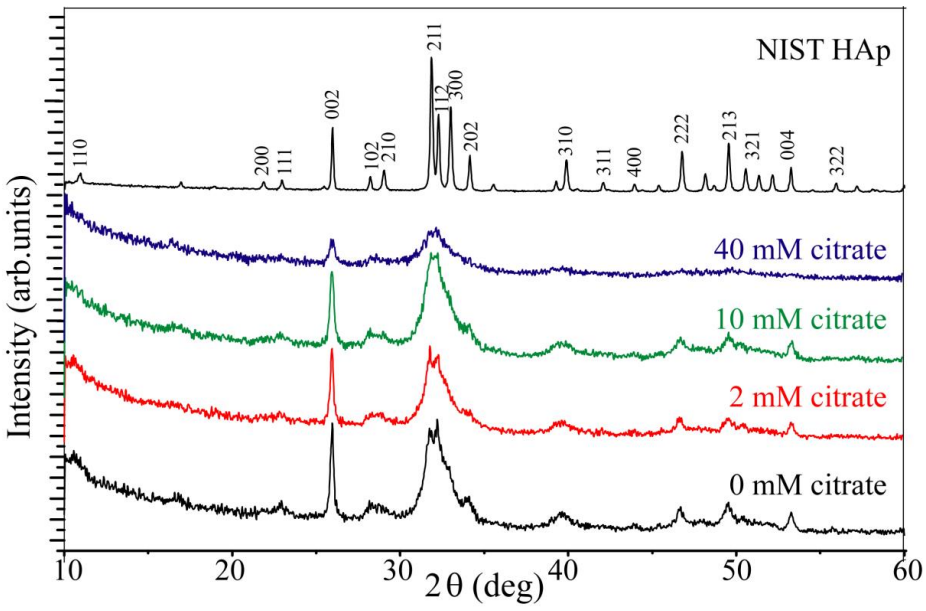


Figure 3.2 XRD patterns of Pluronic polymer-hydroxyapatite nanocomposites after washing. The diffraction pattern of NIST HAp is shown for reference.

**TEM.** HAADF-STEM is sensitive to scattered electrons generated in proportion to the atomic number (*Z*) of the atoms in the specimen. It can be used for obtaining compositional and morphological information of a sample (Z-contrast imaging), where contrast varies roughly as a function of $Z^2$.[31,32] It is, therefore, possible to image high-*Z* species inside a densely populated lower-Z environment of a nanocomposite specimen. Example of such analysis of the unwashed hydroxyapatite samples is shown in Figure 3.3. Dark-field (DF) images are obtained with HAADH-STEM at the magnification of 110,000. Here the bright spots correspond to the calcium-rich thicker areas of the nanocomposite. According to Figure 3.3, the sample prepared with the highest concentration of citrate has the shortest and thinnest particles.

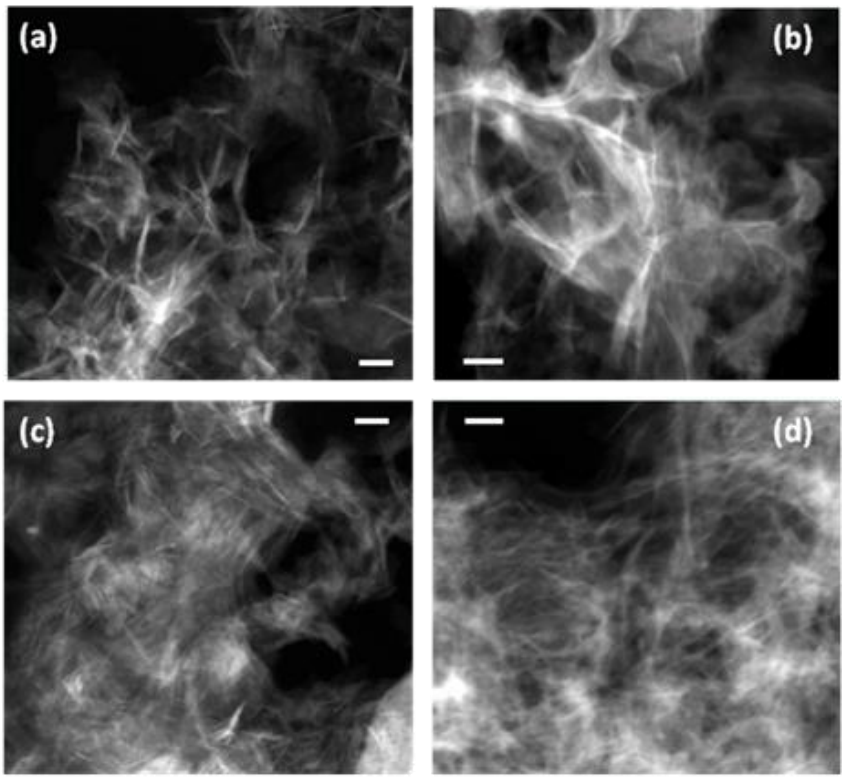


Figure 3.3 HAADF-STEM images of hydroxyapatite nanocrystals fabricated within a Pluronic polymer matrix using different citrate concentrations: (a) 0 mM; (b) 2 mM; (c) 10 mM; (d) 40 mM. All scale bars are 50 nm.

Figure 3.4 shows Bright-Field (BF) Transmission Electron Micrographs obtained at a magnification of 88,000. Analysis both in the BF TEM mode and HAADF-STEM mode reveals elongated particles of approximately 5 nm thickness and a mean particle length of 50 nm. These data are in good agreement with the results from the other techniques.

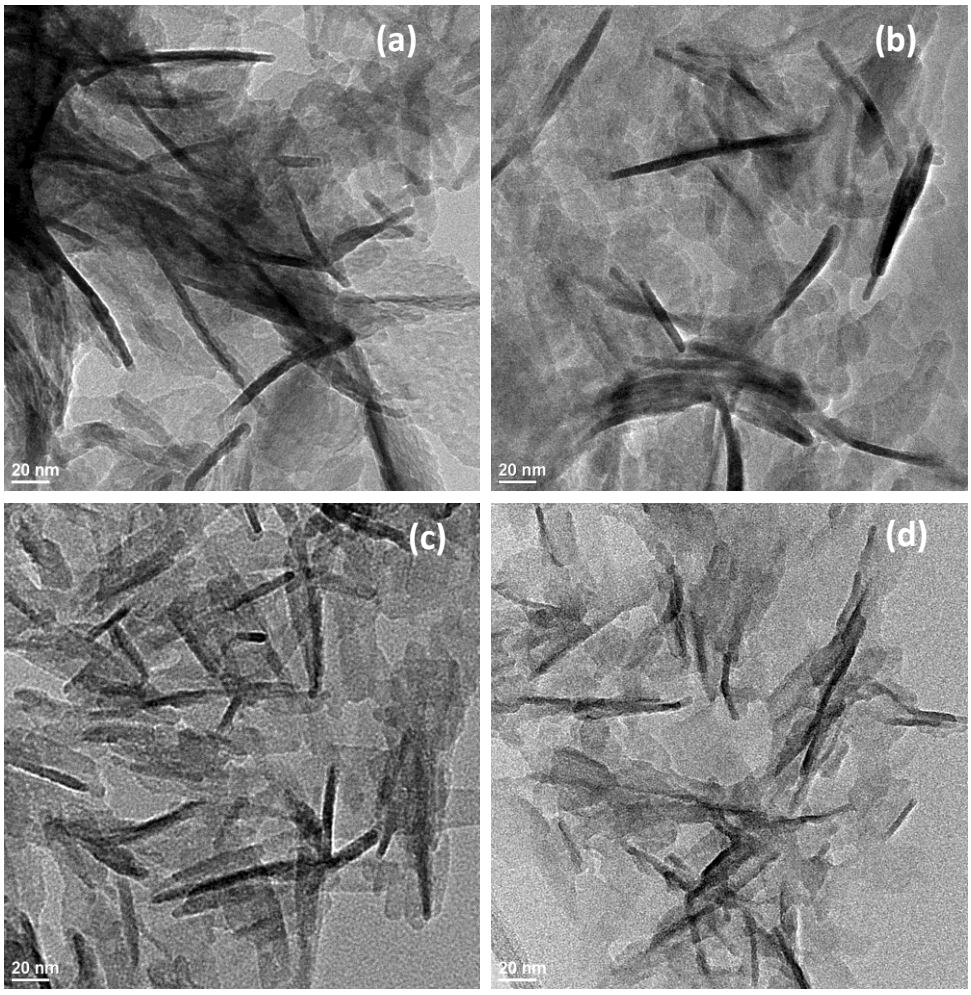


Figure 3.4 Bright field TEM images of hydroxyapatite nanocrystals fabricated within a Pluronic polymer matrix using different citrate concentrations: (a) 0 mM; (b) 2 mM; (c) 10 mM; (d) 40 mM. The magnification is 88,000, and scale bars are 20 nm.

**SANS.** Figure 3.5 shows SANS data in a plot of log I(q) vs. log (q) for Pluronic polymer-hydroxyapatite nanocomposite gels with different citrate concentrations. Due to the small neutron scattering contrast between $D_2O$ and calcium phosphate, whose isotopes all have positive scattering lengths of similar magnitudes, the inorganic component is essentially invisible here. This enables selective observation of the structure of the polymer micelles. For all four samples, a pronounced peak is observed at essentially the same $q_{max}$ of 3 $A^{-1}$, which corresponds to a characteristic length scale of ca. 15 nm. This peak was observed previously for the neat hydrated Pluronic material and shown to be due to the self-organization of the triblock copolymer into micelles[11]. The fact that the observed scattering pattern is very similar for the different samples indicates that the nanocrystals as well as the citrate molecules are incorporated into the organic matrix in a manner that does not disrupt the self-assembled structure of the pluronic polymer micelles.

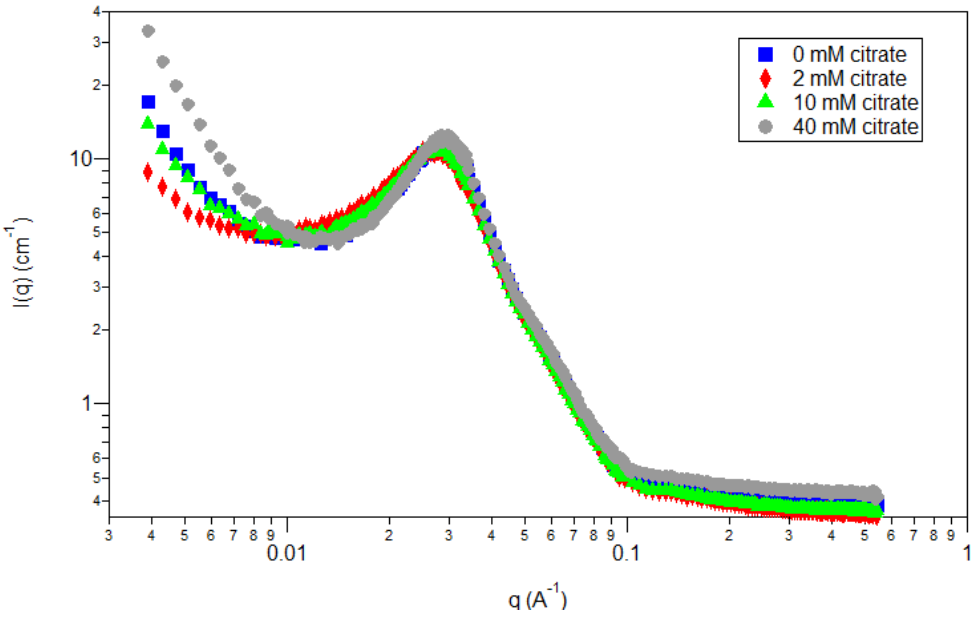


Figure 3.5 SANS curves of Pluronic-hydroxyapatite nanocomposites fabricated using different citrate concentrations.

**NMR characterization of the synthetic composites.** Direct-polarization (DP) 1D solid state $^{31}P$ NMR spectra yield quantitative site populations of the different phosphate species precipitated in the mineral phase. Figure 3.6 shows the $^{31}P$ DP NMR spectra of composites synthesized with Pluronic polymer, calcium phosphate, and citrate of different concentrations (bold line). Analysis of spectra reveals two overlapping spectral components that are recognizable in all four samples, which correspond to two different phosphate species.[33] The first is represented by a relatively sharp peak resonating at ~2.8 ppm, characteristic of orthophosphate ($PO_4^{3-}$) in hydroxyapatite (HAp). 2D $^{1}H$-$^{31}P$ HetCor NMR further prove it to be from HAp by its connection to the $OH^-$ $^{1}H$ resonance in experiments described below. The second phosphate species exhibits a broad peak centered around 2 ppm and with a full width at half maximum (FWHM) of 5 ppm, indicating a disordered phosphate environment. The NMR signal of the phosphate species near protons ($^{1}H$) can be selectively enhanced by $^{31}P\{^{1}H\}$ cross polarization (CP). The CP spectra (Figure S1) of the samples show lineshapes different from those in the DP $^{31}P$ spectra due to this selective enhancement. In Figure S1 the signal of the disordered phosphate component is selectively enhanced over that of the HAp phosphate species. This indicates that the disordered phosphate component has a closer proximity to $^{1}H$ than the HAp component.[33]

On the other hand, based on the difference in their distance from the surface and polymer protons (which exhibit strong spin-spin interactions and therefore a short spin-spin relaxation time $T_2$), the two phosphate components can be separated by $^{1}H$-$^{31}P$ HARDSHIP NMR experiments, in which $^{31}P$ signal of the disordered phosphate is dephased (suppressed) by protons with short $T_2$ much faster than that of HAp.[29] This differential dephasing enables a deconvolution of the overlapping DP spectra of the two phosphate components into two separate components as shown in Figure 3.6 (thin lines).

Quantification of surface and core phosphates of the synthetic HAp in each sample is done by integrating the two components in the deconvoluted DP spectra in Figure 3.6. The results in Table 3.1 show that as the citrate concentration is increased from 0 to 40 mM, the amount of surface $HPO_4^{2-}/PO_4^{3-}$-$H_2O$ species nearly doubles from 27% to 52%, while the core $PO_4^{3-}$ content concomitantly decreases from 73% to 48%, which indicates that the specific surface area of the nanocrystals increases. In other words, the addition of citrate results in smaller HAp crystals.

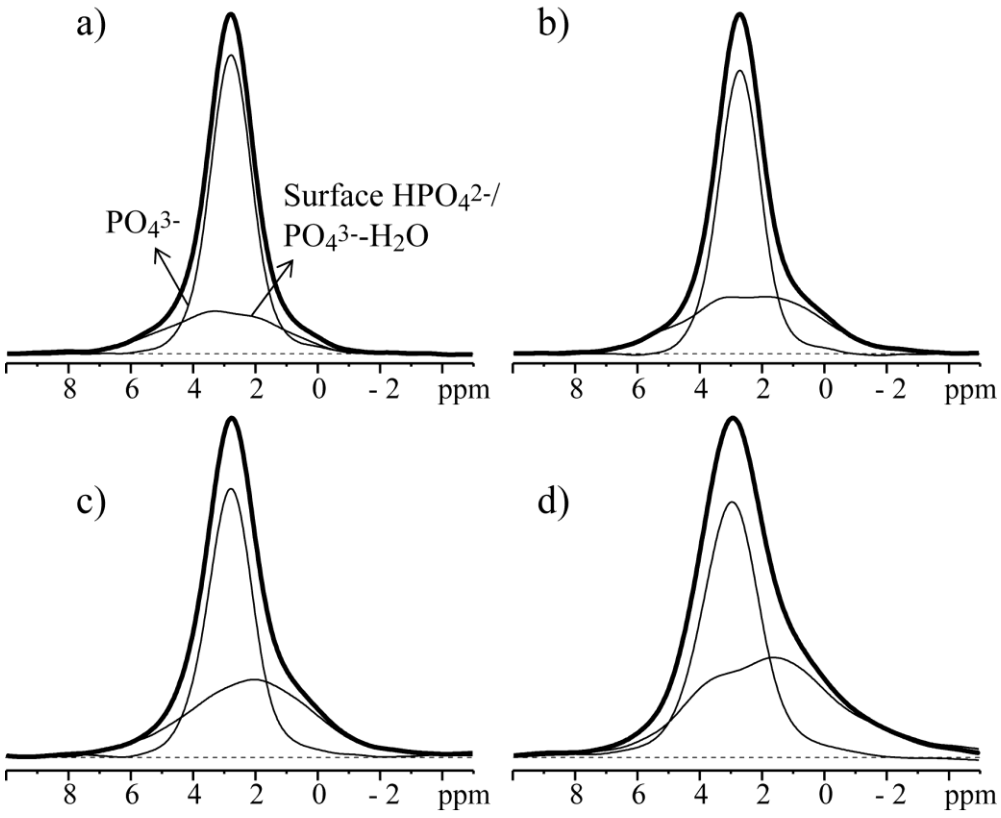


Figure 3.6 Direct polarization (DP) $^{31}P$ NMR spectra of composites synthesized with Pluronic polymer, calcium phosphate, and with ammonium citrate of different concentration. a) 0 mM citrate, b) 2 mM citrate, c) 10 mM citrate, d) 40 mM citrate. The spectra have been deconvoluted into a relatively sharp peak, obtained experimentally after long $^{31}P\{^1H\}$ HARDSHIP dephasing of surface phosphates by polymer or surface protons and assigned to the hydroxyapatite core of the nanocrystals, and a remaining broad component of surface $PO_4^{3-}/PO_4^{3-}$-$H_2O$. Magic angle spinning frequency: $\nu_r = 6.5$ kHz.

**$^{13}$C NMR of bound citrate.** Detection of the bound citrate itself is possible in $^{13}$C NMR. Figure 3.7 compares cross polarization $^{13}$C NMR spectra of the composites with 0 and 40 mM citrate. Signals at 48 and 181 ppm appearing in the citrate-containing sample must be assigned to the $CH_2$ and $COO^-$ groups of citrate, respectively,[17] while the signal of the central quaternary C-OH carbon of citrate expected near 76 ppm is hidden by overlap with the strong peak of PEO. The large width of the lines is characteristic of apatite-bound citrate,[17] while crystalline citrate shows much sharper peaks, with widths of less than 1 ppm.[17]

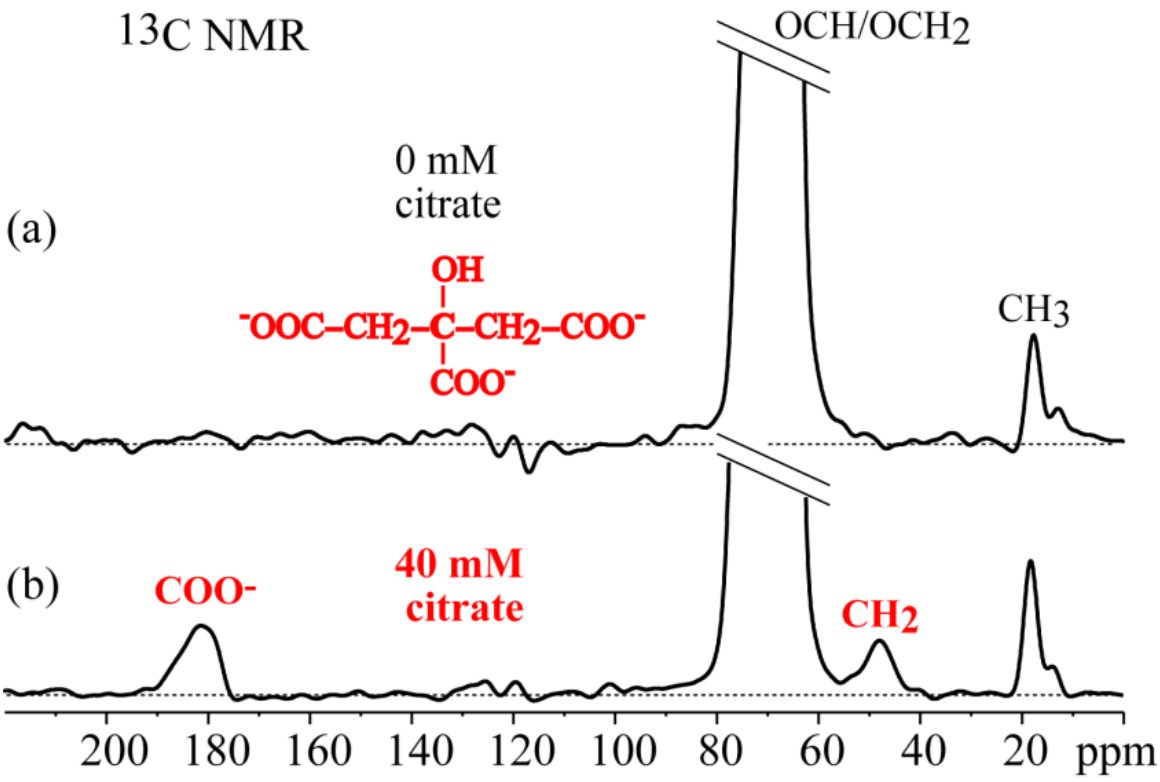


Figure 3.7 $^{13}$C CP/MAS NMR spectra of composites of Pluronic polymer and calcium phosphate synthesized with (a) 0 and (b) 40 mM ammonium citrate.

**Nanocomposite formation.** The formation of the nanocomposite is proved most convincingly by monitoring the $^{1}H$ spin diffusion from polymer protons to the mineral phase in 2D $^{1}H$-$^{31}P$ HetCor experiments.[8] With increasing $^{1}H$ spin diffusion time, the presence of the polymer $OCH_2$ (4 ppm) and $CH_3$ (1.5 ppm) peaks in the $^{1}H$-$^{31}P$ HetCor experiments (Figures 3.8 and S3, $t_{SD}$= 5, 50, and 500 ms) proves that in all four samples the mineral is in nanometer-scale contact with the organic matrix. The addition of citrate enables formation of crystals that are so small that even after a short $^{1}H$ spin diffusion time of only 0.05 ms, the $OCH_2$ proton peak at 4 ppm is observed, proving contact between the inorganic phosphate and Pluronic polymer. This is most apparent in Figure 3.8(b) for the nanocomposite synthesized with the highest citrate concentration (40 mM). At longer spin diffusion times, one can see the $^{1}H$ peak at 1.3 ppm, from $CH_3$ of the hydrophobic PPO segments at the core of the Pluronic block-copolymer micelles appear. At the same spin diffusion times, magnetization has arrived from the relatively mobile $OCH_2$/OCH of PEO and PPO, and $NH_4^+$ of the starting material $(NH_4)_2HPO_4$, whose signals appear at 4 ppm and 7.3 ppm, respectively. This is balanced by a decrease in the relative intensity of the $OH^-$ and $HPO_4^{2-}$ signals at 0.2 ppm and 11 ppm, respectively. Equilibrium of the magnetization between HAp and Pluronic polymer, evidenced by similar relative peak intensities in all $^{1}H$ cross sections, is reached within 500 ms $^{1}H$ spin diffusion in all samples. $^{1}H$ spectra taken at 1 ppm $^{31}P$ exhibit faster spin diffusion to polymer protons than those taken at 2.8 ppm, which again confirms that the disordered phosphate component is at the organic-inorganic interface.

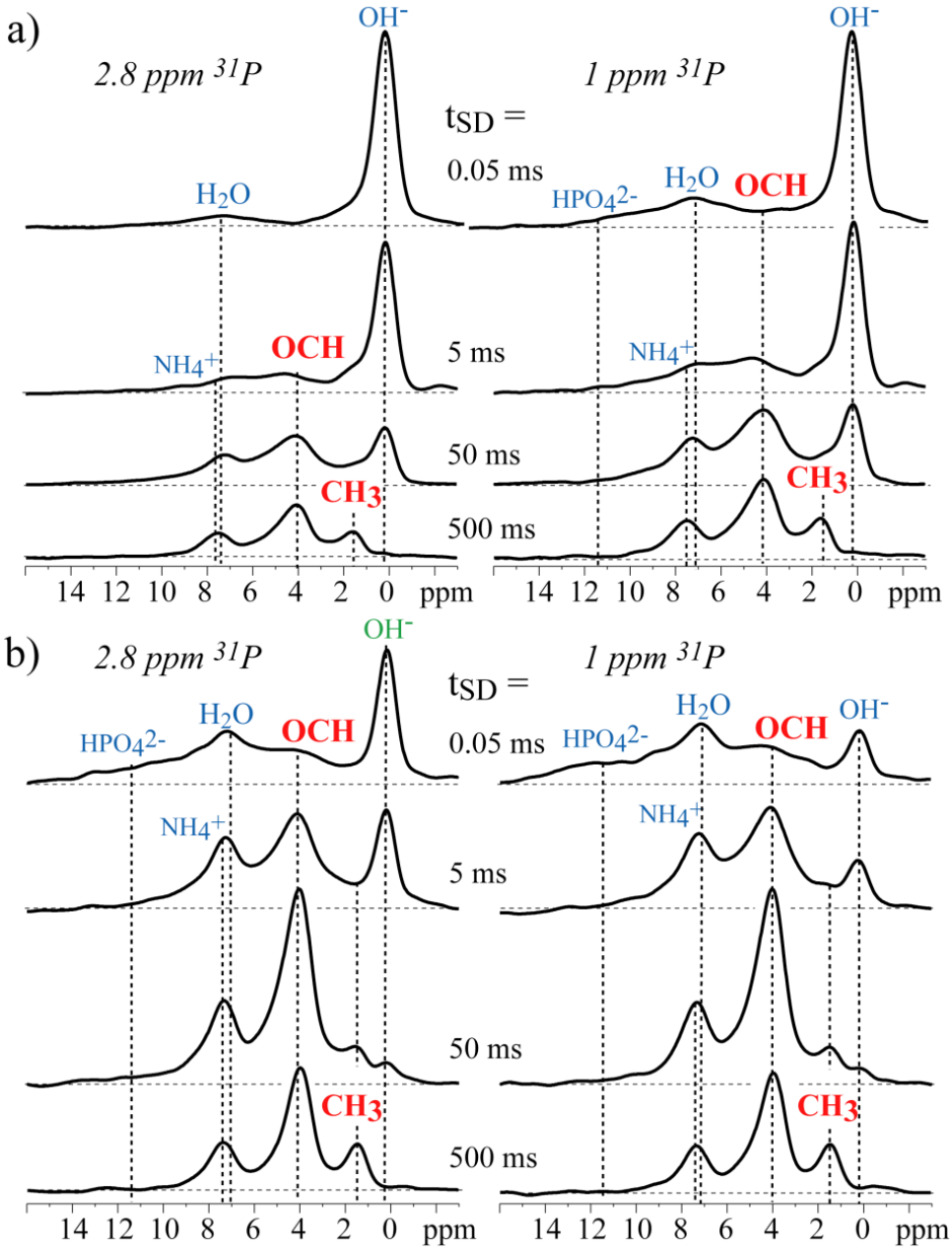


Figure 3.8 $^{1}$H spectra from cross sections taken at 2.8 ppm and 1.0 ppm $^{31}$P of 2D $^{1}$H-$^{31}$P HetCor NMR spectra of composites synthesized with Pluronic polymer, calcium phosphate, and a) 0 mM, and b) 40 mM ammonium citrate. The $^{1}$H spin diffusion times $t_{SD}$ are 0.05, 5, 50, and 500 ms.

**Nanocrystal size.** The size of the nanocrystals is crucial to the overall performance and properties of nanocomposite materials. In the present syntheses, it is also a measure of the specific molecular interactions of citrate with the mineral phase, whereby it promotes, and more importantly, stabilizes the HAp phase at a few nanometer thickness. The rate of $^{1}H$ spin diffusion from the organic protons to the mineral matrix, observed in a series of $^{1}H$-$^{31}P$ HetCor spectra reveals that spin diffusion between the organic and inorganic protons is faster as the citrate concentration is increased from 0 mM to 40 mM. This indicates that on average, the mineral has a larger surface area in contact with the organic phase in the 40 mM citrate sample than at lower citrate concentrations. This means that the average nanocrystal size decreases as more citrate is added. This trend is seen most clearly in a comparison of spectra from all samples after 5 ms of $^{1}H$ spin diffusion (Figure 3.9). With the intensities of the $OH^-$ peaks scaled to equal height, the spin diffusion rate can be gauged by the intensity of the polymer $^{1}H$ peaks, in particular the $OCH_2$/OCH at 4 ppm. The sample with 40 mM citrate shows the most intense $OCH_2$/OCH peak and thus the fastest $^{1}H$ spin diffusion and therefore the smallest HAp crystals, followed by the samples with 10, 2, and then 0 mM citrate. The faster spin diffusion also implies more extensive interactions between mineral and polymer matrix, which is favorable to the stability of the nanocomposite.

The thickness of HAp nanocrystals can be estimated from (i) the results of $^{1}H$-$^{31}P$ HetCor experiments with $^{1}H$ spin diffusion; (ii) the surface and core fractions derived from deconvoluted DP spectra; (iii) the width of the (310) peak in X-ray diffraction; and (iv) the $^{31}P\{^{1}H\}$ HARDSHIP signal decay. In principle, the $^{1}H$ spin diffusion time required to reach equilibrium in $^{1}H$-$^{31}P$ HetCor experiments can be used to estimate the thickness of the inorganic domain, but this requires knowledge of spin diffusion coefficients and $^{1}H$ densities in the organic and inorganic layers. Nevertheless, even without these parameters available, the thickness of apatite crystals can

still be approximately evaluated based on the similar synthetic systems in our previous published results. All the samples discussed in this paper exhibit faster spin diffusion than the Pluronic30-8 sample[11] made with Pluronic polymer and calcium phosphate salt without citrate under similar experimental conditions, which was characterized by various techniques, including wide-angle X-ray diffraction, solid state NMR, small angle neutron/X-ray scattering (SANS/SAXS), and TEM, and in which the thickness of the HAp crystals is ~ 4.8 nm. Therefore, the thickness of the HAp crystals in all the samples in this paper is < 5 nm.

With a surface phosphate layer of $d_s \approx 0.4$-nm thickness, the typical aspect ratio of crystals in bovine bone[34,35] and the surface-to-volume ratio of apatite crystals, the crystallite thickness d of the four synthetic samples presented in this paper can be estimated based on

$$\text{Fraction of surface } HPO_4^{2-} \text{ and } PO_4^{3-} = d_s \times (\text{Surface/Volume})$$

$$= d_s \times 2 \times (L \times W + L \times d + W \times d)/(L \times W \times d) \qquad (1)$$

For long thin crystals, Eq.1 simplifies to S/V ~ 2/d. Since the length (L) and width (W) of the crystals are not infinite, a more accurate estimate needs to consider changes in length and width of HAp crystals. Assuming a fixed aspect ratio of d:W:L = 1:3:6, we have S/V = 3/d according to Eq. 1 and the crystal thicknesses of the synthetic HAp range between 2.3 and 4.4 nm, as listed in Table 3.1.

For comparison, the HAp crystal diameters have also been estimated by applying the Debye-Scherrer equation

$$d = K\lambda/(B_{1/2} \cos\theta) \qquad (2)$$

to the (310) X-ray diffraction peak of the washed samples synthesized with different citrate concentrations, where K is chosen as 0.9, $\lambda$ = 0.154 nm is the x-ray wavelength, $B_{1/2}$ is the full width at half maximum (FWHM) of the diffraction peak, and $\theta = 20^{o}$ is half the diffraction angle of the (310) peak. The crystal thicknesses calculated from X-ray diffraction, see Table 3.1, are somewhat smaller than those estimated from the phosphate compositions. This can be attributed to the disordered surface layers (> 0.6 nm thickness combined) that may not contribute to the coherent scattering.

Analysis of $^{31}P\{^{1}H\}$ HARDSHIP NMR data by curve fitting[29] gives crystal thicknesses between 3.5 and 2.2 nm, again for d:W:L = 1:3:6 and with 2 x 0.3 nm of surface layers beyond the surface phosphorus layers. The thickness values obtained from HARDSHIP, listed in Table 3.1, are similar to those from the surface-top-volume ratio.

Our data show no indications of a broad distribution of crystallite thicknesses. The various crystallites in each micrograph of Figure 3.4 show similar thicknesses, and the Bragg peaks in the XRD patterns of Figure 3.2 seem to have a fairly homogeneous envelope, rather than broad and narrow components from small and large crystallites, respectively. The fairly good agreement in the thickness values obtained by different methods is also an indication of a fairly narrow thickness distribution. Finally, the broadening of the narrow component in the $^{31}P$ NMR spectra of Figure 3.6 with decreasing crystal thickness indicates that the cores of most crystallites are subject to more disorder as the crystallites get thinner; this rules out the assignment of that narrow component to a set of thick crystals.

**Mechanism of apatite crystal size reduction by citrate.** The three carboxyl groups of citrate have $pK_a$ values of 3.1, 4.8, and 6.4, therefore, at pH =7.5-8, they are completely ionized and can bind strongly to $Ca^{2+}$ on the HAp surface. In studies of citrate in natural bone[36] or of citrate interacting with HAp *in vitro*,[19,20,22,37] citrate is found on the surface of apatite crystals

without being incorporated within the crystal lattice, due to the relatively larger size of citrate molecules compared with lattice ions, such as phosphate or $OH^-$; this indicates that once citrate molecule occupies certain surface area of growing apatite, the further crystal growth on top of that area will be terminated unless the citrate molecule departs. In addition, surface bound citrate molecules generate a negatively charged surface area[17a], which repels negatively charged phosphate ions, thus inhibiting further crystal growth. Via electrostatic repulsion, the negatively charged apatite surface also prevents the aggregation of the primary crystallites into bigger particles.[19]

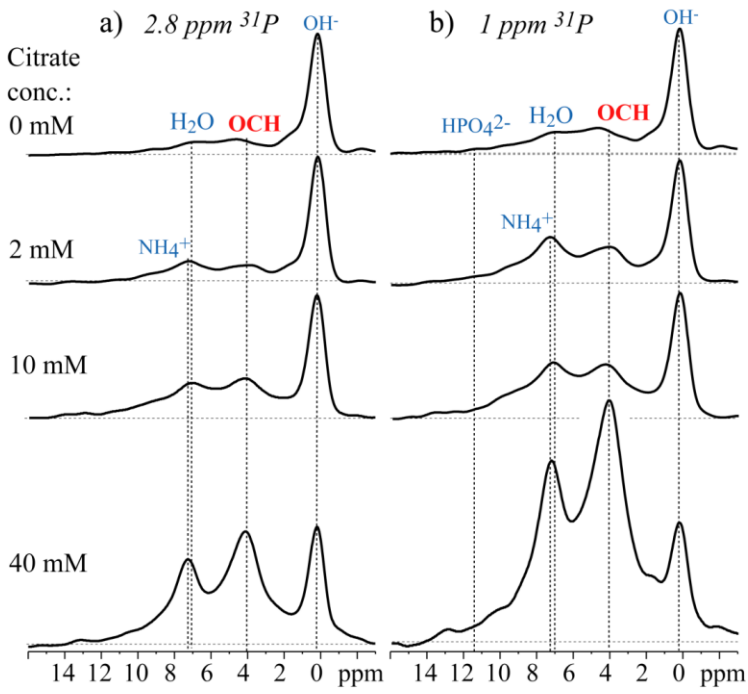


Figure 3.9 $^1H$ spectra from cross sections of 2D $^1H$-$^{31}P$ HetCor NMR spectra with 5 ms of $^1H$ spin diffusion in composites of Pluronic polymer and calcium phosphate synthesized with 0, 2, 10, or 40 mM ammonium citrate. $^1H$ spectra were taken at a) 2.8 ppm $^{31}P$, b) 1.0 ppm $^{31}P$. The height of the $OH^-$ peak at 0.2 ppm has been normalized for convenience of comparison.

Table 3.1 Composition of phosphates formed in Pluronic polymer and HAp nanocomposites with different citrate concentrations quantified based on the deconvolution of the DP spectra. The estimated HAp crystal thicknesses based on the ratio of surface phosphates ($HPO_4^{2-}$ and $PO_4^{3-}$-$H_2O$) and the total phosphates are also listed and compared with the thicknesses calculated by applying the Debye-Scherrer formula to the (310) peak in the wide-angle X-ray diffraction patterns of the washed samples. The uncertainties of the thickness values are also specified.

| Citrate Concentration | Core $PO_4^{3-}$ | Surface $HPO_4^{2-}$ and $PO_4^{3-}$-$H_2O$ | Estimated crystal thickness from surface fraction ($\pm$0.5 nm) | Estimated crystal thickness HARDSHIP NMR ($\pm$20 %) | Estimated crystal diameter from X-ray diffraction ($\pm$15%) |
|---|---|---|---|---|---|
| 0 mM | 73 % | 27 % | 4.4 nm | 3.5 nm | 4.0 nm |
| 2 mM | 59 % | 41 % | 2.9 nm | 2.7 nm | 2.4 nm |
| 10 mM | 57 % | 43 % | 2.8 nm | 2.6 nm | 2.3 nm |
| 40 mM | 48 % | 52 % | 2.3 nm | 2.2 nm | 1.5 nm |

## 3.4 Conclusions

The molecular species, their relative concentrations, and the proximity of different inorganic and organic components in synthesized bone-mimicking nanocomposites have been assessed by a full complement of NMR, diffraction, and electron microscopy. Our data show that the addition of citrate in the bottom-up synthesis of self-assembled Pluronic polymer and HAp nanocomposites enables molecular control over the growth of the apatite crystal size, similar as in

native bone. The combination of XRD and $^{1}H$-$^{31}P$ NMR techniques show that citrate is able to stabilize HAp crystals of extremely small thickness (2 nm, ~ 3 unit cells), over other calcium phosphate species. The mineralization of the organic matrix occurs without disturbing the supramolecular structure of the polymer gel, as documented by the nearly unchanged SANS patterns with and without citrate. The crystal size of HAp can be fine-tuned on the nanometer scale by varying the citrate concentration. By using similar concentrations of citrate as in body fluid, we have successfully produced apatite nanocrystals that mimic those in natural bone. The increase in citrate concentrations to 40 mM makes the $HPO_4^{2-}/PO_4$-$H_2O$ surface species the dominant fraction of the mineral phase, as determined by careful analysis of quantitative $^{31}P$ NMR spectra. The presence of citrate and the structural similarity of the synthetic HAp nanocrystals with bone apatite may contribute to better biocompatibility of these nanocomposites.

**Supporting Information Available:** Figures with cross-polarization $^{13}C$ NMR spectra and cross sections from $^{1}H$-$^{31}P$ HetCor spectra. This material is available free of charge via the internet at http://pubs.acs.org.

**Acknowledgements.** This work was supported by the U.S. Department of Energy, Office of Basic Energy Science, Division of Materials Sciences and Engineering. The research was performed at the Ames Laboratory. Ames Laboratory is operated for the U.S. Department of Energy by Iowa State University under Contract No. DE-AC02-07CH11358. Thanks to Dr. Jennifer O'Donnell (Iowa State University) for helping to perform the SANS experiments, and to Dr. Bosiljka Njegic for help with the TOC figure.

## References

(1) Buckwalter, J. A.; Glimcher, M. J.; Cooper, R. R.; Recker, R. Bone Biology. *JBJS* **1995**, *77*, 1256–1275.

(2) Rey, C.; Combes, C.; Drouet, C.; Glimcher, M. Erratum to: Bone mineral: update on chemical composition and structure. *Osteoporosis International* **2009**, *20*, 2155–2155.

(3) Weiner, S.; Traub, W. Bone structure: from angstroms to microns. *FASEB J.* **1992**, *6*, 879–885.

(4) Weiner, S.; Wagner, H. D. THE MATERIAL BONE: Structure-Mechanical Function Relations. *Annual Review of Materials Science* **1998**, *28*, 271–298.

(5) Liao, S.; Ngiam, M.; Chan, C. K.; Ramakrishna, S. Fabrication of nano-hydroxyapatite/collagen/osteonectin composites for bone graft applications. *Biomed. Mater.* **2009**, *4*, 025019.

(6) Wasserman, N.; Brydges, B.; Searles, S.; Akkus, O. In vivo linear microcracks of human femoral cortical bone remain parallel to osteons during aging. *Bone* **2008**, *43*, 856–861.

(7) Vallet-Reg í, M. Evolution of bioceramics within the field of biomaterials. *Comptes Rendus Chimie* **2010**, *13*, 174–185.

(8) Enlow, D.; Rawal, A.; Kanapathipillai, M.; Schmidt-Rohr, K.; Mallapragada, S.; Lo, C.-T.; Thiyagarajan, P.; Akinc, M. Synthesis and characterization of self-assembled block copolymer templated calcium phosphate nanocomposite gels. *J. Mater. Chem.* **2007**, *17*, 1570.

(9) Hu, Y.-Y.; Yusufoglu, Y.; Kanapathipillai, M.; Yang, C.-Y.; Wu, Y.; Thiyagarajan, P.; Deming, T.; Akinc, M.; Schmidt-Rohr, K.; Mallapragada, S. Self-assembled calcium phosphate nanocomposites using block copolypeptide templates. *Soft Matter* **2009**, *5*, 4311.

(10) Kanapathipillai, M.; Yusufoglu, Y.; Rawal, A.; Hu, Y.-Y.; Lo, C.-T.; Thiyagarajan, P.; Kalay, Y. E.; Akinc, M.; Mallapragada, S.; Schmidt-Rohr, K. Synthesis and Characterization of Ionic Block Copolymer Templated Calcium Phosphate Nanocomposites. *Chemistry of Materials* **2008**, *20*, 5922–5932.

(11) Yusufoglu, Y.; Hu, Y.; Kanapathipillai, M.; Kramer, M.; Kalay, Y. E.; Thiyagarajan, P.; Akinc, M.; Schmidt-Rohr, K.; Mallapragada, S. Bioinspired synthesis of self-assembled calcium phosphate nanocomposites using block copolymer-peptide conjugates. *Journal of Materials Research* **2008**, *23*, 3196–3212.

(12) Pathak, A.; Kulkarni, S. D.; Date, S. K.; Pramanik, P. New reagents for the chemical synthesis of fine rare-earth orthoferrite powders. *Nanostructured Materials* **1997**, *8*, 101–117.

(13) Song, J.; Malathong, V.; Bertozzi, C. R. Mineralization of Synthetic Polymer Scaffolds: A Bottom-Up Approach for the Development of Artificial Bone. *Journal of the American Chemical Society* **2005**, *127*, 3366–3372.

(14) Armentano, I.; Dottori, M.; Fortunati, E.; Mattioli, S.; Kenny, J. M. Biodegradable polymer matrix nanocomposites for tissue engineering: A review. *Polymer Degradation and Stability* **2010**, *95*, 2126–2146.

(15) Gao, H.; Ji, B.; J äger, I. L.; Arzt, E.; Fratzl, P. Materials Become Insensitive to Flaws at Nanoscale: Lessons from Nature. *PNAS* **2003**, *100*, 5597–5600.

(16) Gay, S.; Arostegui, S.; Lemaitre, J. Preparation and characterization of dense nanohydroxyapatite/PLLA composites. *Materials Science and Engineering: C* **2009**, *29*, 172–177.

(17) Hu, Y.-Y.; Rawal, A.; Schmidt-Rohr, K. Strongly Bound Citrate Stabilizes the Apatite Nanocrystals in Bone. *PNAS* **2010**, *107*, 22425–22429.

(18) Sato, K.; Kumagai, Y.; Tanaka, J. Apatite formation on organic monolayers in simulated body environment. *Journal of Biomedical Materials Research* **2000**, *50*, 16–20.

(19) Martins, M. A.; Santos, C.; Almeida, M. M.; Costa, M. E. V. Hydroxyapatite micro- and nanoparticles: nucleation and growth mechanisms in the presence of citrate species. *J Colloid Interface Sci* **2008**, *318*, 210–216.

(20) López-Macipe, A.; Gómez-Morales, J.; Rodríguez-Clemente, R. Nanosized Hydroxyapatite Precipitation from Homogeneous Calcium/Citrate/Phosphate Solutions Using Microwave and Conventional Heating. *Advanced Materials* **1999**, *10*, 49–53.

(21) Jiang, W.; Chu, X.; Wang, B.; Pan, H.; Xu, X.; Tang, R. Biomimetically Triggered Inorganic Crystal Transformation by Biomolecules: A New Understanding of Biomineralization. *J. Phys. Chem. B* **2009**, *113*, 10838–10844.

(22) Hempel, U.; Reinstorf, A.; Poppe, M.; Fischer, U.; Gelinsky, M.; Pompe, W.; Wenzel, K. W. Proliferation and differentiation of osteoblasts on Biocement D modified with collagen type I and citric acid. *Journal of Biomedical Materials Research Part B: Applied Biomaterials* **2004**, *71B*, 130–143.

(23) Schneiders, W.; Reinstorf, A.; Pompe, W.; Grass, R.; Biewener, A.; Holch, M.; Zwipp, H.; Rammelt, S. Effect of modification of hydroxyapatite/collagen composites with sodium citrate, phosphoserine, phosphoserine/RGD-peptide and calcium carbonate on bone remodelling. *Bone* **2007**, *40*, 1048–1059.

(24) Burton, A. W. A Priori Phase Prediction of Zeolites: Case Study of the Structure-Directing Effects in the Synthesis of MTT-Type Zeolites. *J. Am. Chem. Soc.* **2007**, *129*, 7627–7637.

(25) Taguchi, A.; Schüth, F. Ordered mesoporous materials in catalysis. *Microporous and Mesoporous Materials* **2005**, *77*, 1–45.

(26) Reisfeld, R.; Saraidarov, T. Innovative materials based on sol–gel technology. *Optical Materials* **2006**, *28*, 64–70.

(27) Kline, S. R. Reduction and analysis of SANS and USANS data using IGOR Pro. *Journal of Applied Crystallography* **2006**, *39*, 895–900.

(28) Hou, S. S.; Beyer, F. L.; Schmidt-Rohr, K. High-Sensitivity Multinuclear NMR Spectroscopy of a Smectite Clay and of Clay-Intercalated Polymer. *Solid State Nuclear Magnetic Resonance* **2002**, *22*, 110–127.

(29) Schmidt-Rohr, K.; Rawal, A.; Fang, X.-W. A new NMR method for determining the particle thickness in nanocomposites, using T2,H-selective X{} recoupling. *The Journal of Chemical Physics* **2007**, *126*, 054701–054701–16.

(30) Liao, S.; Watari, F.; Uo, M.; Ohkawa, S.; Tamura, K.; Wang, W.; Cui, F. The preparation and characteristics of a carbonated hydroxyapatite/collagen composite at room temperature. *Journal of Biomedical Materials Research Part B: Applied Biomaterials* **2005**, *74B*, 817–821.

(31) Determan, M. D.; Guo, L.; Thiyagarajan, P.; Mallapragada, S. K. Supramolecular Self-Assembly of Multiblock Copolymers in Aqueous Solution. *Langmuir* **2006**, *22*, 1469–1473.

(32) Sousa, A. A.; Hohmann-Marriott, M.; Aronova, M. A.; Zhang, G.; Leapman, R. D. Determination of quantitative distributions of heavy-metal stain in biological specimens by annular dark-field STEM. *Journal of Structural Biology* **2008**, *162*, 14–28.

(33) Jäger, C.; Welzel, T.; Meyer-Zaika, W.; Epple, M. A solid-state NMR investigation of the structure of nanocrystalline hydroxyapatite. *Magnetic Resonance in Chemistry* **2006**, *44*, 573–580.

(34) Fratzl, P.; Schreiber, S.; Klaushofer, K. Bone mineralization as studied by small-angle x-ray scattering. *Connect. Tissue Res.* **1996**, *35*, 9–16.

(35) Tong, W.; Glimcher, M. J.; Katz, J. L.; Kuhn, L.; Eppell, S. J. Size and Shape of Mineralites in Young Bovine Bone Measured by Atomic Force Microscopy. *Calcified Tissue International* **2003**, *72*, 592–598.

(36) Hoang, Q. Q.; Sicheri, F.; Howard, A. J.; Yang, D. S. C. Bone recognition mechanism of porcine osteocalcin from crystal structure. *Nature* **2003**, *425*, 977–980.

(37) Rhee, S.-H.; Tanaka, J. Effect of citric acid on the nucleation of hydroxyapatite in a simulated body fluid. *Biomaterials* **1999**, *20*, 2155–2160.

# Chapter 4 Bioinspired synthesis and characterization of mesoporous zirconia templated by cationic block copolymers in aqueous media

Xunpei Liu, Qinwen Ge, Aditya Rawal, German Parada, Klaus Schmidt-Rohr, Mufit Akinc, and Surya K. Mallapragada*

This chapter is modified from a paper published in *Science of Advanced Materials*, 2013, 5, 354-365. My contribution to this work includes: developing the pluronic F127 conjugate template, characterization of the conjugates by DLS and FPLC, synthesis of the pentablock copolymer, synthesis of the mesoporous zirconia, and characterization of the mesoporous zirconia by TGA, XRD, TEM, and SANS.

## Abstract

Mesoporous zirconia has attracted great attention from the research community due to its unique properties such as high surface area, uniform pore size distribution, and large pore volume. Self-assembled structures have been used as directing agents to synthesize mesoporous zirconia. Here, we investigate the use of self-assembling block copolymers conjugated to cationic biomolecules such as lysozyme, as well as self-assembling cationic block copolymers as templates for synthesis of mesoporous zirconia in completely aqueous media. We believe this is the first report of a synthesis of mesoporous zirconia in completely aqueous media with biomolecules, thereby opening up opportunities for different mechanisms for controlling zirconia synthesis. The inorganic content of the nanocomposite was determined by TGA, while the structure and composition of the samples was characterized by XRD, nitrogen adsorption, TEM, SEM, SANS, and solid state NMR. The results showed that zirconia nanocrystals formed after calcination of the as-synthesized nanocomposite at 500 ˚C, and significant crystal growth was observed only after 900 ˚C calcination. The conjugate-templated zirconia showed a surface area

of 174 m2/g after calcination at 500 ℃, and retained its tetragonal structure even after calcining at 900 ˚C. The cationic pentablock copolymer-templated zirconia showed the highest surface area, 191 m2/g, after calcination at 500 ℃, and also demonstrated improved thermal stability. This bioinspired method can be easily scaled up and potentially used for synthesis of other oxides.

Key words: Mesoporous zirconia, bioinspired synthesis, templating, aqueous media

## 4.1 Introduction

In recent years, zirconia has received much attention from the materials research community due to its attractive intrinsic properties such as hardness, shock wear, excellent acid and alkali resistance, low frictional resistance, and high melting temperature.[1] It has been widely used in applications, such as gas sensors, solid oxide fuel cells (SOFCs), catalysis, catalysis carriers, and orthopaedic implants.[1–4] However, bulk zirconia synthesized by the conventional methods usually have relatively low specific surface area (<100 $m^2$ $g^{-1}$) and microporosity, which limit some of its applications.[4] Much research has been focused on increasing the specific surface area of zirconia. Synthesis of mesoporous zirconia has received significant attention, due to its high surface area, uniform pore size distribution, and large pore volume.[5]

A number of synthesis methods such as sol–gel synthesis, aqueous precipitation, thermal decomposition, and hydrothermal synthesis have been reported.[1] However, some of these methods require extremes of temperature or pressure, or are costly. A large number of researchers have focused on the preparation of porous zirconia with high specific surface area by using self-assembled structures as directing agents. The unique of the synthesis of mesoporous materials is its focus on the use of supramolecular assembly of template molecules as structure-directing agents. Self-assembly of block copolymers, surfactants, colloidal suspensions and proteins, which create nanostructures through versatile approaches, plays a key role in directing the formation of

organized porous structures.[5–7]

Block copolymers, especially amphiphilic block copolymers, have been increasingly used to organize mesostructured composites. For example, Pluronic block copolymers have been used as structure-directing agents for organizing different inorganic material networks.[5,8–10] Yang *et al.* synthesized large-pore mesoporous metal oxides, with semicrystalline frameworks using Pluronic P-123 as template in organic solvents.

Previous research on templated zirconia synthesis was almost exclusively carried out in organic solvents.[4–6,8,11–14] This is probably the reason that there are hardly any bioinspired methods for the synthesis of zirconia, although such approaches provide environmentally clean and energy-conserving processes, and have been widely used to synthesize other oxides such as silica.[15] A few studies have recently reported biosynthesis of zirconia, but these methods suffer from several limitations.[1,16] Bansal *et al.* synthesized zirconia nanoparticles using the fungus *Fusarium oxysporum,* and pointed out that a cationic protein in the fungus may play an important role in the biosynthesis.[1] Although zirconia was successfully synthesized under mild conditions, this study was limited by the availability of the fungus, the difficulties in identification and separation of the protein, and the very low yield of zirconia. Jiang *et al.* reported zirconia synthesis catalyzed and templated by lysozyme.[16] This protein (MW 14.7 kDa, 147 amino acid residues, pI=10.5) is one of the most prominent members in the class of cationic enzymes, which can hydrolyze the glycosyl groups. Recent reports indicate the involvement of lysozyme in the biomineralization of silica, titania, and calcium carbonate, and heat-denatured lysozyme has also been implicated in the synthesis of bismuth sulfide, although the mechanism is unclear.[17] However, the zirconia yield was very limited due to the low solubility of the precursor ($K_2ZrF_6$).[16] In addition, the fluoride precursor is neither environmentally safe, nor inexpensive for large scale zirconia production. Moreover, neither of these were mesoporous zirconia.

Previously we have used bioinspired approaches involving Pluronic polymers conjugated to mineralization peptides to template calcium phosphate nanocomposites.[18] Using a similar approach in this study, we have used Pluronic triblock as well as cationic pentablock copolymer templates conjugated with lysozyme as the mineralization protein to synthesize mesoporous zirconia with high surface area in completely aqueous media. Aqueous solutions of Pluronic F127 (PF127) and the cationic pentablock copolymers (poly(diethylaminoethylmethacrylate) (PDEAEM) blocks attached to PF127) self-assemble into spherical micelles at low temperature and concentration, and transform to viscous gels with increasing temperature (typically above 25 ˚C) or concentration.[10] Since cationic groups have shown to be important for zirconia synthesis in aqueous solutions, the PDEAEM is responsive to pH changes and provides tertiary amine groups. In addition, at specific temperature and pH ranges (T>50 ˚C and pH of 8-11), PDEAEM-based pentablock copolymers can form cylindrical micelles in aqueous solutions.[19,20] These various self-assembled polymer micelle structures were used as templates for the mesoporous zirconia formation. The synthesized zirconia was characterized and found to exhibit high specific surface area, porosity and thermal stability even at high temperatures. This is the first time that mesoporous zirconia was reported to be synthesized in completely aqueous media, with a potential to be scaled up relatively easily.

## 4.2 Experimental Section

### 4.2.1 Chemicals and Materials

Triblock copolymer poly(ethylene oxide)-b-poly(propylene oxide)-b-poly(ethylene oxide ) Pluronic F127 (PF127) ($PEO_{100}PPO_{65}EO_{100}$, Mav = 12600 g $mol^{-1}$), lysozyme from chicken egg white, zirconium(IV) oxynitrate hydrate ($ZrO(NO_3)_2$) (99.99%), *N*,*N* –(diethyl amino)ethyl methacrylate (DEAEM), succinic anhydride, and N-hydroxy succinimide(NHS) were all purchased from Sigma-Aldrich. Ammonium hydroxide was purchased from Fisher scientific. All

of the chemicals were used as received without further purification. A bicinchoninic acid (BCA) protein assay kit and dialysis cassettes were purchased from Thermo Scientific. Sodium dodecyl sulfate polyacrylamide gel electrophoresis (SDS-PAGE) kit was purchased from Bio-Rad.

### 4.2.2 Synthesis of Pluronic-lysozyme conjugate, and pentablock copolymers

The Pluronic was conjugated to the lysozyme using an NHS-based coupling method.[18] The hydroxyl end groups of PF127 Pluronic were converted to carboxyl groups by reacting it with succinic anhydride in pyridine. The carboxyl-terminated PF127 was activated by reaction with NHS at room temperature for 24 h. The NHS-activated PF127 was then covalently bonded (conjugated) with lysozyme. After reacting at room temperature for 24 h in PBS buffer, the mixture was dialyzed against water, using a cellulose ester membrane with a molecular weight cut off of 25,000 (Thermo Scientific), for 4 days at room temperature to remove the unreacted polymer and lysozyme. The mixture was then freeze dried to form the solid conjugate.

The cationic pentablock copolymer (PDEAEM-based) exhibits reversible pH and thermo-responsive behavior, and was synthesized by atom transfer radical polymerization (ATRP). Poly(diethyl amino ethyl methacrylate) (PDEAEM) blocks were grown to the ends of PF127 by ATRP as described earlier.[21]

Scheme 1. Structure of the cationic pentablock copolymer (PDEAEM-based pentablock)

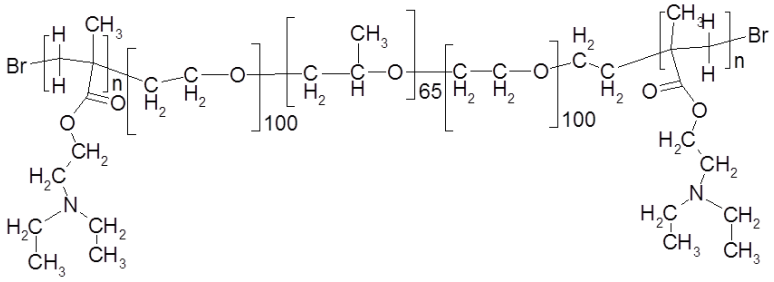

### 4.2.3 Characterization of the conjugate

The synthesized conjugate was characterized by fast protein liquid chromatography (FPLC) and SDS-PAGE to confirm covalent binding between the PF127 and lysozyme, and to estimate the molecular weight. A BCA assay was used to determine the percentage of lysozyme in the conjugate. Dynamic light scattering (DLS) was used to observe the micelle sizes of the conjugates formed in aqueous media.

**FPLC.** The size-exclusion chromatography studies were carried out using an AKTA FPLC system (GE healthcare) through a prepacked Superdex 75 column. The flow rate was 0.4 mL/min. The sample was the solution right after the conjugation reaction of Pluronic-NHS and lysozyme. The intensity was measured based on the absorbance of UV light (A280) by the aromatic amino acids. The fractions of the FPLC were collected at 0.5 mL each, and selected to run SDS-PAGE to estimate the molecular weight of the fractions.

**DLS.** The diameter of the micelles formed by the PF127 and PF127-lysozyme conjugate in water was determined using quasi-elastic light scattering (Zetasizer Nano, Malvern Instruments Ltd.) with laser irradiation at 633 nm.

### 4.2.4 Synthesis of the zirconia nanocomposite and mesoporous zirconia

Since a sol-gel process was important for the polymer to template the zirconia formation, the amount of polymer template in each sample was chosen at a percentage that allows the polymer and precursor mixture to form a viscous solution at 4 $^{\circ}$C and self-assemble to form a physical gel at room temperature. The conjugate amount was limited by its solubility in water; therefore, additional PF127 was added to help gel formation during the aging process.

In a typical synthesis, the zirconia precursor solution was prepared by dissolving 1.15 g $ZrO(NO_3)_2$ into 10 mL water. To this solution, 3.0 g PF127, 2.6 g PF127 and 0.4 g conjugate, or 2

g PDEAEM was added and dissolved at 4 ˚C. The solution was then brought up to room temperature, which resulted in formation of a gel within 30 minutes. After the gel formation, ammonium hydroxide (28-30%) was added with stirring until the pH was equal to 10. A few samples were prepared at pH=4. A white precipitate was formed within the gel when ammonium hydroxide was added. The precipitated gel was aged at room temperature or 60 ˚C for 3 days before washing three times with water to remove the ammonium nitrate, excess ammonium hydroxide, and free polymer. The sample was then frozen in liquid nitrogen and lyophilized for two days to obtain polymer/zirconia nanocomposite powder. The composite was heated to 500 ˚C or 900 ˚C for 3 hours in air to pyrolyze the polymer template and form mesoporous zirconia for further characterization. Six representative samples are selected for detailed characterization as shown in Table 4.1:

Table 4.1 List of samples with their different polymer templates and aging conditions

| Template | No template | PF127 | PF127+ Conjugate | Pentablock | Pentablock | Pentablock |
|---|---|---|---|---|---|---|
| Aging Temp. | 20 ˚C | 20 ˚C | 20 ˚C | 20 ˚C | 60 ˚C | 20 ˚C |
| pH | 10 | 10 | 10 | 10 | 10 | 4 |

### 4.2.5 Characterization of the zirconia nanocomposite and mesoporous zirconia

Polymer/zirconia nanocomposite and mesoporous zirconia samples were characterized by thermogravimetric analysis (TGA), X-ray diffraction (XRD), nitrogen sorption, transmission electron microscopy (TEM), scanning electron microscopy (SEM), small angle neutron scattering (SANS), and solid state nuclear magnetic resonance (NMR) techniques.

**TGA.** The percentage of inorganic material in the nanocomposite was determined by TGA, which was performed on TGA 7 equipment (Perkin Elmer). Approximately 10 mg of the freeze

dried nanocomposite sample was placed in a platinum pan, and was heated from room temperature to higher temperature at a rate of 10 ˚C/min under 20 mL/min air flow. Isothermal heating at 500 ˚C for 3 hours was applied to some samples.

**XRD.** The crystal structure of the calcined zirconia was studied by an X-ray diffractometer (X'Pert PRO, PANalytical Inc.). The diffractometer was operated at 45 kV and 40 mA. The monochromatic light was from CuKα radiation with a wavelength of 0.15418 nm. The scan rate was 0.021˚/s with a step size of 0.017˚, over the range of $20° \leq 2\theta \leq 80°$. X'pert Data collector software was used to collect the data.

**Nitrogen sorption.** Nitrogen adsorption and desorption runs were carried out using an AUTOSORB-1 QUANTA CHROME Instrument (Quantachrome Corporation). The adsorption and desorption isotherms of the 500 ˚C calcined zirconia were obtained at 77 K. All samples were degassed under vacuum at 110 ˚C prior to adsorption. Surface area was calculated by applying the Brunauer-Emmett-Teller (BET) method and using the data in the $0.03 < P/P_0 < 0.3$ range. The pore size distribution was calculated using the Barrett-Joyner-Halenda (BJH) method and the desorption branch of the isotherm plot. The total pore volume was calculated based on the volume of nitrogen adsorbed near saturation pressure.

**TEM.** Imaging of the samples was performed using a Tecnai G2 F20 Scanning Transmission Electron Microscope (STEM) (FEI Company, Hillsboro, OR) equipped with High Angle Annular Dark Field (HAADF) and Energy Dispersive X-ray Spectroscopy (EDS) detectors at an operating voltage of 200 kV. 20 µL of diluted zirconia powder suspension was deposited on a holey carbon-supported copper grid. Multiple areas of each sample were examined.

**SEM.** Morphological features of the synthesized mesoporous zirconia were studied by FEI quanta 250 SEM (FEI Company, Hillsboro, OR). 20 µg of zirconia powder sample was dispersed

on a carbon stub, and was sputter-coated with iridium for imaging. Multiple areas of each sample were examined.

**SANS.** This technique was used to highlight the structure of the block copolymer in the nanocomposite gels. In a deuterated solvent, the polymer phase has higher neutron-scattering contrast than the inorganic phase. A specific batch of samples using $D_2O$ as solvent was prepared for the characterization. The SANS measurements were performed on the Low-Q Diffractometer (LQD) of the Lujan Center at Los Alamos National Laboratory (LANL). The nanocomposite samples during the aging stage were sealed in quartz benjo cells with a 2-mm path length. The scattering vector, q, was varied between 0.003 $Å^{-1} < q < 0.3$ $Å^{-1}$, where $q = (4\pi/\lambda) \sin(\theta/2)$ with the neutron wavelength $\lambda$ and the scattering angle $\theta$. The scattered intensity I(q) was placed on an absolute scale in the units of $cm^{-1}$. SANS data were reduced by software provided at the Lujan center and corrected for empty-cell and background scattering.

**NMR.** Solid-state NMR spectra were obtained using a Bruker Biospin DSX-400 spectrometer (Bruker-Biospin, Billerica) at 400 MHz for $^{1}H$ and 100 MHz for $^{13}C$. A Bruker 7-mm double-resonance magic-angle-spinning (MAS) probe-head was used with a spinning frequency of 7 kHz. The $90^{\circ}$ pulse length was 4.5 μs for $^{1}H$ and 4 μs for $^{13}C$. A 150-s recycle delay was used in direct-polarization $^{13}C$ NMR experiments, with two-pulse phase-modulation (TPPM) heteronuclear decoupling during detection.

## 4.3 Results and Discussion

### 4.3.1 Characterization of the Pluronic-lysozyme conjugate

The covalent attachment between PF127 and lysozyme was confirmed by FPLC and SDS-PAGE, shown in the supporting information. The conjugate had a molecular weight of about 30 kDa. Some larger molecular weight fractions were also detected, which may be due to the non-

specific binding between the NHS-modified PF127 and the free amine groups in lysozyme. The BCA assay indicated that lysozyme constitutes 38 wt.% of the conjugate.

Figure 4.1 shows the diameter of the lysozyme molecules and of the micelles formed by PF127 and conjugate as determined by DLS. The conjugate micelles were larger than the PF127 micelles, and the increase was probably due to the lysozyme end groups on the conjugate. A small fraction of larger micelles (around 13 nm) observed for the conjugate is attributable to and consistent with the formation of the larger molecular weight conjugates mentioned above.

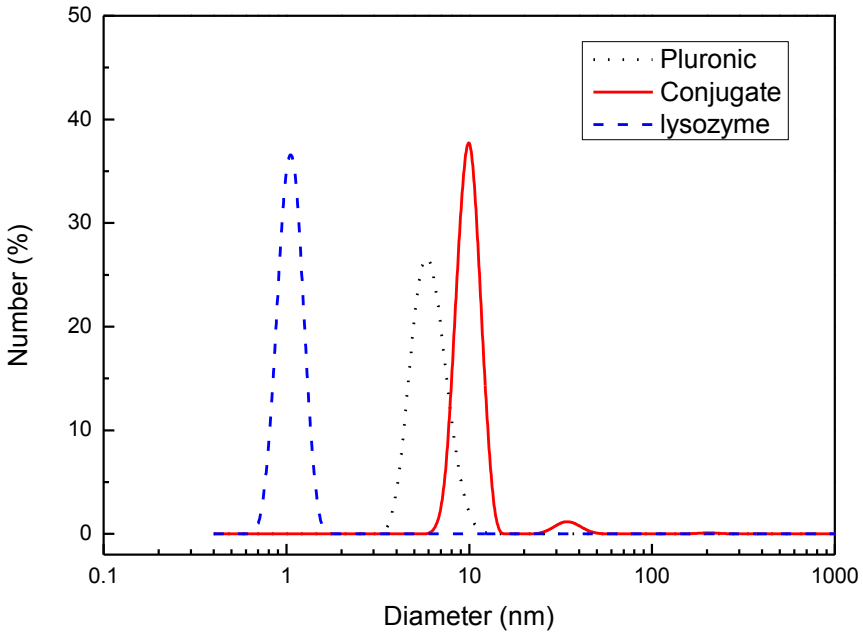


Figure 4.1 DLS of lysozyme, conjugate and PF127 in water, molecule or micelle size distribution by number

### 4.3.2 Characterization of zirconia nanocomposite and mesoporous zirconia

**TGA.** A thermogravimetric analyzer was used to determine the decomposition temperature of the polymeric templates and the fraction of the inorganic phase in the composite. Figure 4.2 shows the TGA results obtained by heating the pure polymer templates. PF127 was totally burned off by 400 ˚C. Lysozyme was burned off once the temperature reached 700 ˚C. To mimic the annealing conditions, pure pentablock, lysozyme and the conjugate were heated to 500˚C and maintained at 500 ˚C for 3 hours. After a 3-hour isothermal hold at 500 ˚C, almost all the organics were gone. Therefore, only inorganic zirconia was left after the freeze-dried nanocomposite had been calcined at 500 ˚C for 3 hours.

The inorganic content of each zirconia nanocomposite sample can be estimated from Figure 4.3. The sample prepared under identical conditions except without any organic template resulted in 77 % zirconia, and the 23 % weight loss corresponds to almost exactly the dehydroxylation of the $Zr(OH)_4$ precipitate according to:

$$Zr(OH)_4 \rightarrow ZrO_2 + 2H_2O$$

More organics remained in the conjugate templated sample than in the PF127-templated one (i.e. the zirconia content was lower in the conjugate than in PF127), indicating that the lysozyme helped enhance the interactions between the template and the precursor, which was also confirmed by solid state NMR as discussed later. Although the mechanism is still unknown, the cationic property of lysozyme may play an important role.[1,16] The fact that the cationic pentablock templated samples had an even higher fraction of polymer, about 55% to 65%, indicate its more extensive interactions with the zirconia precursor.

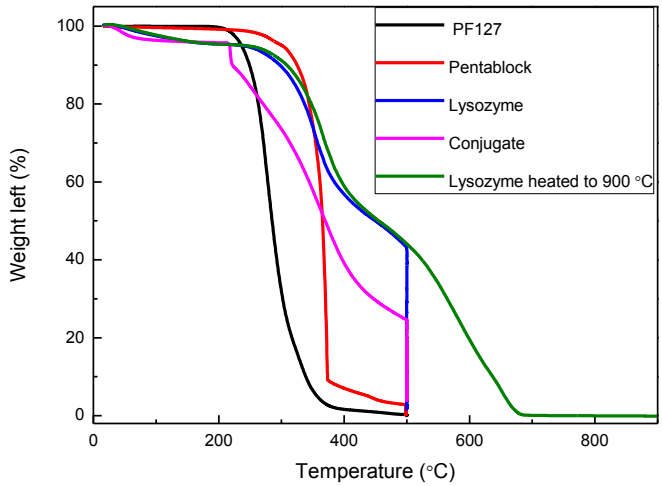


Figure 4.2 TGA of organic templates: PF127 and lysozyme were heated to 500 ℃ and 900 ℃, respectively, with a ramp of 10 ℃/min; pentablock, lysozyme and conjugate were heated to 500 ℃ with a ramp of 10 ℃/min, and then kept at 500 ℃ for an isothermal step for 3 hours.

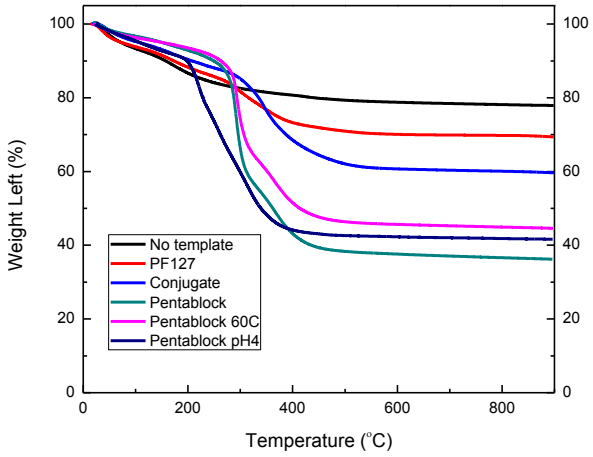


Figure 4.3 TGA for freeze dried zirconia nanocomposites with different templates shown in the legend. The aging conditions were 20˚C and pH 10, if not specified in the legend, and are the same for all the following figures. All the samples were heated directly to 900 ˚C at a rate of 10 ℃/min.

**$^{13}$C NMR of the organic components in the composites.** Figure 4.4 shows $^{13}$C NMR spectra of the organic templates and the organic-inorganic composites. The spectra were obtained by direct polarization after long (150-s) recycle delays for full relaxation, which avoids the selective signal enhancement seen in standard cross polarization from $^{1}$H.

The spectra of lysozyme and PF127 are clearly distinct, with characteristic C=O and N-CH peaks of lysozyme near 173 and 55 ppm, and OCH signals of PF127 between 70 and 75 ppm. This enables peak assignment in the spectra of materials containing both components. In PF127, the signal of crystalline PEO at 70 ppm is almost invisible, most likely due to line broadening by helical jumps that interfere with H-C dipolar decoupling. The signal of the $CH_3$ groups in the PPO block near 17 ppm is observed at the expected intensity level. The spectrum of the conjugate template, see Fig. 4.4(c), is dominated by the signals of PF127, since the lysozyme signals, e.g. near 173 and 55 ppm, are broad and low.

Figure 4.4(d) shows the spectrum of the composites with PF127 template. The signal intensity is ca. 20 times smaller than in neat PF127, indicating that only a relatively small fraction of the polymer is strongly bound to zirconia. In addition to the regular PF127 signals, the spectrum shows unexpected peaks at 180 ppm and 23 ppm, which are also observed in the spectra of the other mineralized samples. The chemical shifts are consistent with acetyl groups, -OOC-$CH_3$, but their origin remains unclear.

Figures 4.4(e) and (f) compare the spectra of the composites templated by lysozyme-PF127 conjugate and by lysozyme and PF127 physical mixture. In these spectra, the signals of lysozyme are clearly visible and their area exceeds that of the PF127 peaks by an order of magnitude. In other words, the PF127:lysozyme ratio is reduced by a factor of 10 to 20 relative to the neat template in Figure 4.4(c). This demonstrates selective retention of lysozyme, which can be attributed to its stronger binding to zirconia. The spectrum from the conjugate exhibits a

significantly larger total area than that of the physical mixture, which indicates stronger binding of the conjugate template to zirconia.

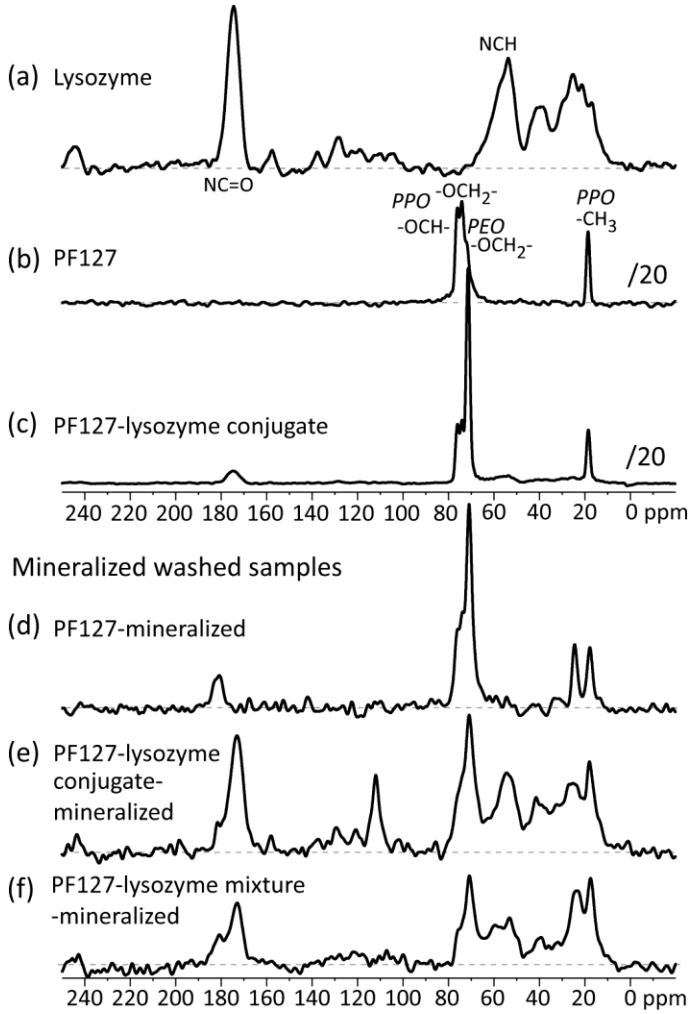


Figure 4.4 Direct-polarization 13C NMR spectra of the organic templates: (a) pure lysozyme; (b) pure PF127 triblock copolymer; (c) pure PF127-lysozyme conjugate template; and 13C NMR spectra of the freeze dried organic-inorganic composites with different organic templates: (d) PF127 template; (e) PF127-lysozyme conjugate template. The signal at 111 ppm is background from Teflon tape used to balance the magic-angle-spinning rotor. (f) Mineralized physically mixed PF127 and lysozyme. All spectra were scaled to account for differences in sample mass. Recycle delay: 150 s; magic-angle-spinning frequency: 7 kHz.

**XRD.** The XRD patterns shown in Figure 4.5 clearly indicate that the amorphous zirconia precursors were completely crystallized to tetragonal zirconia after calcination at 500 ˚C.[2] The broad peaks indicate that the size of the crystals was in nanometer range and the calculated crystal sizes according to the Debye-Scherrer formula (using the peak at $2\theta = 30^{\circ}$) are listed in Table 4.2. They are consistent with the TEM data shown in the following. The zirconia synthesized without any templates showed sharper and stronger peaks than any other samples, which demonstrated it had the largest crystal size. As shown in TEM micrographs and Table 4.2, polymer templation results in smaller crystallites and higher specific surface as will be discussed below. The benchmark sample prepared without polymer template shows a small peak at $2\theta = 28^{\circ}$ indicative of monoclinic phase. Apparently, polymer templates prevent formation of monoclinic phase at this temperature either by forming smaller crystals or directing organization of the precursors.

The zirconia templated by pentablock copolymers and aged at 60 ˚C had broader peaks than the other samples. This implied that it had the smallest crystal size and may have the largest surface area among the samples, which was confirmed by the TEM and BET surfaces area measurements, and could be attributed to the reversible thermal and pH responsive properties of cationic pentablocks. The pentablock solution exhibits micellar and gel phases in response to changes in both the temperature and pH by virtue of the lower critical solution temperature of the PPO and PDEAEM blocks and the polyelectrolyte character of the pendant PDEAEM blocks.[22] PDEAEM has a pKa of 7.6, and at pH<pKa, the micelles are charged, and cannot be well packed due to electrostatic repulsion; at 8.1<pH<11, the micelles are deprotonated. At higher pH values (typically 8.1-11) and temperature (typically 37-75 ˚C) the progressive dehydration of the PPO blocks causes the formation of cylindrical micelles. Therefore, the tight packing of the pentablock template micelles in the zirconia composite and aging at 60 ˚C, may be the reason for better templating and the resulting smaller crystal sizes.

The XRD patterns of 900 °C calcined zirconia are shown in Figure 4.6. Clearly, all the peaks sharpen with increasing temperature, indicating the growth of the zirconia crystal size as temperature increases. The zirconia synthesized without template, the zirconia templated by pentablocks and aged at a pH of 4, and templated by PF127 exhibit strong peaks associated with the monoclinic phase, whereas the other samples were still dominated by the tetragonal phase. Especially in the zirconia templated by the conjugate, only a small peak was detected at 28 °, indicating that only a small fraction of the sample was converted to the monoclinic structure at this temperature. Retention of tetragonal phase may be due to the higher decomposition temperature of lysozyme, which lets the conjugate template stay longer in the composite during the calcination, and inhibited pore collapse to form larger crystals and transition to monoclinic zirconia. And the smaller initial crystallite size also resulted in retardation of crystal growth during heat treatment, and hence delayed transformation to the monoclinic phase. Zirconia formed at lower pH had a lower surface area and a lower thermal stability, and formed the monoclinic phase more easily than the one at higher pH.[23] In summary, we conclude that the conjugate and pentablock copolymer templates were more effective at maintaining the tetragonal zirconia phase and forming smaller zirconia particles.

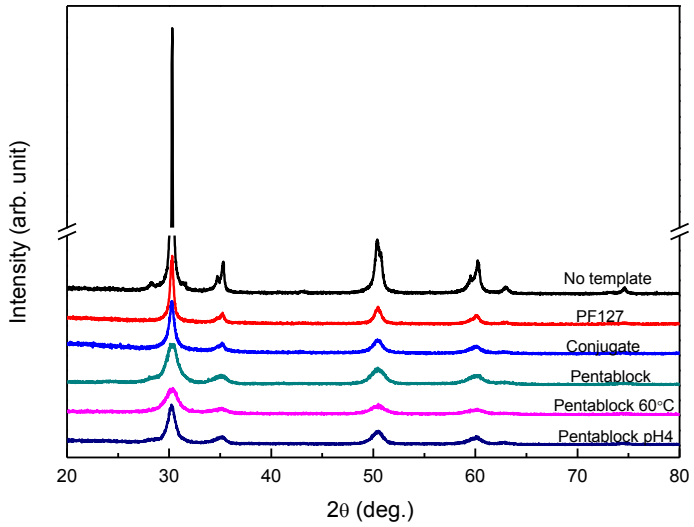


Figure 4.5 XRD of the 500 ˚C calcined zirconia. The legend stands for the polymer template for each sample.

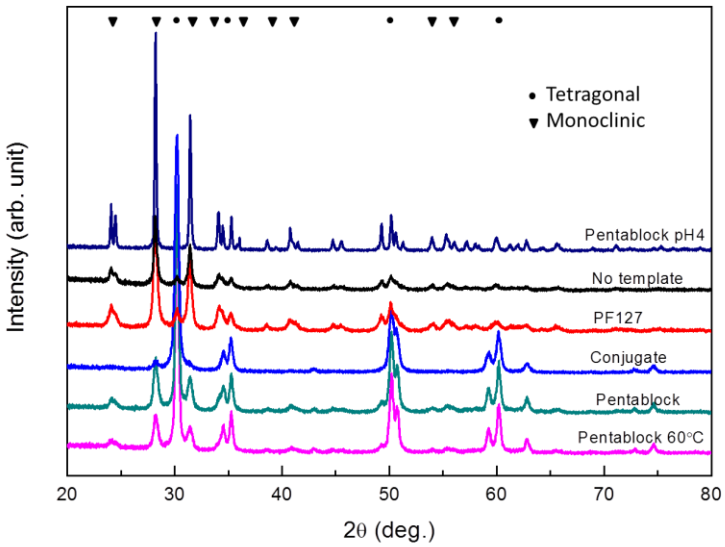


Figure 4.6 XRD of the 900 ˚C calcined zirconia. The legend identifies the polymer template for each sample

**Specific surface area of the mesoporous zirconia.** Figure 4.7 shows a typical isotherm plot for the 500 ˚C calcined zirconia sample, and the existence of a hysteresis loop indicates the mesoporous structure of the 500 ˚C calcined self-assembled zirconia.[5] Table 4.2 compiles the specific surface area, average pore size, and total pore volume for the six as-prepared zirconia samples. Both the pentablock copolymer and the conjugate templated zirconia samples had higher surface areas than the PF127 templated zirconia sample and the no-template zirconia sample. Templating by the pentablock at 60 ˚C further increased the surface area of the self-assembled zirconia samples compared to templating by the conjugate under the same conditions. The specific surface area was also related to the pore size and total pore volume. In this specific study, the surface area is larger when the pore size is smaller and the total pore volume is larger. As shown in Table 4.2, the conjugate-templated zirconia had a significantly smaller average pore size; the pentablock-60˚C templated zirconia had the largest total pore volume and relatively small average pore size, so these two samples had relatively higher surface areas compared to the other zirconia samples.

At pH4, the pentablock micelles could not pack to form micellar aggregates, while the other two pentablock templated zirconia samples could form close packed templates that performed better with respect to increasing the template sample's surface area.[24]

The typical pore size distribution of the 500 ˚C calcined self-assembled zirconia samples were studied by applying the Barrett-Joyner-Halenda (BJH) method to the $N_2$ desorption branch of the sample isotherm plots, as shown in Figures 4.8. In Figure 4.8, all pores fell into a range of 30Å~500Å (mesoporous). The conjugate templated zirconia sample exhibited a close to unimodal pore size distribution, with a nearly uniform pore size of about 3.6~3.7 nm. The no-template zirconia sample had a close to bimodal pore size distribution; the majority of pore sizes in this sample are either 3.5~3.7 nm or 45 nm. The pentablock-20˚C-pH4 templated sample exhibited a

secondary peak following the main peak, so the majority of pore sizes in this sample were between 3.8 nm and 5.1 nm. These mesopores can form either from removal of the polymer templates or dehydroxylation and crystallization of amorphous zirconia, and all contribute to the increase of the specific surface area of the mesoporous zirconia samples.

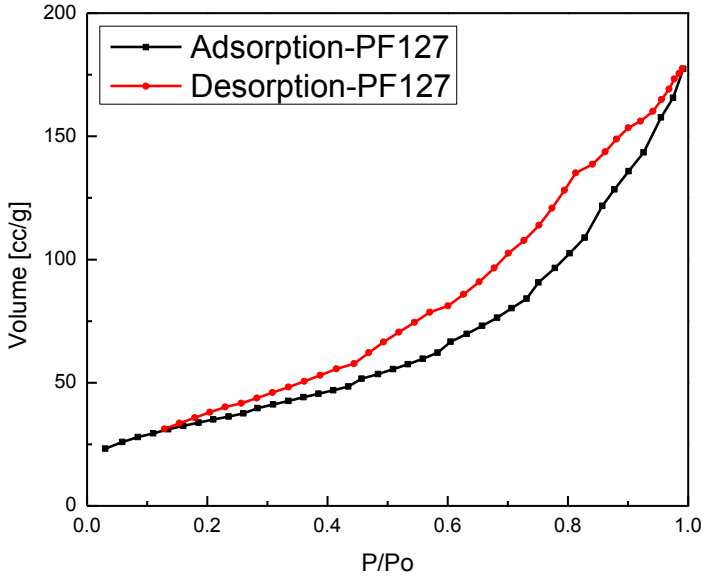


Figure 4.7 N2-adsorption-desorption Isotherm plots for 500 ℃ calcined self-assembled mesoporous zirconia

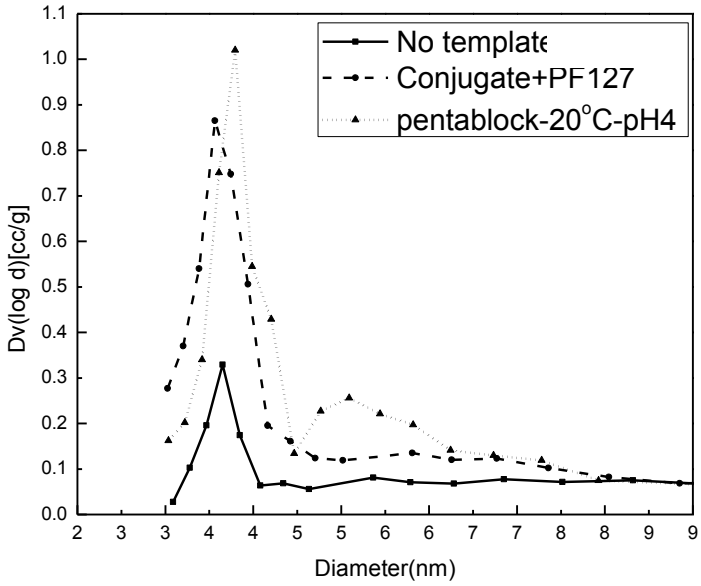


Figure 4.8 Pore size distributions for 500 ˚C calcined self-assembled mesoporous zirconia samples

Table 4.2 Surface area, average pore size, pore volume and estimated crystal size from the XRD results for the 500 ℃ calcined zirconia samples

| | Surface area ($m^2/g$) | Avg. pore size (nm) | Pore Volume ($cm^3/g$) | Estimated crystal diameter from X-ray diffraction (nm) |
|---|---|---|---|---|
| No template | 52 | 10.0 | 0.13 | 26.0 |
| PF127 | 126 | 8.7 | 0.27 | 22.4 |
| Conjugate+PF127 | 174 | 4.5 | 0.20 | 11.7 |
| Pentablock-60 ˚C | 191 | 6.8 | 0.33 | 6.3 |
| Pentablock-20 ˚C | 140 | 8.2 | 0.29 | 6.8 |
| Pentablock-20 ˚C-pH4 | 98 | 5.8 | 0.14 | 9.3 |

**Morphology of the mesoporous zirconia.** The morphology of the mesoporous zirconia can be viewed by TEM and SEM techniques. Figure 4.9 shows TEM images of the zirconia formed after 500 ˚C calcination. Estimated from the images, every sample had pores in the 5-10 nm range, which was consistent with the BJH results. The zirconia formed without template, shown in Figure 4.9-a, had much larger crystal sizes than the other samples. Also, it was a mixture of tetragonal and monoclinic phases, as shown in the inset (Figure 4.9-a), while all the other polymer templated samples showed mostly the tetragonal phase.[25,26] This is consistent with the XRD results. The conjugate template resulted in smaller crystal sizes than the PF127 template, which may be due to the higher decomposition temperature of the lysozyme in the conjugate, as mentioned above.

The pentablock templated samples (Figure 4.9-d, -e, and -f) had similar morphology. These samples exhibited more uniform structures than other samples. The slight difference among the three samples may be attributed to the different aging temperature and/or pH, since the pentablock template could respond to both temperature and pH changes. In a certain range, at higher temperatures and pH, cylindrical micelles could form. The zirconia templated by pentablock and aged at 60 ˚C (Figure 4.9-e) showed the smallest crystal size, about 5-10 nm, while the samples synthesized at the same pH but at lower aging temperature shows (Figure 4.9-d) slightly larger particle size, about 10 nm; Figure 4.9-f shows the sample templated with pentablock aged at room temperature and at pH=4, where the polymer could not pack as effectively because the cationic groups were charged. These observations matched the BET surface area data and the crystal sizes in Table 4.2.

HAADF-STEM is sensitive to scattered electrons generated in proportion to the atomic number (Z) of the atoms in the specimen. It can be used for obtaining compositional and morphological information of a sample, with contrast varying roughly as a function of Z. An

STEM image of the 500 °C calcined zirconia samples is shown in Figure 4.9-g. Here the bright areas correspond to the zirconium-rich areas of the mesoporous zirconia. We can see the porous structure clearly in this image. Figure 4.9-e was taken at the edge area of Figure 4.9-g.

Figure 4.10 shows TEM images of some of the zirconia composite samples heated to 900 °C. Clearly the zirconia crystals were larger than after 500 °C calcination. The diffraction patterns of the zirconia showed that only the conjugate templated zirconia retained the tetragonal phase,[25,26] which is consistent with the XRD data for the same heat treatment temperature as discussed above (Figure 4.6). The pattern inside the crystal seen in Figure 4.10-a was formed due to the volume change associated with the phase transformation. A high resolution TEM image of this sample is shown in the supporting information. By contrast, the zirconia templated by conjugate in Figure 4.10-c exhibits no such pattern, as it has not gone through the tetragonal to monoclinic phase transformation.

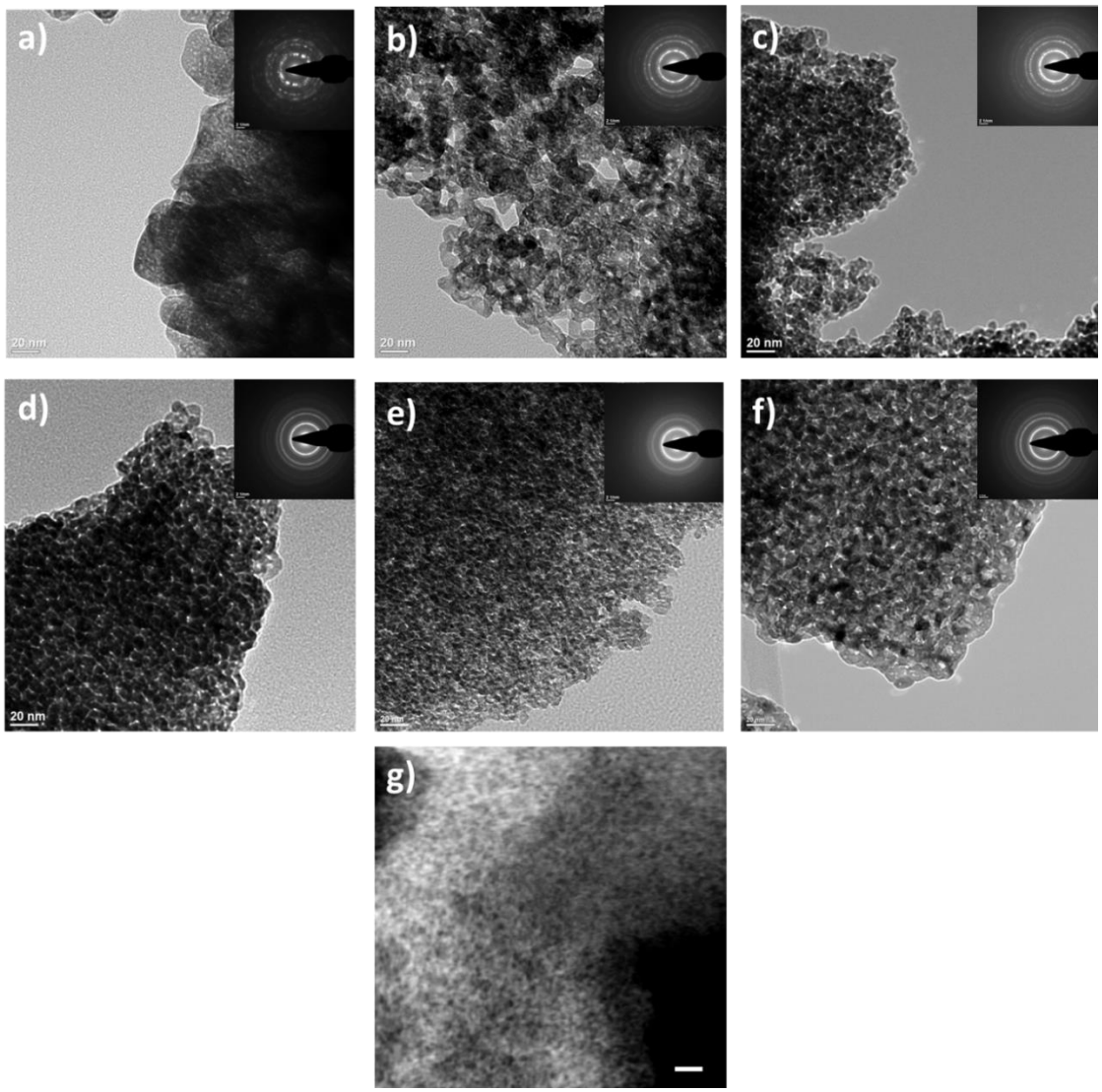


Figure 4.9 TEM images and diffraction patterns of the 500 °C calcined zirconia templated by: a) no template; b) PF127; c) conjugate; d) pentablock; e) pentablock, aged at 60 °C; f) pentablock template, pH=4. The scale bars in image a) through f) are 20 nm. g) Dark field image of the zirconia templated by pentablock, aged at 60 °C; the scale bar is 50 nm.

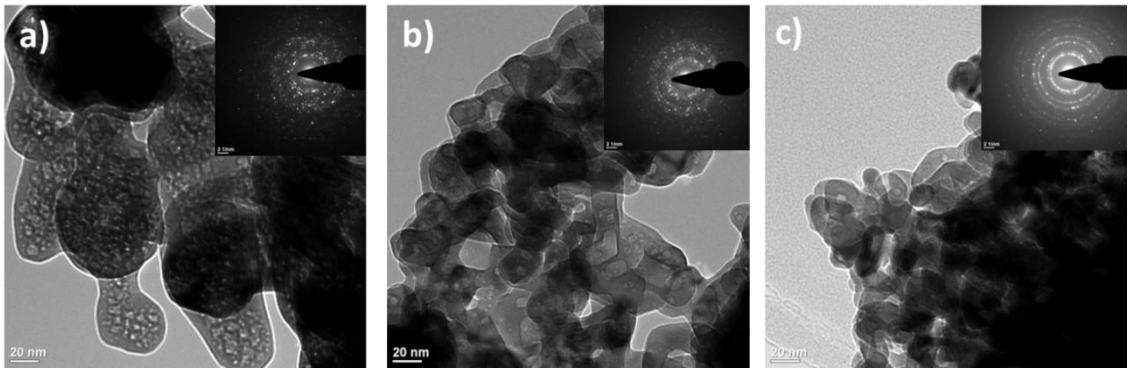


Figure 4.10 TEM images and diffraction patterns of the 900 ˚C calcined zirconia templated by: a) no template; b) PF127; c) conjugate.

Although SEM does not have the high resolution as TEM, it can be used to observe the packing of the zirconia particles and the surface morphology. Figure 4.11 shows the SEM images of the zirconia calcined at 500 ˚C. We can see in the micrograph of Figure 4.11-f that the zirconia formed at pH=4 has a very different morphology, compared with the other zirconia samples, apparently due to aging the nanocomposite at low pH as discussed above.[23] TEM images (Figure 4.9-f) also show similar features. The zirconia synthesized without template and with the PF127 template had loose packing compared to the other samples, and these two samples also had lower surface area, indicating that the smaller sized particles and their tight packing may introduce large surface area in this study.

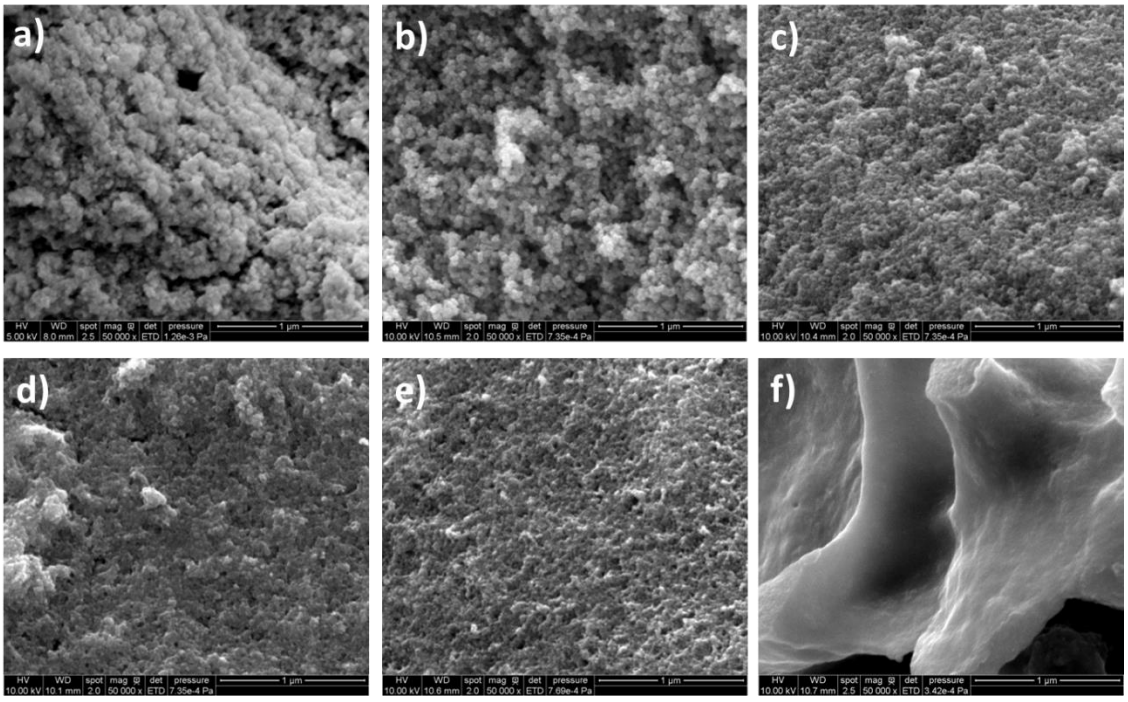


Figure 4.11 SEM images of the 500 ˚C calcined zirconia templated by: a) no template; b) PF127; c) conjugate; d) pentablock; e) pentablock, aged at 60 ˚C; f) pentablock template, pH=4.

**SANS shows polymer templating.** Small angle neutron scattering techniques are versatile in elucidating detailed information about the phase behavior, organization in ordered arrays, and the morphological transitions of the self-assembled micelles and gels. Figure 4.12 shows the SANS results of the composite gel during the aging process. The samples with PF127 and conjugate templates showed scattering peaks from PF127 micelles,[27] and samples with pentablock templates exhibited peaks from the pentablock copolymer.[22] The composite with PF127 template shows diffraction peaks with $Q/Q^*$ ($Q^*$ is the first order peak position) of $\sqrt{3}:\sqrt{4}:\sqrt{8}$ , indicating a FCC structure;[28,29] while the composite with pentablock copolymer template shows diffraction peaks with $Q/Q^x$ of $1:\sqrt{3}$, indicating a hexagonal closed packing.[19] Although we did not fit the data to a model in this study, literature reports on modeling of these two polymers are abundant.[22,27] The

data implied that the zirconia composite formed in a manner that did not interrupt the organization of the template micelles.

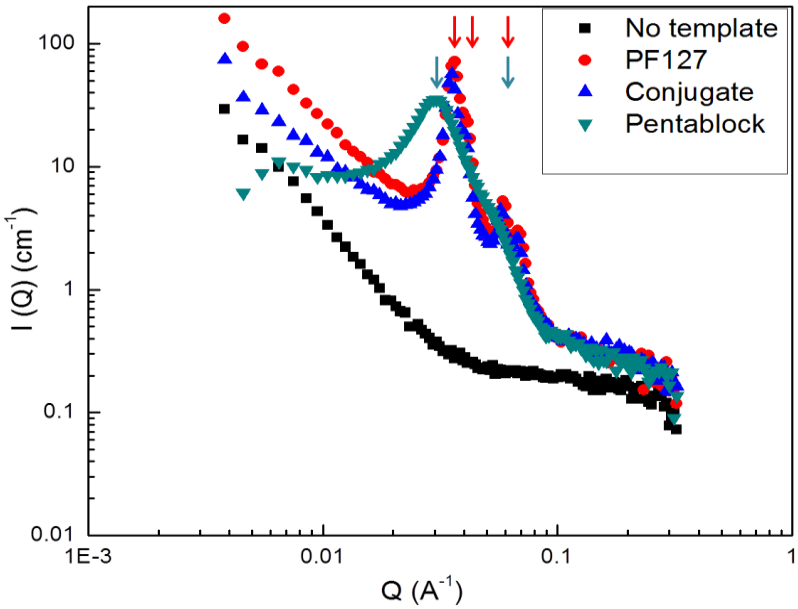


Figure 4.12 SANS results of the composite gel after aging. The legend indicates the polymer template in each sample. Red arrows show the peak positions of PF127 templated composite, and green arrows show the peak positions of Pentablock templated composite.

### 4.3.3 Proposed templation mechanism.

We controlled the property of pentablock templated zirconia by adjusting the pH and the aging temperature. In Figure 4.13, we propose a plausible mechanism for the templation process in this study. The zirconyl nitrate precursor solution is naturally acidic (pH<1). When dissolving the pentablock copolymer template into the precursor, a mixture of micelles, unimers, and precursors form. At high temperatures and pH, cylindrical micelle structures arrange in a hexagonal close packed form,[19,22] helping to create a larger number of pores after template

removal. The sample aged at low temperature and pH would stay at the first stage in Figure 4.13, forming a large cluster of zirconia with fewer pores after calcination, as the TEM image in Figure 4.9-f and SEM image in Figure 4.11-f showed.

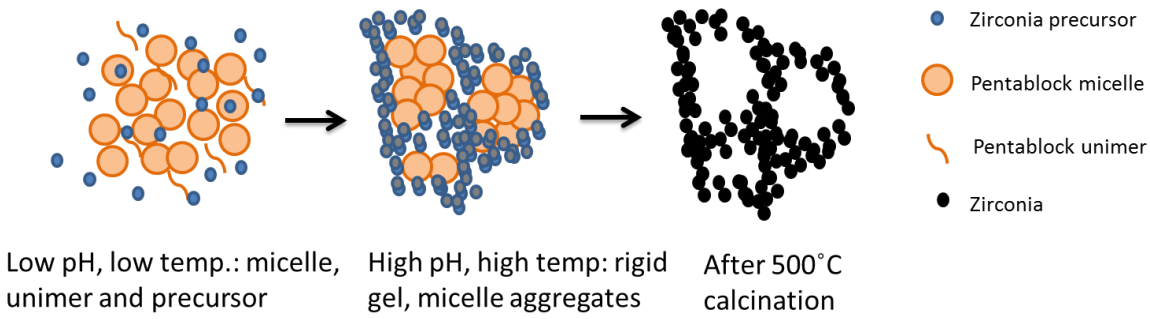


Figure 4.13 Mechanism for formation of mesoporous zirconia templated by pentablock

The differences in packing between PF127 and pentablock templates, as shown in Figure 4.12, may introduce the surface area differences between their templated zirconia. The presence of lysozyme in the conjugate potentially helped to bind to the precursor, creating smaller particle sizes after calcination, and maintaining the tetragonal phase zirconia.

## 4.4 Conclusions

In this study, we have developed a new bioinspired templation method for the synthesis of self-assembled mesoporous zirconia nanoparticles, with high surface area and a thermally stable tetragonal phase. This is also the first report of well-ordered mesoporous zirconia synthesized in completely aqueous media. We have also developed new templates for zirconia synthesis based on cationic self-assembling pentablock polymers, since cationic groups have been shown to be important in zirconia formation. The XRD, TEM and the specific surface area results indicated that pentablock copolymer templates could create the smallest zirconia nanocrystals with the highest surface area. The lysozyme and PF127 conjugate template could also produce zirconia

with much higher surface area, and maintain the tetragonal phase zirconia up to 900 ˚C. These templates could potentially be employed to synthesize other metal oxides, because the templation process is carried out in aqueous media, with facile treatment afterwards. More biological molecules could be introduced into the bioinspired synthesis, which will help to create milder synthesis conditions for the metal oxides.

## Acknowledgments

This work was supported by the U.S. Department of Energy, Office of Basic Energy Science, Division of Materials Sciences and Engineering. The research was performed at the Ames Laboratory. Ames Laboratory is operated for the U.S. Department of Energy by Iowa State University under Contract No. DE-AC02-07CH11358. Thanks to the Lujan center at Los Alamos National Lab for use of their facilities for the SANS studies. Lujan center is sponsored by the Scientific User Facilities Division, Office of Basic Energy Sciences, U.S. Dept. of Energy. Thanks to the scientists at Lujan center, Monika Hartl and Rex Hjelm, for helping on the LQD beam line. Thanks to Feng Jia at Iowa State University for helping with the SEM imaging. Thanks to Honghu Zhang at Iowa State University for helping with some of the TGA work.

## References

(1) Bansal, V.; Rautaray, D.; Ahmad, A.; Sastry, M. Biosynthesis of zirconia nanoparticles using the fungus Fusarium oxysporum. *J. Mater. Chem.* **2004**, *14*, 3303–3305.

(2) Jaenicke, S.; Chuah, G. K.; Raju, V.; Nie, Y. T. Structural and Morphological Control in the Preparation of High Surface Area Zirconia. *Catalysis Surveys from Asia* **2008**, *12*, 153–169.

(3) Yamahara, K.; Sholklapper, T. Z.; Jacobson, C. P.; Visco, S. J.; De Jonghe, L. C. Ionic conductivity of stabilized zirconia networks in composite SOFC electrodes. *Solid State Ionics* **2005**, *176*, 1359–1364.

(4) Li, Q.; Xu, J.; Wu, Z.; Feng, D.; Yang, J.; Wei, J.; Wu, Q.; Tu, B.; Cao, Y.; Zhao, D. Facile synthesis of highly stable and well-dispersed mesoporous ZrO2/carbon composites with high performance in oxidative dehydrogenation of ethylbenzene. *Phys. Chem. Chem. Phys.* **2010**, *12*, 10996–11003.

(5) Das, S. K.; Bhunia, M. K.; Sinha, A. K.; Bhaumik, A. Self-Assembled Mesoporous Zirconia and Sulfated Zirconia Nanoparticles Synthesized by Triblock Copolymer as Template. *The Journal of Physical Chemistry C* **2009**, *113*, 8918–8923.

(6) Drisko, G. L.; Zelcer, A.; Luca, V.; Caruso, R. A.; Soler-Illia, G. J. de A. A. One-Pot Synthesis of Hierarchically Structured Ceramic Monoliths with Adjustable Porosity. *Chemistry of Materials* **2010**, *22*, 4379–4385.

(7) Chen, S.-Y.; Jang, L.-Y.; Cheng, S. Synthesis of Thermally Stable Zirconia-Based Mesoporous Materials via a Facile Post-treatment. *J. Phys. Chem. B* **2006**, *110*, 11761–11771.

(8) Yang, P.; Zhao, D.; Margolese, D. I.; Chmelka, B. F.; Stucky, G. D. Generalized syntheses of large-pore mesoporous metal oxides with semicrystalline frameworks. *Nature* **1998**, *396*, 152–155.

(9) Yang, P.; Zhao, D.; Margolese, D. I.; Chmelka, B. F.; Stucky, G. D. Block Copolymer Templating Syntheses of Mesoporous Metal Oxides with Large Ordering Lengths and Semicrystalline Framework. *Chem. Mater.* **1999**, *11*, 2813–2826.

(10) Hu, Y.-Y.; Liu, X. P.; Ma, X.; Rawal, A.; Prozorov, T.; Akinc, M.; Mallapragada, S. K.; Schmidt-Rohr, K. Biomimetic Self-Assembling Copolymer−Hydroxyapatite Nanocomposites with the Nanocrystal Size Controlled by Citrate. *Chem. Mater.* **2011**, *23*, 2481–2490.

(11) Wong, M. S.; Ying, J. Y. Amphiphilic Templating of Mesostructured Zirconium Oxide. *Chem. Mater.* **1998**, *10*, 2067–2077.

(12) Armatas, G. S.; Bilis, G.; Louloudi, M. Highly ordered mesoporous zirconia-polyoxometalate nanocomposite materials for catalytic oxidation of alkenes. *J. Mater. Chem.* **2011**, *21*, 2997–3005.

(13) Fang, H.; Wan, T.; Shi, W.; Zhang, M. Design and synthesis of large-pore p6mm mesoporus zirconia thin films templated by a novel block copolymer. *Journal of Non-Crystalline Solids* **2007**, *353*, 1657–1661.

(14) Cassiers, K.; Linssen, T.; Aerts, K.; Cool, P.; Lebedev, O.; Tendeloo, G. V.; Grieken, R. V.; Vansant, E. F. Controlled formation of amine-templated mesostructured zirconia with remarkably high thermal stability. *J. Mater. Chem.* **2003**, *13*, 3033–3039.

(15) Bansal, V.; Rautaray, D.; Bharde, A.; Ahire, K.; Sanyal, A.; Ahmad, A.; Sastry, M. Fungus-mediated biosynthesis of silica and titania particles. *J. Mater. Chem.* **2005**, *15*, 2583.

(16) Jiang, Y.; Yang, D.; Zhang, L.; Jiang, Y.; Zhang, Y.; Li, J.; Jiang, Z. Facile Synthesis and Novel Application of Zirconia Catalyzed and Templated by Lysozyme. *Ind. Eng. Chem. Res.* **2008**, *47*, 1876–1882.

(17) Luckarift, H. R.; Dickerson, M. B.; Sandhage, K. H.; Spain, J. C. Rapid, Room-Temperature Synthesis of Antibacterial Bionanocomposites of Lysozyme with Amorphous Silica or Titania. *Small* **2006**, *2*, 640–643.

(18) Yusufoglu, Y.; Hu, Y.; Kanapathipillai, M.; Kramer, M.; Kalay, Y. E.; Thiyagarajan, P.; Akinc, M.; Schmidt-Rohr, K.; Mallapragada, S. Bioinspired synthesis of self-assembled

calcium phosphate nanocomposites using block copolymer-peptide conjugates. *Journal of Materials Research* **2008**, *23*, 3196–3212.

(19) Determan, M. D.; Guo, L.; Thiyagarajan, P.; Mallapragada, S. K. Supramolecular Self-Assembly of Multiblock Copolymers in Aqueous Solution. *Langmuir* **2006**, *22*, 1469–1473.

(20) Peleshanko, S.; Anderson, K. D.; Goodman, M.; Determan, M. D.; Mallapragada, S. K.; Tsukruk, V. V. Thermoresponsive Reversible Behavior of Multistimuli Pluronic-Based Pentablock Copolymer at the Air−Water Interface†. *Langmuir* **2007**, *23*, 25–30.

(21) Determan, M. D.; Cox, J. P.; Seifert, S.; Thiyagarajan, P.; Mallapragada, S. K. Synthesis and characterization of temperature and pH-responsive pentablock copolymers. *Polymer* **2005**, *46*, 6933–6946.

(22) Determan, M. D.; Guo, L.; Lo, C.-T.; Thiyagarajan, P.; Mallapragada, S. K. pH- and temperature-dependent phase behavior of a PEO-PPO-PEO-based pentablock copolymer in aqueous media. *Phys. Rev. E* **2008**, *78*, 021802.

(23) Rezaei, M.; Alavi, S. M.; Sahebdelfar, S.; Yan, Z.-F. Effect of process parameters on the synthesis of mesoporous nanocrystalline zirconia with triblock copolymer as template. *Journal of Porous Materials* **2007**, *15*, 171–179.

(24) Kresge, C. T.; Leonowicz, M. E.; Roth, W. J.; Vartuli, J. C.; Beck, J. S. Ordered mesoporous molecular sieves synthesized by a liquid-crystal template mechanism. *Nature* **1992**, *359*, 710–712.

(25) Yuan, Q.; Li, L.-L.; Lu, S.-L.; Duan, H.-H.; Li, Z.-X.; Zhu, Y.-X.; Yan, C.-H. Facile Synthesis of Zr-Based Functional Materials with Highly Ordered Mesoporous Structures. *The Journal of Physical Chemistry C* **2009**, *113*, 4117–4124.

(26) Răileanu, M.; Todan, L.; Crişan, D.; Drăgan, N.; Crişan, M.; Stan, C.; Andronescu, C.; Voicescu, M.; Vasile, B. S.; Ianculescu, A. Sol–gel zirconia nanopowders with α-cyclodextrin as organic additive. *Journal of Alloys and Compounds* **2012**, *517*, 157–163.

(27) Sharma, P. K.; Matthew, J. E.; Bhatia, S. R. Structure and assembly of PEO-PPO-PEO co-polymers in mammalian cell-culture media. *J Biomater Sci Polym Ed* **2005**, *16*, 1139–1151.

(28) Enlow, D.; Rawal, A.; Kanapathipillai, M.; Schmidt-Rohr, K.; Mallapragada, S.; Lo, C.-T.; Thiyagarajan, P.; Akinc, M. Synthesis and characterization of self-assembled block copolymer templated calcium phosphate nanocomposite gels. *J. Mater. Chem.* **2007**, *17*, 1570.

(29) Pozzo, D. C.; Walker, L. M. Small-angle neutron scattering of silica nanoparticles templated in PEO–PPO–PEO cubic crystals. *Colloids and Surfaces A: Physicochemical and Engineering Aspects* **2007**, *294*, 117–129.

## Supporting Information

The covalent attachment between PF127 and lysozyme was confirmed by the FPLC, as shown by Figure 4.14. PF127 does not have absorbance under these conditions. The conjugate with larger

molecular weight came out of the column faster than the lysozyme. The solution of the conjugation reaction, and some of the fractions from the conjugate peak and the lysozyme peak were randomly selected to run a SDS-PAGE, as shown by Fiure 2. We can see that lysozyme, with a molecular weight of 14.7 kD, only exited in the lysozyme fractions, which confirmed the assignment of the FPLC peaks. Figure 4.15 also clearly showed the formation of the conjugate, with a molecular weight larger than 30 kD. The larger molecular weight may due to the unspecific binding between the NHS modified PF127 and the free amine groups in lysozyme.

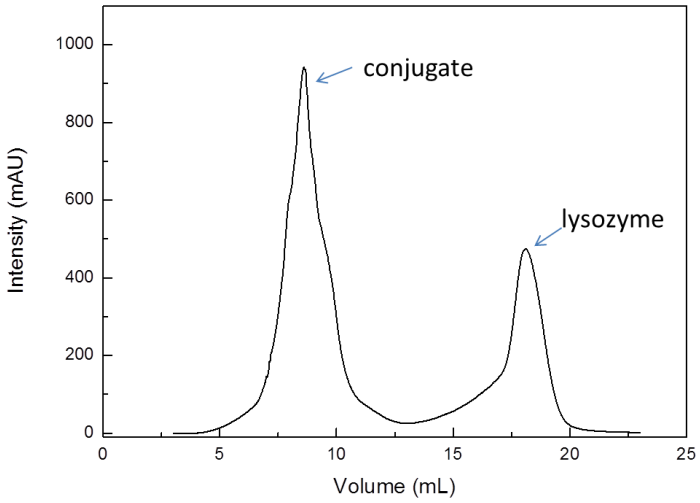


Figure 4.14 FPLC result of the solution after the conjugate reaction between lysozyme and PF127

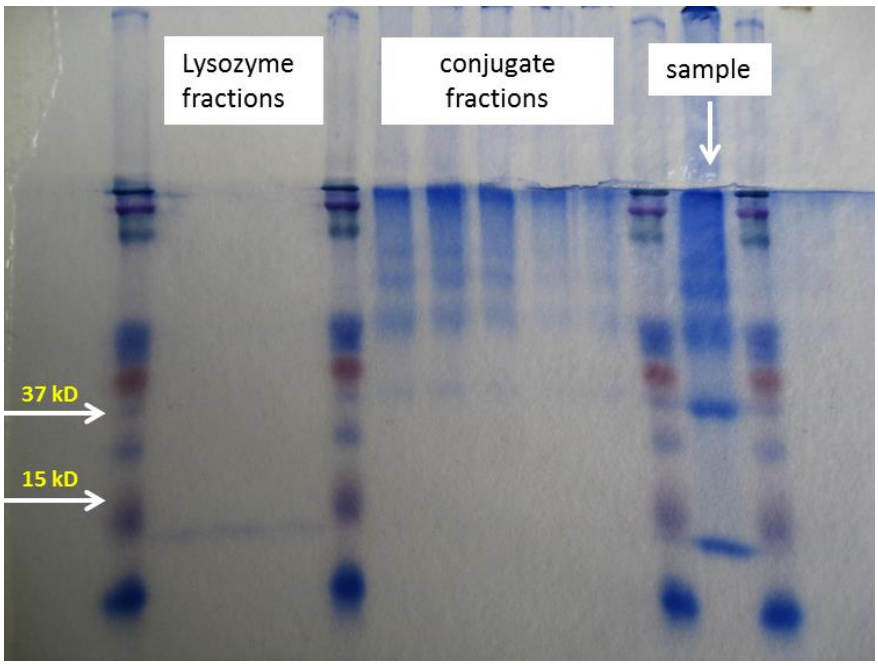


Figure 4.15 SDS-PAGE for fractions separated by FPLC, and the reaction solution

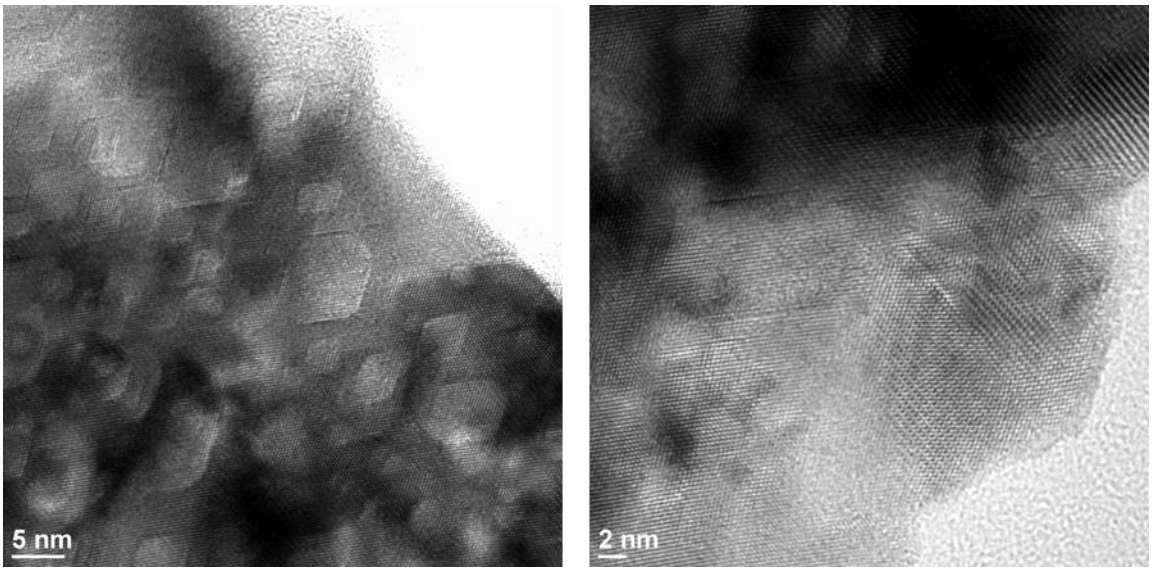


Figure 4.16 HRTEM of Figure 4.10-a.

# Chapter 5 Synthesis of mesoporous zirconia templated by block copolymer-lysozyme conjugate in aqueous media

Qinwen Ge, Xunpei Liu, German Parada, Surya K. Mallapragada, and Mufit Akinc*

This chapter is a paper submitted to *Science of Advanced Materials*. My contribution focused on synthesis and characterization of the block copolymer-lysozyme conjugate, and characterization of the mesoporous zirconia by XRD and TEM.

## Abstract

High surface area mesoporous zirconia/polymer nanocomposite was obtained using a block copolymer-lysozyme conjugate template and applying aqueous sol-gel method. The effects of several parameters such as pH, zirconium ion concentration, and calcination temperature on the structure and morphology of the resulting mesoporous zirconia were studied. Samples were characterized by X-ray diffraction (XRD), nitrogen sorption, and transmission electron microscopy (TEM). The results showed that tetragonal zirconia started to crystallize from amorphous precipitate above 300˚C, became fully crystalline above 500˚C, grew larger with higher temperatures, and a monoclinic phase formed above 900˚C. It was also found that a more dilute precursor solution leads to more thermally stable and smaller particles with higher surface area. Likewise, higher pH (such as pH=10), is more conducive for obtaining higher surface area, thermally stable tetragonal zirconia with smaller particle sizes compared to ones precipitated at pH=4, 6, and 8. The aging at pH=4 formed ill-defined gels rather than distinct particles. The surface area of the synthesized zirconia increased with calcination temperature up to 500˚C, reaching a maximum with a specific surface area of 348 $m^2/g$ using 0.08 mol/L [$ZrO^{2+}$] and precipitating at pH=10 before decreasing at higher temperatures.

## 5.1 Introduction

Synthesis of zirconium dioxide, the major component of a well-known structural ceramic, continues to receive a lot of interest from the scientific community. The engineering properties such as hardness, shock resistance, chemical inertness, low frictional resistance, and high thermal stability make zirconia a potential candidate for refractory materials, fuel cell membranes, sensors, catalysts or catalyst carriers, biomedical materials, and hot metal extrusion dies.[1-7] Some of these applications, especially catalytic applications, require high surface area and nano-sized, uniform pore structure. Therefore, a large number of methods have been explored to obtain fine zirconia powders with high surface area and fine pore structure, such as sol-gel, aqueous precipitation, hydrothermal synthesis, microwave, hard and soft templating.[8-23] Among them, the surfactant assisted sol-gel method has received considerable attention for the synthesis of nanostructured mesoporous zirconia powders with high surface area. Many surfactants, such as block copolymers,[1] the non-ionic surfactants PEG–PPG–PEG,[24] the hydroxyl propyl cellulose (HPC) polymer[25], the cationic protein lysozyme[26], and agarose[11] have been explored. In this paper, we have employed a Pluronic block copolymer-lysozyme conjugate as a template, since a previous study showed that this polymer conjugate yielded oxides with higher surface area as well as uniform size pores.[27] A number of experimental variables play a significant role in determining the characteristics of the zirconia powder formed by this process. Chuah and coworkers reported digestion time and temperature as key factors in obtaining high surface area.[28] Stefanic and others reported that the pH value has a significant influence on the phase transformation and surface area.[29] Rezaei and others reported that the surfactant-to-zirconium molar ratio is also an important parameter in this process.[1] Deshmane and Adewuyi showed that the calcination temperature had a profound influence on the surface area and crystallization - particles grew larger and surface area decreased dramatically when samples were heat treated at high temperature.[30] Stichert and

Schuth reported the influence of the precursor concentration; they found that lower precursor concentration would lead to smaller particle size, more stable tetragonal phase and higher surface area.[31] In this paper, the role of several experimental variables on the characteristics of the resulting zirconia powder was investigated. In particular, the conditions leading to high surface area, mesoporous, nanostructured zirconia powders using the conjugate templates were established. The surface area under the optimized condition was about 348 m2/g, increased two fold compare to our previous study.[27] This number is the highest number we have noticed for the aqueous zirconia synthesis, and is even very comparable to the mesoporous zirconia synthesized in organic solvents.[32]

## 5.2 Experimental

### 5.2.1 Chemicals and Materials

Triblock copolymers, poly (ethylene oxide)-b-poly (propylene oxide)-b-poly (ethylene oxide) Pluronic F127 (PF127) ($PEO_{100}PPO_{65}PEO_{100}$, $M_{av}$ = 12600 g $mol^{-1}$), lysozyme from chicken egg white, zirconium (IV) oxynitrate hydrate ($ZrO(NO_3)_2 \cdot xH_2O$) (99.99%), succinic anhydride, and N-hydroxy succinimide (NHS) were all purchased from Sigma-Aldrich (St. Louis, MO, USA). Ammonium hydroxide was purchased from Fisher Scientific (Pittsburgh, PA, USA). All of the chemicals were used without further treatment.

### 5.2.2 Synthesis of Pluronic-lysozyme conjugate template

The method of synthesis of Pluronic-lysozyme conjugate was reported earlier.[33] The hydroxyl end groups of PF127 Pluronic were converted to carboxyl groups by reacting with succinic anhydride in pyridine. The carboxyl-terminated PF127 was activated by reaction with NHS at room temperature for 24 h. The NHS-activated PF127 was then covalently bonded (conjugated) with lysozyme. After reacting at room temperature for 24 h in phosphate buffered saline buffer,

the mixture was dialyzed against water using a cellulose ester membrane with a molecular weight cut off of 25,000 (Thermo Scientific), for 4 days at room temperature to remove the unreacted polymer and lysozyme. The mixture was then freeze-dried to form the solid conjugate.

### 5.2.3 Synthesis of the mesoporous zirconia nanocomposite

In a typical experiment, 0.231 g zirconyl nitrate $ZrO(NO_3)_2 \bullet xH_2O$ was dissolved in 10 mL deionized water to make 0.08 mol/L $ZrO(NO_3)_2$ solution. Similarly, 1.15 or 2.31 g zirconyl nitrate hydrate was used to prepare 0.4 or 0.8 mol/L solution. 2.6 g PF127 and 0.4 g Pluronic-lysozyme conjugate were dissolved in the precursor solution. For each experiment, the total polymer content was kept constant at 3 g, and was added at 4 ̊C. The solution was then brought to room temperature, and dilute ammonium hydroxide (about 30%) was added dropwise with pipette and with continuous stirring, until the solution reached a predetermined, desired pH value (4, 6, 8, or 10). A white precipitate was formed during this step. The precipitated gel was then aged at room temperature for 3 days, rinsed with deionized water and centrifuged for 3 times (15 minutes at 4400 rpm) to remove ammonium nitrate and the free polymers. The composite was then calcined at 300, 500, 700 or 900 ˚C for 3 hours in air.

### 5.2.4 Characterization

The samples were characterized at various stages of preparation to investigate crystal structure, surface area, porosity, and morphology by X-ray diffraction (XRD), nitrogen sorption, and transmission electron microscopy (TEM) respectively.

**X-Ray Diffraction**. Diffraction patterns were obtained using an X'Pert PRO X-ray diffractometer (PANalytical Inc., Westborough, MA, USA). Operational parameters of the diffractometer were set at 45 kV and 40 mA, with a scan rate of 0.021 °/s and step size of 0.017 °, over the range of $20^\circ \leq 2\Theta \leq 80^\circ$. CuKα radiation with a wavelength of λ=1.54059 Å was used for

the monochromatic light, X'pert Data collector software was used to collect the data. Crystallite size was estimated with well-known Scherrer equation.

**Nitrogen sorption**. Nitrogen sorption isotherms were carried out using an AUTOSORB-1 Physisorption analyzer (Quantachrome Corporation, Boynton Beach, FL, USA) at 77 K, the Quantachrome Autosorb Software was used for collecting and processing the data. All samples were degassed under vacuum at 110 ˚C overnight prior to adsorption. Surface area was calculated by applying Brunauer-Emmett-Teller (BET) method and using the sorption data in the $0.03<P/P_0<0.3$ range. Pore size distribution was calculated using Barrett-Joyner-Halenda (BJH) method and the desorption branch of the isotherm. The total pore volume was estimated from the volume of nitrogen adsorbed near saturation pressure.

**TEM**. TEM images were taken using a Tecnai G2 F20 Scanning Transmission Electron Microscope (STEM) (FEI Company, Hillsboro, OR, USA) operating at 200 kV with High Angle Annular Dark Field (HAADF) and Energy Dispersive X-ray Spectroscopy (EDS) detectors. About 20 μL of diluted zirconia powder suspension was placed on a mesh carbon-supported copper grid and left in ambient atmosphere until the water evaporates completely before loading it to TEM.

## 5.3 Results and Discussion

### 5.3.1 The effect of calcination temperature

Crystallization, surface area, and pore size distribution of the synthesized powders were followed as a function of calcination temperature. Figure 5.1 shows the XRD patterns of a typical zirconia sample ($[ZrO^{2+}]$ = 0.4 M and pH=10) as a function of temperature. At room temperature, the sample is amorphous. At 300 ˚C, tetragonal zirconia starts to form and becomes fully crystallized at 500 ˚C. At 700 ˚C, the tetragonal zirconia crystals grew larger. At 900 ˚C, the

sample was still tetragonal, but small monoclinic phase peaks (such as the small peak at 2θ=28˚) also emerged. Even after calcination at 900 ˚C, the approximate crystallite size was about 20 nm (see Table 1).

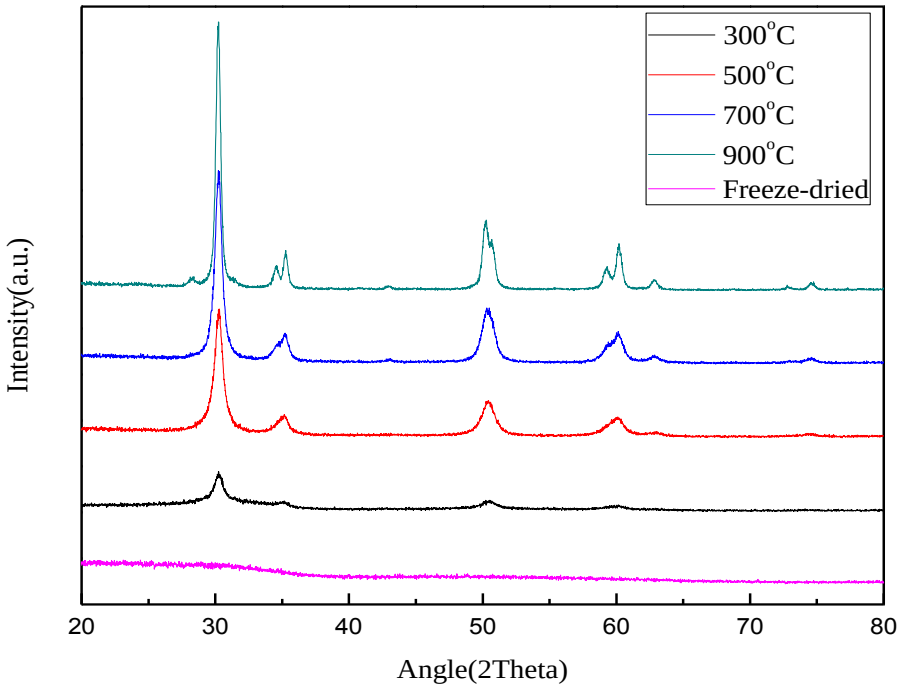


Figure 5.1 XRD patterns for 0.4M-pH10 zirconia samples after calcination at indicated temperatures.

As shown in Table 5.1, the specific surface area of the sample increased from 41 $m^2/g$ at room temperature to its maximum value of 174 $m^2/g$ at 500 ˚C before decreasing progressively as the calcination temperature increased. Before heat treatment (after freeze-drying) the sample contains precipitated hydrated zirconia ($ZrO_2 \cdot xH_2O$) and the Pluronic-lysozyme polymer template. At 300 ˚C, Pluronic-lysozyme polymer started to pyrolyzed and hence the surface area increased. At 500 ˚C, dehydration/deyhdroxylation of the zirconia was nearly complete, and hence the

powder at this stage was pure zirconia and exhibited an open structure with highest surface area and porosity. As the sample was heated to higher temperatures, the specific surface area and porosity decreased. At 900 ˚C, the sample exhibited a specific surface area of 31 $m^2/g$. Initial increase in surface area with temperature may be attributed to the removal of the polymeric template and evolution of structural water and hydroxide from zirconia precipitate, while the decrease in surface area during change in annealing temperature from 500 to 900 ˚C is due to crystal growth and the collapse of pores at elevated temperatures.

Table 5.1 Nitrogen sorption isotherm and crystal size data for 0.4M-pH10 zirconia samples at several calcination temperatures

| Calcination temperature, ˚C | Freeze-dried | 300 | 500 | 700 | 900 |
|---|---|---|---|---|---|
| Specific Surface area, $m^2/g$ | 41 | 143 | 174 | 86 | 31 |
| Total pore volume, mL/g | 0.10 | 0.16 | 0.20 | 0.13 | 0.08 |
| Average pore size, nm | 10 | 4.3 | 4.5 | 6.2 | 10 |
| Crystal size calculated from T(101), nm | amorphous | amorphous | 12 | 13.4 | 20 |

Figure 5.2 shows that at the freeze-drying stage, the zirconia sample does not show significant amount of porosity in the range where the adsorption isotherm is applicable. When the polymer template was removed by heat treating at 300 ˚C, the powder showed a significant level of porosity centering around 3-4 nm. The highest level of porosity was observed after 500 ˚C again, and the peak in pore size was around 3.6 nm. Increase in temperature led to a decrease in the pore volume as well as a shift of the maximum to larger sizes, indicating crystal growth.

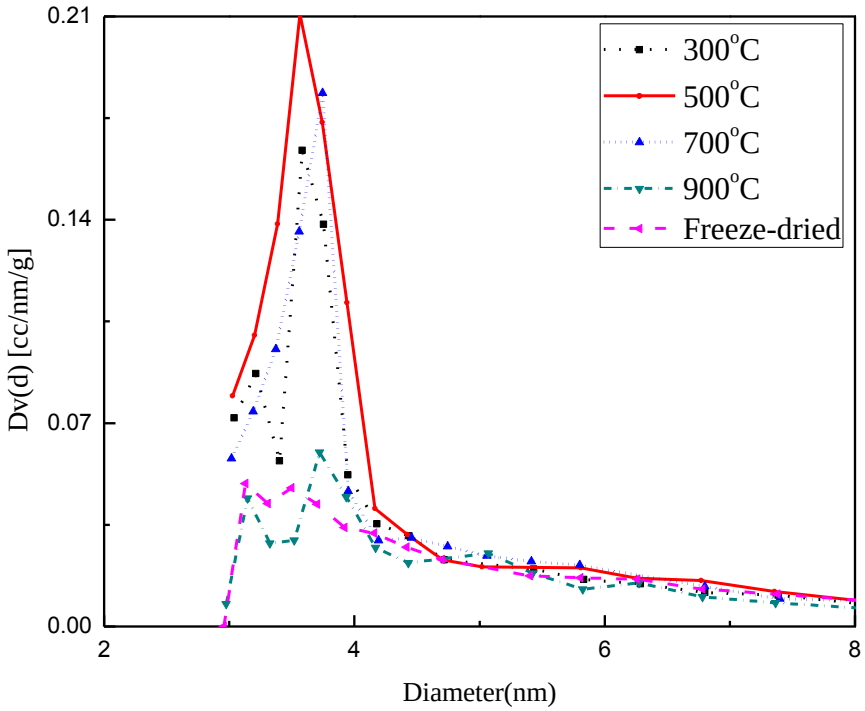


Figure 5.2 Pore size distributions for the 0.4M-pH10 sample after freeze drying and heat treatment at indicated temperatures

After heat treatment at 900 ˚C, essentially all the mesopores collapsed. These observations are consistent with the surface area measurements. It is interesting to note that the pore size distribution in the 4 and 8 nm range remained constant irrespective of the heat treatment, indicating that the surface area was primarily determined by the pores in the 3-4 nm range.

Figure 5.3 shows the TEM images of the nanocomposite (freeze-dried) and the zirconia nanoparticles formed after heat treatment. Smaller and distinct particles were observed after heat treatment at temperatures as low as 300 ˚C. The particle size increased as the heat treatment temperature increased.

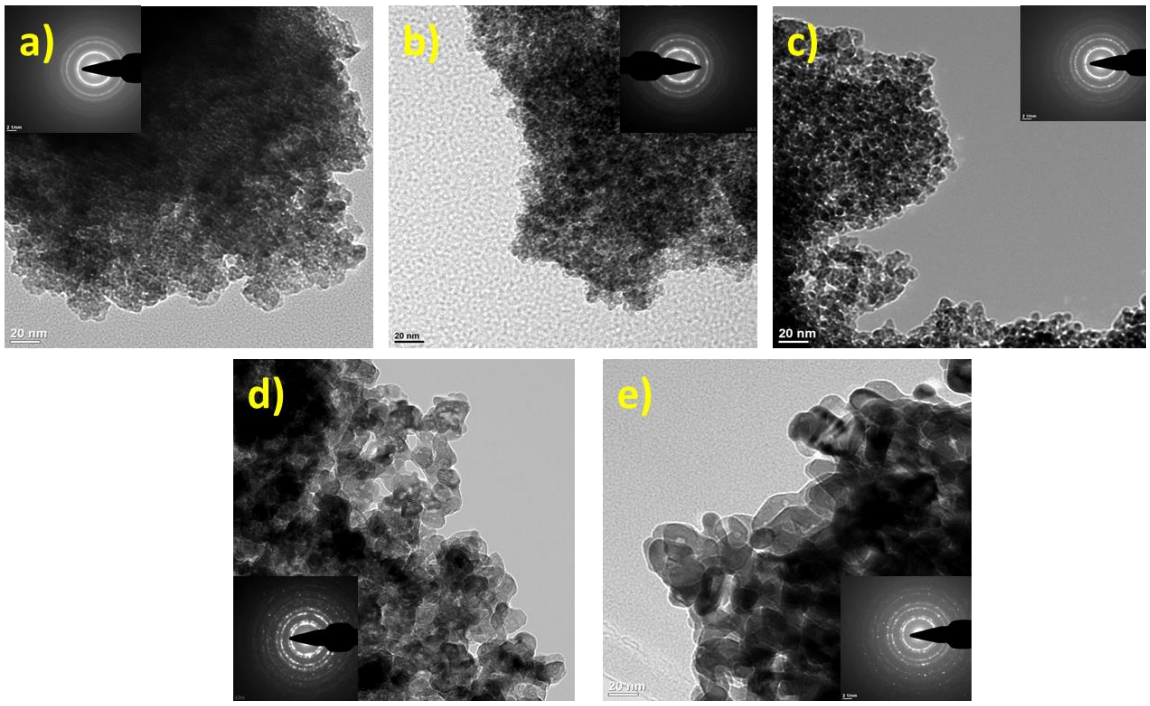


Figure 5.3 TEM images and diffraction patterns of freeze-dried nanocomposite: a) Freeze-dried, and heat treated at: b) 300, c) 500, d) 700, and e) 900 ˚C for 3 h. The samples were synthesized starting with 0.4 M $ZrO(NO_3)_2$ precursor and aged at pH 10.

Crystallite size was estimated to be less than 10 nm at 300˚C, progressively increasing to about 20-30 nm at 900 ˚C in agreement with the XRD observations. The inset of Figure 5.3-e shows the diffraction pattern of the zirconia calcined at 900 ˚C, which is consistent with that of tetragonal phase[34-36], indicating that the nanocrystalline zirconia templated by the lysozyme conjugate has excellent thermal stability.

### 5.3.2 Zirconyl ion concentration

Crystallization, specific surface area and pore size distribution of the synthesized zirconia were studied as a function of zirconium concentration. Figure 5.4 shows that after 500 ˚C calcination, the samples prepared using three different precursor concentrations (0.08, 0.4, and

0.8 mol/L) and at pH=10, all exhibited tetragonal phase, and the crystal size increased with increasing zirconyl ion concentration as evident from the sharpening of the diffraction peaks as the concentration increased. Although peak splitting due to tetragonal crystal structure is not obvious at low concentrations, it is inferred in the 0.4 M sample from the asymmetry of thee peaks at 2θ≈35 and 60. The calculated crystal sizes using T (101) are listed in Table 2, and are consistent with the TEM observations.

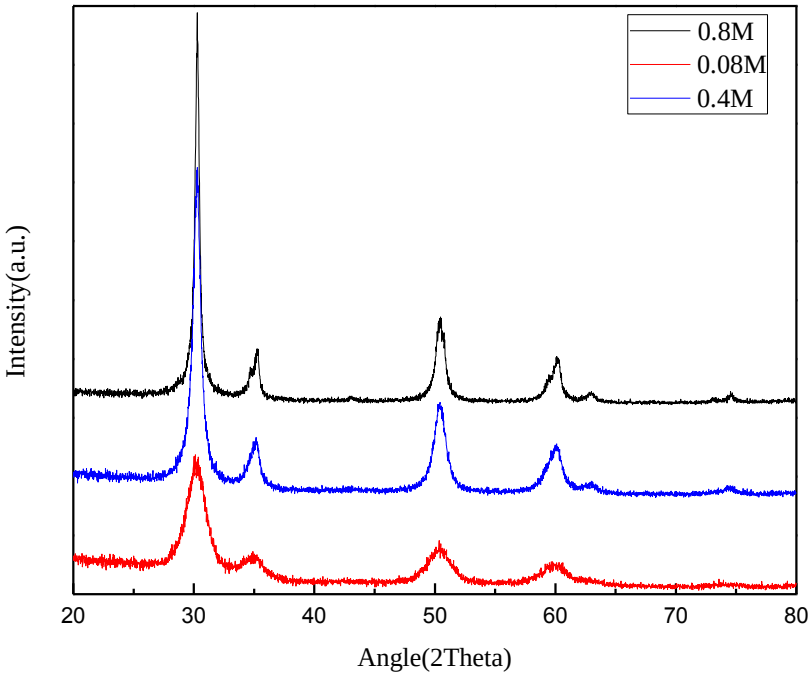


Figure 5.4 XRD patterns for 500 ˚C-pH10 samples prepared at several zirconium ion concentrations.

Table 5.2 shows the specific surface area of the samples calcined at 500 ˚C prepared using [$ZrO^{2+}$]= 0.08, 0.4, and 0.8 mol/L and at pH=10. Highest specific surface area of 348 $m^2/g$ was obtained at a [$ZrO^{2+}$] concentration of 0.08 mol/L. Again, specific surface area correlates well with the crystal size calculated from X-Ray line broadening and particle sizes seen in TEM micrographs.

Table 5.2 Nitrogen sorption isotherm and crystal size data for 500 ˚C-pH10 zirconia samples prepared at several zirconyl ion concentrations.

| $[ZrO^{2+}]$, mol/L | 0.08 | 0.4 | 0.8 |
|---|---|---|---|
| Specific surface area, $m^2/g$ | 348 | 174 | 93 |
| Total pore volume, mL/g | 0.52 | 0.20 | 0.19 |
| Average pore size, nm | 6.0 | 4.5 | 8 |
| Crystal size calculated from T(101), nm | 5 | 12 | 20 |

Figure 5.5 shows the pore size distribution for three samples. All three samples exhibited a single peak centering around 3.6-3.8 nm, and the largest pore volume was observed for the 0.08 mol/L sample. In addition, this sample showed larger size pores extending to about 11 nm while the higher concentration samples had little porosity above 4.2 nm. It might be inferred that the larger pore sizes observed for lowest zirconyl concentrations may be due to loose packing of very fine particles, while the small but prominent pores around 3.6-3.8 nm were formed by pyrolysis of the templating polymer scaffolds. Pore volume data correlates well with the specific surface area measurements, and the higher the pore volume, the higher the specific surface area.

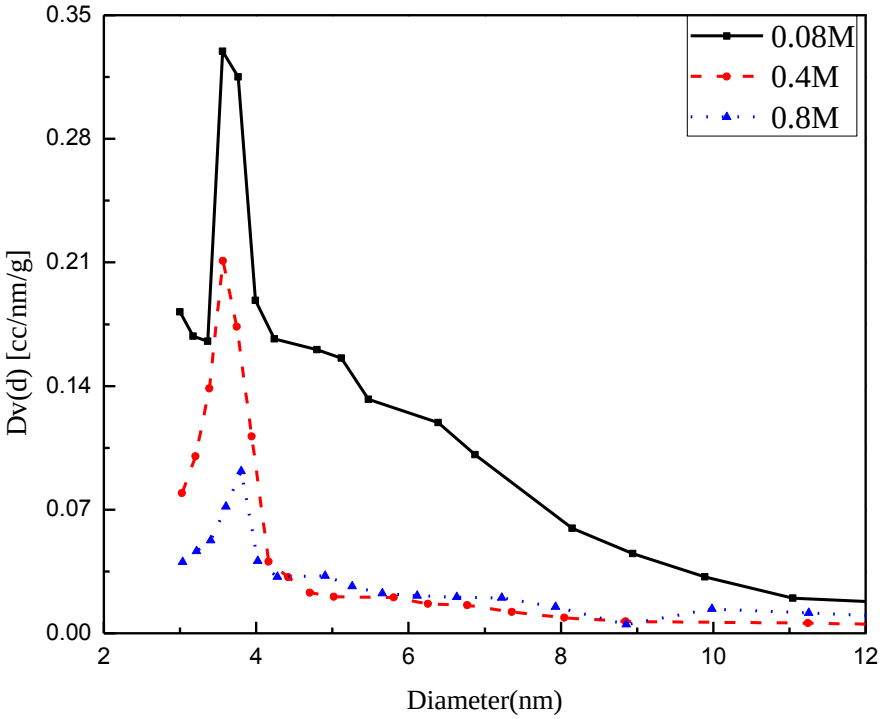


Figure 5.5 Pore size distributions for 500 ˚C-pH10 samples prepared using different precursor concentration

Increase in particle size with the zirconyl ion concentration is also depicted in TEM micrographs as shown in Figure 5.6. The estimated particles sizes from the images were about 5 nm, 10 nm and 20 nm for the zirconia prepared with precursor concentrations of 0.08, 0.4 and 0.8 mol/L, respectively. These observations were also consistent with the specific surface area values, and explain why the zirconia with 0.08 M precursor concentration had the maximum specific surface area. SAED patterns of the respective samples indicate that the zirconia synthesized with 0.8 mol/L precursor concentration did not exhibit as neat a pattern as the other two, perhaps due to emergence of a small fraction of monoclinic phase already[34-36] as indicated by the XRD patterns more clearly of the zirconia heat-treated at 900 ˚C.

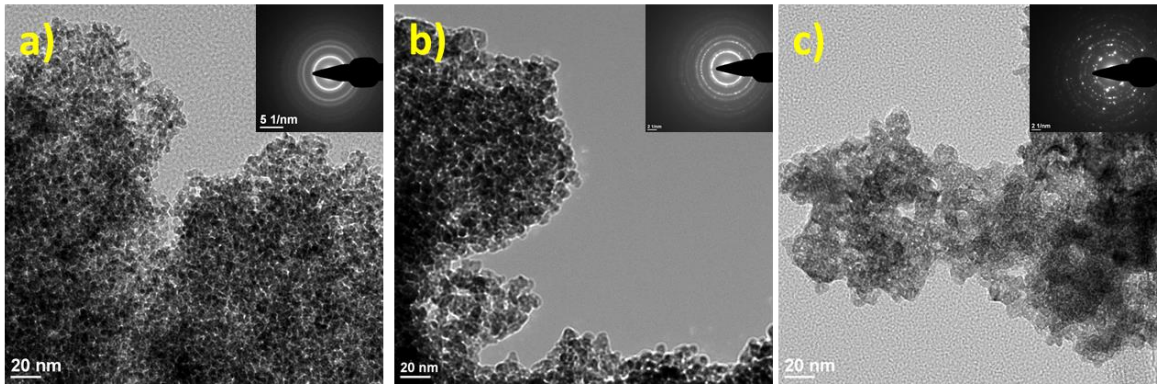


Figure 5.6 TEM images and SAED patterns of zirconia calcined at 500 ˚C for 3 h, with $ZrO(NO_3)_2$ concentration: a) 0.08, b) 0.4, and c) 0.8 mol/L. All the samples were aged at pH=10.

Figure 5.7 shows that after calcination at 900 ˚C, the 0.08mol/L concentration sample still exhibits tetragonal phase while the 0.4 mol/L sample exhibits minor monoclinic phase in addition to more dominant tetragonal peaks, but the 0.8 mol/L sample is almost completely transformed to monoclinic phase at this temperature. Apparently, small crystallite sizes retain metastable tetragonal phase at much higher temperatures than larger crystals. This result is in good agreement with previous studies of Stichert and Schüth who postulated that large precursor particle size will lead to monoclinic phase after calcination, while smaller precursor particle size will lead to tetragonal phase[31].

The results presented above show that the concentration of the starting precursor had a significant influence on the physical characteristics of the mesoporous zirconia. The first conclusion we can derive from the results is that lower zirconium precursor concentration will lead to smaller crystal size, higher porosity and a concomitant higher specific surface area. Although one might surmise incorrectly that lower zirconium concentration would lead to fewer

nuclei generation hence forming larger particles, our results are consistent with earlier similar studies[24, 25, 30, 31, 37].

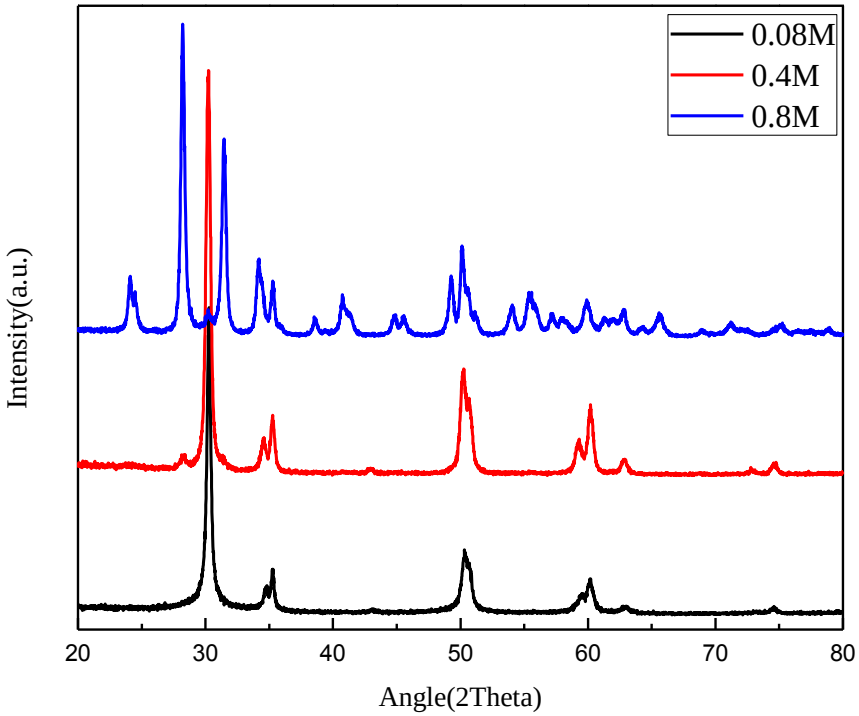


Figure 5.7 XRD patterns for samples after heat treatement at 900 ˚C prepared using [$ZrO^{2+}$] = 0.08, 0.4, and 0.8 mol/L and pH=10.

To resolve the apparent discrepancy, we would like to draw attention to the work of Stichert and Schuth[31] who proposed that the crystallization is a result of agglomeration of small precursor particles, so that the crystal size after calcination is determined by the precursor primary particle size. Thus, a dilute precursor solution leads to smaller precursor primary particles which will further result in smaller crystal sizes after calcination and vice versa which is consistent with what was observed in this study. These authors also pointed out that the precursor particle size has a significant influence on the crystal structure of zirconia. They stated that large precursor particle size will lead to a monoclinic phase after calcination, while smaller precursor particle size

will lead to a tetragonal phase. This hypothesis is also in good agreement with our results. Shubhlakshmi et al also reported that lower concentration precursor solution leads to smaller crystal size and fewer agglomerates after calcination. [25, 38] Later, Kongwudthiti et al,[37] Deshmane and Adewuyi[30] reported similar results. A most recent study by Eltejaei and et al[24] obtained similar results but offered an alternate explanation claiming that at higher concentrations, ions will compete with the surfactant's hydrophilic part for water molecules leading to reduced surfactant solubility and to a decrease in specific surface area of the precipitated powder.

### 5.3.3 The effect of pH

The precipitation pH plays an important role in the sol-gel synthesis. Figure 5.8 shows that after calcination at 500 ˚C, all samples exhibited tetragonal phases. The samples precipitated at pH=10 had broader XRD peaks compared with the other three samples, indicating smaller crystalite size. Crystal size calculated from X-ray line broadening also followed the same trend and was in good agreement with specific surface area and TEM observations mentioned above. Table 5.3 shows that the average pore size decreased while the surface area increases with increasing pH. Samples precipitated at pH=4 had the lowest specific surface area among the four samples; the samples precipitated at pH=6 and 8 had similar surface area values while the sample precipitated at pH=10 had the largest specific surface area. These observations are in good agreement with earlier reports.[28-30, 39-41]

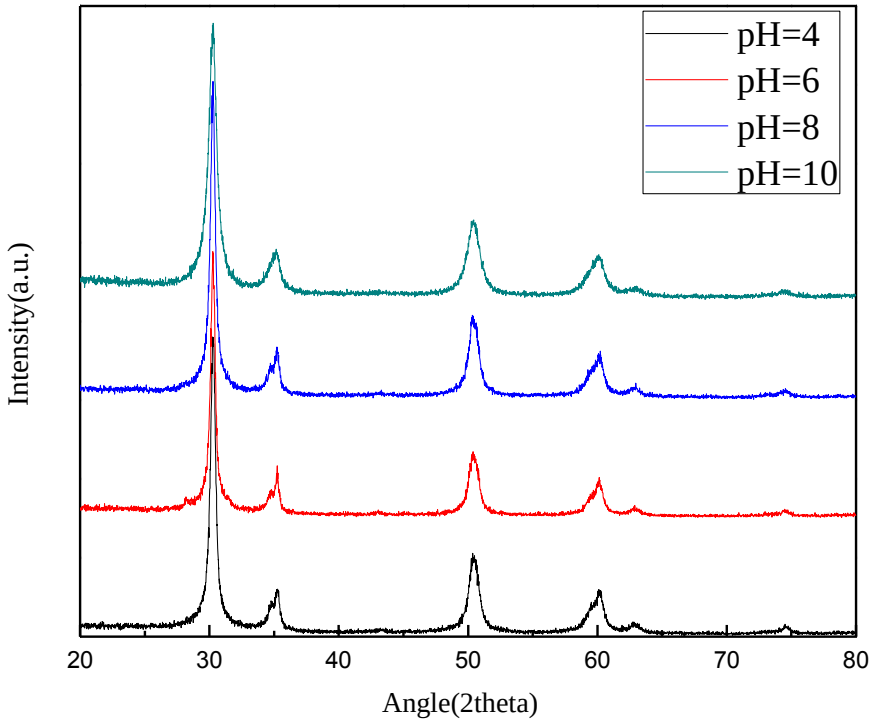


Figure 5.8 XRD patterns of samples precipitated at pH 4, 6, 8, and 10, and heat treated at 500 ˚C, with 0.4M zirconia precursor.

Table 5.3 Nitrogen sorption isotherm and crystal size data for samples precipitated at several pH using [$ZrO^{2+}$] = 0.4 mol/L and heat treated at 500 ˚C.

| Precipitate pH | 4 | 6 | 8 | 10 |
|---|---|---|---|---|
| Total pore volume, mL/g | 0.12 | 0.16 | 0.15 | 0.20 |
| Average pore size, nm | 5.5 | 5.1 | 5.2 | 4.5 |
| specific surface area, $m^2/g$ | 86 | 129 | 125 | 174 |
| Crystal size calculated from T(101), nm | 18 | 19 | 19 | 10 |

Figure 5.9 shows the pore size distribution for the samples precipitated at pH = 4, 6, 8, and 10. Clearly, all samples exhibit a single major peak within the mesopore range, centering around 3.5-3.7 nm, largest pore volume is observed for pH=10. In addition, the sample precipitated at pH=4

showed much lower pore volume than the other three samples, which also corroborates with the specific surface area results.

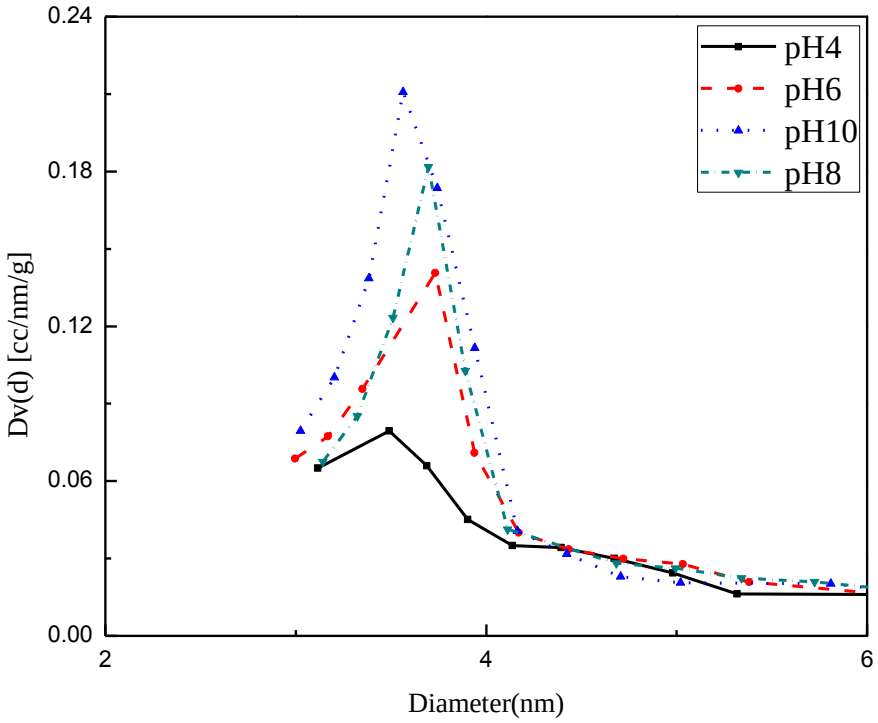


Figure 5.9 Pore size distributions for 500 ˚C-0.4M samples prepared at pH=4, 6, 8, and 10.

Figure 5.10 shows the TEM images and SAED patterns of the samples. The diffraction patterns indicate that all samples exhibit tetragonal phase of zirconia[34-36]. Micrographs representing sample precipitated at pH=4 (which are well crystallized as illustrated by XRD and SAED patterns) shows no distinct particle features. It may be that initial amorphous particles were large to begin with and fused during the heat treatment to blur distinct particle boundaries. This also explains why this sample exhibits relatively low surface area. Zirconia aged at pH=6 and pH=8 are shown in Figure 5.10-b and 10-c, and they exhibit similar features. Zirconia formed

at pH=10 had the smallest particle size, and BET surface area showed that it had the largest surface area. These results were all self-consistent and support the data presented in Table 3.

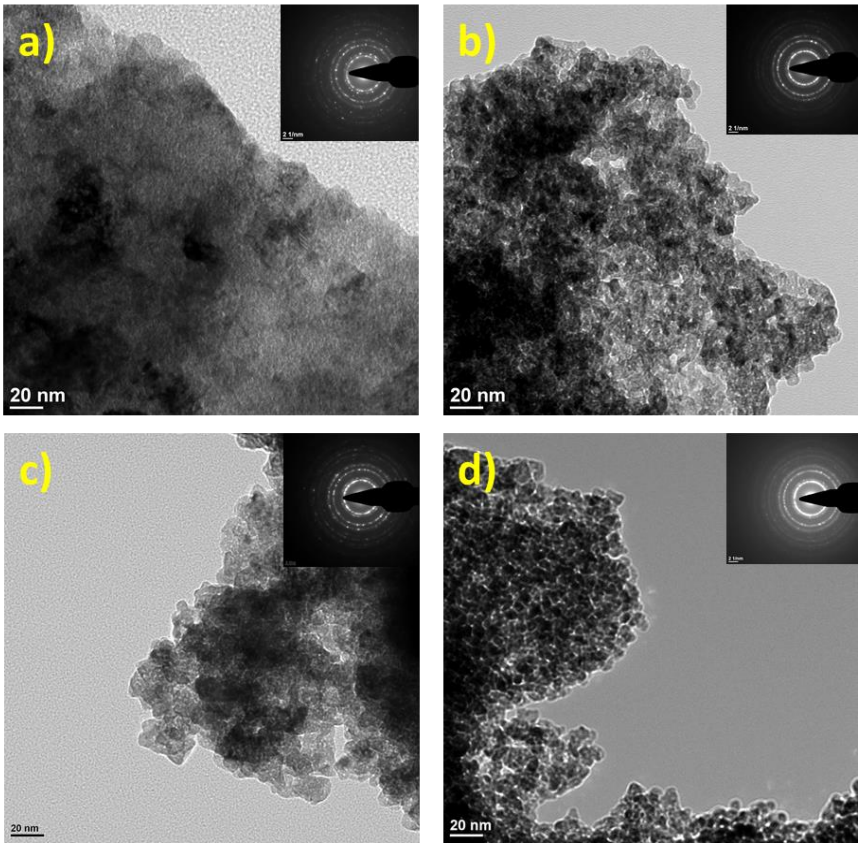


Figure 5.10 TEM images and electron diffraction patterns zirconia precipitated at: a) pH=4, b) pH=6, c) pH=8, and d) pH=10 after heat treatment at 500 ˚C. All samples were synthesized using 0.4 mol/L zirconyl ion concentration.

Figure 5.11 shows that samples precipitated at $4 \leq pH \leq 8$ display a coexistence of both tetragonal and monoclinic phases after heat treatment at 900 ˚C, while the pH=10 sample is still tetragonal with only a small monoclinic peak emerged around $2\theta = 28^{\circ}$ indicating the beginning of formation of the monoclinic phase. The data presented above demonstrate that the pH value during precipitation has a significant influence on the physical properties of the final zirconia

powder. The point of zero charge (pzc) of hydrous zirconia is around pH = 4-6 depending on the supporting ions in the solution[41-45]. So, the precipitated particles will assume a positive charge below the pzc.[46-49] Therefore, zirconia particles tend to flocculate around the pzc due to the diminishing repulsive forces between the particles. In this case, the particles precipitated at pH = 4 and pH = 6 exhibited little or no repulsion. The sample prepared at pH=4 appeared to form a gel structure rather than distinct particles as shown in Figure 5.10, thus leading to low surface area and low porosity as shown in Table 3. Based on pzc argument only, the sample prepared at pH=6 should exhibit similar morphology but apparently surface charge is not the only factor in determining the particle morphology. This result is in good agreement with earlier study by Chuah and et al.[40], who reported that digestion in acidic medium resulted in a lower surface area both for hydrous oxides and the calcined zirconia. When the pH is low as is the case with the starting zirconyl nitrate solution, the Pluronic-lysozyme copolymer's carboxylic acid groups are largely undissociated and hence show limited affinity to associate with zirconyl ions prior to precipitation. Even when zirconia is precipitated at pH = 4 the association with the carboxylic acid groups is not strong nor is the repulsion between the particles. Furthermore, solubility of freshly precipitated zirconia hydrate is higher in acidic medium - thus aging at low pH leads to formation of gel-like structure as shown in Figure 5.10a. When the pH is increased to 8 and 10, the hydrous zirconia in the solution is negatively charged, so they interact strongly with the cationic surfactant which leads to a mesoporous structure[39-41]. In our experiments, Pluronic-lysozyme copolymer exhibits negatively charged carboxylate groups that associate with positively charged zirconyl ions. When zirconia is precipitated and aged at pH = 8 and pH = 10, the precipitated particles are negatively charged preventing flocculation and/or gel formation leading to nanoscale distinct particles as illustrated in Figure 5.10c and 10d. These samples had high porosity after 500 ˚C heat treatment. The samples precipitated at pH = 6 and pH = 8 had

similar surface areas, and perhaps the low solubility of $ZrO_2$ in this pH range leads to a relatively low level of supersaturation compared to the ones at high pH range.[28, 29, 40] At pH = 10, the solubility of $ZrO_2$ is higher than in pH=6 and 8, leading to more nuclei formation and hence smaller particles[29, 30] as shown in Figure 5.10d, and smaller crystallite size and a higher surface area as shown in Table 3.

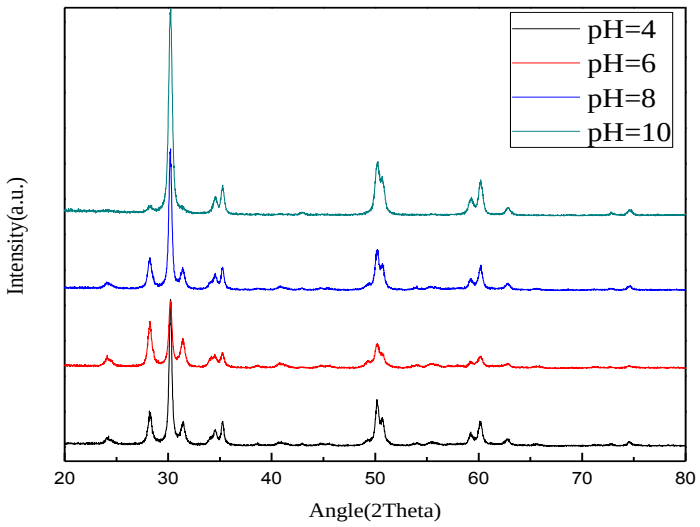


Figure 5.11 XRD patterns for samples after heat treatement at 900 ˚C prepared using [$ZrO^{2+}$] = 0.4 mol/L.

## 5.4 Conclusions

In this work, we studied the effects of different preparation parameters such as calcination temperature, precursor concentration, and precipitation pH in the bioinspired synthesis of mesoporous zirconia templated by the Pluronic-lysozyme conjugate. This is also the first report of the detailed preparation study of well-ordered mesoporous zirconia synthesized in completely aqueous media. The XRD studies showed that all samples precipitated as amorphous hydrated zirconium hydroxide and converted to tetragonal zirconia with heat treatment at temperatures as

low as 300 ˚C. Depending on the preparation conditions, tetragonal phase was retained up to 900 ˚C. The specific surface area progressively increased, reaching its maximum value for all samples at 500 ˚C, mostly due to the removal of the polymer template and dehydroxylation. The specific surface area decreased above 500 ˚C as a result of crystal growth and the collapse of mesopores. This study also showed that lower zirconium ion concentration will lead to smaller particle size as well as larger surface area, and more stable tetragonal phase. The largest surface area, 348 $m^2/g$, was obtained at pH=10 employing $[ZrO^{2+}]$ = 0.08 mol/L and 500 ˚C heat treatment. This study also indicated that the as synthesized mesoporous zirconia sample had larger surface area when precipitated in an alkaline medium than those precipitated in acidic or neutral medium. Thus the sample precipitated at pH=10 resulted in smaller crystal size which leads to a higher surface area, and also more stable tetragonal phase.

## Acknowledgments

This work was supported by the U.S. Department of Energy, Office of Basic Energy Science, Division of Materials Sciences and Engineering. The research was performed at the Ames Laboratory. Ames Laboratory is operated for the U.S. Department of Energy by Iowa State University under Contract No. DE-AC02-07CH11358.

## References

1. M. Rezaei, S. Alavi, S. Sahebdelfar, andZ. F. Yan, *Journal of Porous Materials,* 15, 171-79 **(2008)**.
2. M. M. A. Sekkina, *Journal of the Physical Society of Japan,* 54, 3012-17 **(1985)**.
3. M. Mamak, N. Coombs, andG. Ozin, *Journal of the American Chemical Society,* 122, 8932-39 **(2000)**.
4. T. Ishii and K. Kadoya, *Plant and soil,* 131, 53-58 **(1991)**.
5. S. Jaenicke, G. Chuah, V. Raju, andY. Nie, *Catalysis surveys from Asia,* 12, 153-69 **(2008)**.
6. A. De Aza, J. Chevalier, G. Fantozzi, M. Schehl, andR. Torrecillas, *Biomaterials,* 23, 937-45 **(2002)**.
7. S. Gulati, J. Hansson, J. Helfinstine, andC. Malarkey, *Tube Int.,* 4, 44-47 **(1985)**.

8. J. Wang, M. Valenzuela, J. Salmones, A. Vázquez, andX. Bokhimi, *Catalysis today,* 68, 21-30 **(2001)**.
9. D. Aguilar, L. Torres-Gonzalez, L. Torres-Martinez, T. Lopez, andP. Quintana, *Journal of Solid State Chemistry,* 158, 349-57 **(2001)**.
10. J. Y. Zheng, J. B. Pang, K. Y. Qiu, andY. Wei, *Microporous and mesoporous materials,* 49, 189-95 **(2001)**.
11. X. Ma, L. Klosterman, Y.-Y. Hu, X. Liu, K. Schmidt-Rohr, S. Mallapragada, andM. Akinc, *Journal of the American Ceramic Society,* 95, 3455-62 **(2012)**.
12. V. Bansal, D. Rautaray, A. Ahmad, andM. Sastry, *J. Mater. Chem.,* 14, 3303-05 **(2004)**.
13. K. Cassiers, T. Linssen, K. Aerts, P. Cool, O. Lebedev, G. Van Tendeloo, R. Van Grieken, andE. F. Vansant, *J. Mater. Chem.,* 13, 3033-39 **(2003)**.
14. G. Chuah, S. Jaenicke, andB. Pong, *Journal of Catalysis,* 175, 80-92 **(1998)**.
15. J. Y. Chane-Ching, F. Cobo, D. Aubert, H. G. Harvey, M. Airiau, andA. Corma, *Chemistry-A European Journal,* 11, 979-87 **(2005)**.
16. W. Stichert and F. Schüth, *Journal of Catalysis,* 174, 242-45 **(1998)**.
17. C. Su, J. Li, D. He, Z. Cheng, andQ. Zhu, *Applied Catalysis A: General,* 202, 81-89 **(2000)**.
18. H. Ogihara, M. Sadakane, Y. Nodasaka, andW. Ueda, *Chemistry of materials,* 18, 4981-83 **(2006)**.
19. C. Guo, P. Hu, L. Yu, andF. Yuan, *Materials Letters,* 63, 1013-15 **(2009)**.
20. S. Li, J. Zheng, W. Yang, andY. Zhao, *Materials Letters,* 61, 4784-86 **(2007)**.
21. M. Rezaei, S. Alavi, S. Sahebdelfar, andZ. F. Yan, *Powder technology,* 168, 59-63 **(2006)**.
22. J. Liang, Z. Deng, X. Jiang, F. Li, andY. Li, *Inorganic chemistry,* 41, 3602-04 **(2002)**.
23. M. Răileanu, L. Todan, D. Crişan, N. Drăgan, M. Crişan, C. Stan, C. Andronescu, M. Voicescu, B. Vasile, andA. Ianculescu, *Journal of Alloys and Compounds*, **(2011)**.
24. H. Eltejaei, J. Towfighi, H. R. Bozorgzadeh, M. R. Omidkhah, andA. Zamaniyan, *Materials Letters*, **(2011)**.
25. S. Shukla, S. Seal, R. Vij, andS. Bandyopadhyay, *Journal of Nanoparticle Research,* 4, 553-59 **(2002)**.
26. Y. Jiang, D. Yang, L. Zhang, Y. Zhang, J. Li, andZ. Jiang, *Industrial & Engineering Chemistry Research,* 47, 1876-82 **(2008)**.
27. X. Liu, Q. Ge, A. Rawal, G. Parada, K. Schmidt-Rohr, M. Akinc, andS. K. Mallapragada, *Science of Advanced Materials,* 5, 354-65 **(2013)**.
28. G. Chuah and S. Jaenicke, *Applied Catalysis A: General,* 163, 261-73 **(1997)**.
29. G. Stefanic, S. Popovic, andS. Music, *Thermochimica acta,* 303, 31-39 **(1997)**.
30. V. G. Deshmane and Y. G. Adewuyi, *Microporous and mesoporous materials,* 148, 88-100 **(2012)**.
31. W. Stichert and F. Schüth, *Chemistry of materials,* 10, 2020-26 **(1998)**.
32. U. K. H. Bangi, C.-S. Park, S. Baek, andH.-H. Park, *Powder Technology,* 239, 314-18 **(2013)**.

33. Y. Yusufoglu, Y. Hu, M. Kanapathipillai, M. Kramer, Y. E. Kalay, P. Thiyagarajan, M. Akinc, K. Schmidt-Rohr, andS. Mallapragada, *Journal of Materials Research*, 23, 3196-212 **(2008)**.
34. H. Chen, J. Gu, J. Shi, Z. Liu, J. Gao, M. Ruan, andD. Yan, *Advanced Materials*, 17, 2010-14 **(2005)**.
35. L. Gong, L.-B. Sun, Y.-H. Sun, T.-T. Li, andX.-Q. Liu, *The Journal of Physical Chemistry C*, 115, 11633-40 **(2011)**.
36. Q. Yuan, L. L. Li, S. L. Lu, H. H. Duan, Z. X. Li, Y. X. Zhu, andC. H. Yan, *The Journal of Physical Chemistry C*, 113, 4117-24 **(2009)**.
37. S. Kongwudthiti, P. Praserthdam, P. Silveston, andM. Inoue, *Ceramics international*, 29, 807-14 **(2003)**.
38. S. Shukla, S. Seal, R. Vij, S. Bandyopadhyay, andZ. Rahman, *Nano letters*, 2, 989-93 **(2002)**.
39. A. Sinhamahapatra, N. Sutradhar, M. Ghosh, H. C. Bajaj, andA. B. Panda, *Applied Catalysis A: General*, **(2011)**.
40. G. Chuah, S. Liu, S. Jaenicke, andJ. Li, *Microporous and mesoporous materials*, 39, 381-92 **(2001)**.
41. M. S. Wong, E. S. Jeng, andJ. Y. Ying, *Nano letters*, 1, 637-42 **(2001)**.
42. A. Clearfield, G. Serrette, andA. Khazi-Syed, *Catalysis today*, 20, 295-312 **(1994)**.
43. S. Ardizzone and C. Bianchi, *Journal of Electroanalytical Chemistry*, 465, 136-41 **(1999)**.
44. S. Milonjic and Z. Ilic, *Colloids and Surfaces*, 6, 167-74 **(1983)**.
45. G. A. Parks, *Chemical Reviews*, 65, 177-98 **(1965)**.
46. W. Russel, D. Saville, andW. Schowalter, *Colloidal dispersions*. in. Cambridge University Press (Cambridge and New York), (**1989)**.
47. J. Lyklema, *Fundamentals of interface and colloid science*, Vol. 5. Academic Pr, **(2005)**.
48. B. J. Kirby, *Micro-and Nanoscale Fluid Mechanics: Transport in Microfluidic Devices*. Cambridge Univ Pr, **(2010)**.
49. R. J. Hunter, *Foundations of colloid science*. Clarendon Press, **(1989)**.

# Chapter 6 Self-Assembly and Biphasic Iron-Binding Characteristics of Mms6, A Bacterial Protein That Promotes the Formation of Superparamagnetic Magnetite Nanoparticles of Uniform Size and Shape

Lijun Wang, Tanya Prozorov, Pierre E. Palo, Xunpei Liu, Ruslan Prozorov, Surya Mallapragada, and Marit Nilsen-Hamilton*

This chapter is modified from two papers published in *Biomacromolecules,* 2012, 13 (1), 98–105 and in *International Journal of Molecular Science*, 2013, 14, 14594-14606. My contribution to this work focused on characterization of the Mms6 protein by TEM and AFM, optimization of the synthesis conditions for Mms6 mediated magnetite nanoparticles, synthesis of the magnetite nanoparticles in the presence of Mms6 and its mutants under the optimized conditions, and characterization of some of the magnetite nanoparticles by TEM.

## Abstract

Living organisms create highly ordered mineralized structures from nano- to macro-scale. Proteins have been found responsible for forming many of these structures, but their function mechanisms are generally poorly understood. To better understand its role in biomineralization, the magnetotactic bacterial protein, Mms6, which promotes the *in vitro* formation of superparamagnetic magnetite nanoparticles of uniform size and shape, was studied for its structure and function. We visualized the spherical micelles formed by the protein in aqueous solution by TEM and AFM. We optimized the Mms6 concentration used for *in vitro* magnetite nanoparticle synthesis. Mms6 is shown to have two phases of iron binding: one high affinity and stoichiometric and the other low affinity, high capacity, and cooperative with respect to iron. The protein is amphipathic with a hydrophobic N-terminal domain and hydrophilic C-terminal domain. It self-assembles to form a micelle, with most particles consisting of 20–40 monomers. Proteins

with mutated C-terminal domains lost the function of forming superparamagnetic magnetite nanoparticles, showing that the function of Mms6 is sensitive to the arrangement of carboxyl/hydroxyl groups in the C-terminal.

## 6.1 Introduction

Magnetotactic bacteria can move under the direction of the local geomagnetic field due to their ability to generate magnetite nanoparticles.[1] The morphologies of the magnetite crystals are highly depending on the bacterial species or strains, indicating that the formation of magnetite nanoparticles by magnetotactic bacteria is under precise biological control.[2] Although the mechanisms that controlled the formation of nano-sized magnetite crystals with different morphologies are not well understood yet, there are evidences showing that proteins may involve in the controlled biomineralization process. Several low molecular mass proteins, Mms5, Mms6, Mms7, and Mms13, which were tightly bound to bacterial magnetite, were obtained from *Magnetospirillum magneticumstrain AMB-1*.[3] These proteins have similar properties. They contain hydrophobic N-terminal and hydrophilic C-terminal regions, and the C-terminal regions contain dense carboxyl and hydroxyl groups, which could bind irons.[4]

Magnetic nanoparticles with size ~50 nm are widely used in the development of medical and diagnostic applications such as magnetic resonance imaging (MRI), cell separation, biosensing, hyperthermia, and site-specific chemotherapy.[5–10] The synthesis of magnetic nanoparticles with narrow size distribution represents a significant practical and fundamental challenge.[11] Procedures for the controlled formation of uniformly sized particles at the nanometer scale have been developed, such as the thermal decomposition method. However, these methods require the use of organic solvents or extremely high temperatures.[12,13] Therefore, alternative processes for the simple formation of size and shape selective magnetic nanocrystals in aqueous media and low temperature are required.

In this paper, we studied the structure of Mms6 and its iron binding property. Magnetite nanoparticles similar to those in Nature were prepared by co-precipitation method in the presence of the protein Mms6. We also optimized the concentration of Mms6 used in the *in vitro* synthesis, based on more knowledge we learn about this protein. Two C-terminal mutants of this protein, m2Mms6 and m3Mms6, were synthesized and also used as templates to synthesis magnetite nanoparticles.

## 6.2 Experimental section

**Materials.** The mature form of Mms6 and two mutants (m2Mms6 and m3Mms6) were expressed and purified with N-terminal poly-histidine tags. The C-terminal sequences of these proteins are Mms6 (KSRDIESAQSDEEVELRDALA), m2Mms6 with -OH and -COOH side chains shuffled (KDR**S**I**D****E**AQ**ES**D**S**VELR**E**ALA) and m3Mms6 with all 21 C-terminal residues in the C-terminal domain scrambled (QSLERAEDEDADISAVEKLSR). The remaining sequences of these proteins are identical.

**Size exclusion chromatography.** Chromatography was performed at 4℃ in an AKTA FPLC system (GE healthcare) through prepacked Superose 12 10/300GL and Superdex Peptide 10/300GL columns. Flow rates were 0.4-0.5 mL/min. All column samples were prepared by centrifugation at 14,000g at 4℃ for 1h before use.

**$^{55}Fe^{3+}$ binding assays.** Mms6 (100 nM or 1 μM) in 100 mM KCl was incubated with $^{55}Fe$ (PerkinElmer) as ferric chloride (pH 3) or ferric citrate (pH 7.5) for 2h at 25℃. The samples were captured on nitrocellulose filters, washed and the $^{55}Fe$ quantified.

**Dynamic light scattering (DLS).** Mms6 (0.5 mg/ml) in 100 μL of 137 mM NaCl, 2.7 mM KCl, 4.3 mM $Na_2HPO_4$, 1.4 mM $KH_2PO_4$, pH 7.2 at 25℃ was analyzed with a Zetasizer Nano-

particle analyzer (Model: ZEN3690, Malvern Instrument Ltd., Southborough, MA). Each measurement consisted of 11 acquisitions of 10 s with 3 repeats. Data were processed by using Dispersion Technology Software 5.00 (Malvern Instrument Ltd). The buffer was filtered through a 0.45 μm nitrocellulose membrane and the protein samples were centrifuged for 1h (14000 x g, 4 ℃) prior to use

**Atomic Force Microscope (AFM).** Mms6(A133C) or Mms6(A131C) on a flat gold surface was scanned using AFM to explore the morphology of the protein on surface. Briefly, template-stripped gold served as the substrate, which was prepared by resistively evaporating 250 nm of gold onto a 4-in. silicon wafer with an Edwards 306A resistive evaporator. Glass microscope slides were cut into 1 × 1 cm squares and sonicated in diluted 5% Contrad 70, deionized water, and ethanol (twice), each for 30 min, and dried under a nitrogen stream. The clean glass chips were glued to the gold-coated wafer with two-part Epotek 377 (Epoxy Technology, Billerica, MA, USA) and heated at 150 ℃ for 1.75 h. The glass chips were then gently detached from the silicon wafer. The sandwiched gold film remained on the topside of the glass chip to yield a smooth gold surface. Three μL of 0.2 mg/mL Mms6(A133C) or Mms6(A131C) in buffer BC100 (20 mM Tris, 100 mM KCl, pH 7.5) was dropped on the gold substrate and incubated overnight at room temperature in a humid chamber created by a water-moistened filter in a sealed petri dish. The surface was then washed twice with BC100, 0.5% Tween 20 followed by two washes with 0.5% Tween 20 then dried under a nitrogen stream. AFM images were acquired using a Nanoscope III Digital Instruments/Veeco (Santa Barbara, CA, USA) in tapping mode. The diameter and length of the micelles on the reported image were obtained by measuring ~100 randomly chosen micelles.

**Magnetite nanoparticle formation.** Magnetite nanoparticles were synthesized by co-precipitation of $FeCl_2$ and $FeCl_3$ from aqueous solutions in the presence of Mms6 or its mutants.

Pluronic F127 polymeric aqueous gel was introduced into the synthesis, in order to slow the diffusion rates of the reagents to better mimic the conditions under which magnetite nanocrystals are formed in magnetotactic bacteria. Pluronic F127 aqueous solutions exhibit reverse temperature gelation, thus forming viscous gels at room temperature.

In a typical synthesis, 100 μL of 25wt% Pluronic F127 solution and 100 μL protein solutions containing 20 μg of  of Mms6, m2Mms6, or m3Mms6 were added to a 5 mL degassed pear-shape flask. The flask was then degassed, filled with argon and incubated at 4 ℃ for 30 min for the protein and Pluronic to mix. Then, the flask was degassed, added 50 μL of 0.5M FeCl3 and 50 μL of 0.25M FeCl2, and filled with argon. The flask was then incubated at 4 ℃ again for mixing. The resulting solution was then brought to room temperature, and titrated slowly with the room-temperature 1400 μL of 0.1 M NaOH solution under constant argon flow. As the titration progressed, there was a black particle layer formed on the top of the solution. Nanoparticles were allowed to grow and precipitate at room temperature in the argon purged and sealed flask for 5 days, after which the precipitated nanoparticles were washed with degassed water three times before characterization.

We also varied the concentration of the protein solution used in the synthesis (volume did not change), to test the protein concentration effect on the synthesis process.

**Transmission electron microscopy (TEM) characterization.** Mms6 protein and magnetite nanoparticles were visualized with a Tecnai G2 F20 Scanning Transmission Electron Microscope (FEI Company, Hillsboro OR) at operating voltage 200 KV. Proteins were examined by transmission electron microscopy with negative staining achieved by using the single droplet procedure. Briefly, 10 μL of 0.2 mg/mL protein in 2 mM Tris-HCl (pH 7.5) were individually applied to carbon coated 200 mesh copper grids. After 3 min most of the protein solution was

wicked off with a filter paper and the spot covered by a droplet of fresh 2% uranyl acetate. Excess uranyl actate was removed after 30 s and the grids were air-dried at room temperature. To prepare TEM samples of magnetite nanoparticles, ten microliters of thoroughly washed concentrated suspension of magnetite nanoparticles were dispersed in 3 mL of $H_2O$. Twenty microliters of diluted nanoparticle suspension prepared in this manner, were deposited on a holey carbon-coated copper grid and dried at room temperature under partial argon flow.

**Magnetization measurements** were carried out by using a Quantum Design SQUID (Superconducting Quantum Interference Device) 5T MPMS (Magnetic Properties Measurement System). Under moderate argon flow, 30 μL of concentrated, washed nanoparticle suspension were injected into a double walled polycarbonate capsule. The samples were cooled in a zero applied field to 5K. A negative magnetic field of 5T was applied to ensure complete remagnetization of all nanocrystals and then reversed to 500 Oe to ensure complete magnetization reversal in each particle and to remove metastable states.

## 6.3 Results and Analysis

### 6.3.1 Two Distinct Phases of Iron Binding by Mms6

The concentration dependence of $Fe^{3+}$ binding to Mms6 was determined at pH 3. Under these conditions, two distinct phases of iron binding by Mms6 were observed (Figure 6.1). Scatchard plots of the data constituting the first high affinity phase revealed stoichiometric binding ($Fe^{3+}$/Mms6 = 1:1). A $K_d^{app}$ of 0.58 ± 0.03 μM was measured. A similar value of 0.43 ± 0.11 μM with a stoichiometry of 1.2 ± 0.2 was determined by isothermal titration calorimetry from an average of three experiments at pH 3.[14] At pH 7.5, the $K_d$ was measured to be $10^{-16}$ M.[14] Thus, the $K_d$ for high affinity binding affinity of iron is significantly lower at pH 3 than pH 7. This result suggests a conformational difference under the two conditions, for which evidence was obtained by Circular Dichroism (CD) spectroscopy.

The second binding phase has a much lower apparent affinity ($K_d^{app}$ = 6 ± 4 μM) with an average of 19 ± 8 irons per Mms6. The m2Mms6 (shuffled C-terminal −OH and −COOH groups) and m3Mms6 (scrambled C-terminal sequence) were also tested for iron-binding under the same conditions as for Mms6. Both had lower affinities for iron than Mms6 and did not exhibit two phases of iron binding although m3Mms6 displayed low affinity and saturable iron binding (Figure 6.1). By contrast, the linear increase in binding by m2Mms6 at higher $Fe^{3+}$ concentrations appears to be nonspecific.

We speculate that both iron-binding phases are likely to be relevant to iron oxide crystal formation. The high affinity stoichiometric binding may contribute to the C-terminal domain adopting an appropriate conformation, whereas the second low affinity iron binding phase in which iron clusters on the protein cooperatively and at high stoichiometry is expected to be involved in crystal building.

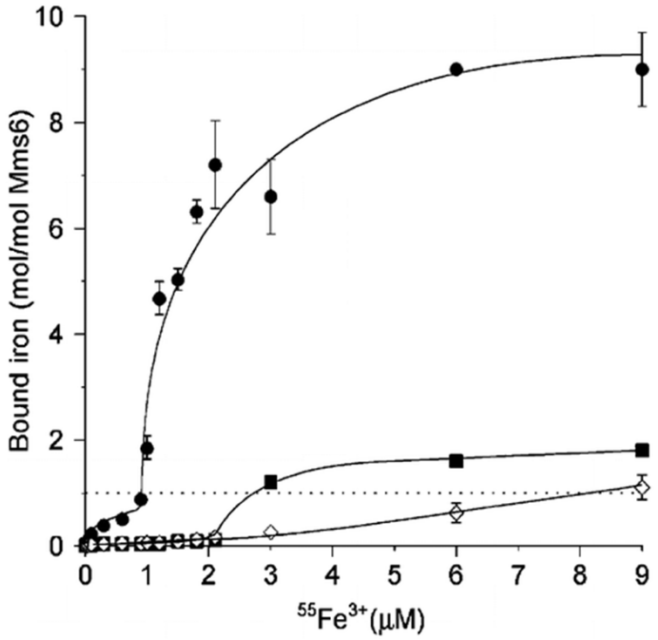


Figure 6.1 Two phases of iron binding by Mms6. Binding of Mms6 to free ferric iron was measured using $^{55}FeCl_3$ with the filter assay. The reaction mixtures contained 100 nM Mms6 (●),

m2Mms6 (◊), or m3Mms6 (■) in 20 mM Tris-HCl, 100 mM KCl, pH 3. Incubation was for 2 h at 25 ℃ followed by collection and analysis by the filter assay. All data are the average of duplicate values. Error bars represent the standard deviations.

The apparent molecular mass of Mms6 was determined by size exclusion chromatography, analytical ultracentrifugation, and DLS (Figure 6.2 A–C). These studies showed that Mms6 exists as large complexes at pH 3 and 7.5. The monomeric molecular mass of Mms6 is 10.2 kDa, but the peak of Mms6 passed through a Superose 12 column with the void volume, which suggests an apparent molecular mass of equal or greater than 300 kDa. Similar results were found at pH 7.5 and 3 in the presence or absence of $FeCl_3$. The observed sedimentation coefficients, distributed from 20 to 100S with the majority between 20 and 40S, also indicate that Mms6 forms large multimers with an estimated apparent molecular mass between 200 and 400 kDa. DLS measurement of Mms6 showed two particle sizes between which the protein mass is almost equally distributed. Peak 1 was 59% of the mass containing particles of 5.1 ± 1.5 nm radius with an estimated molecular mass of 200 kDa. Peak 2 was 41% of the protein mass and contained particles of 12 ± 6.5 nm radius and an estimated molecular mass of 2000 kDa. Although these latter particles contained a significant portion of the mass, they only represent 6% of all particles. Thus, the results of size exclusion chromatography, analytical ultracentrifugation and DLS studies show that Mms6 forms large multimers with most of the particles containing 20–40 protein molecules. In their entirety, these results provide strong evidence that Mms6 forms a micellar quaternary structure with 20 -40 single protein units.

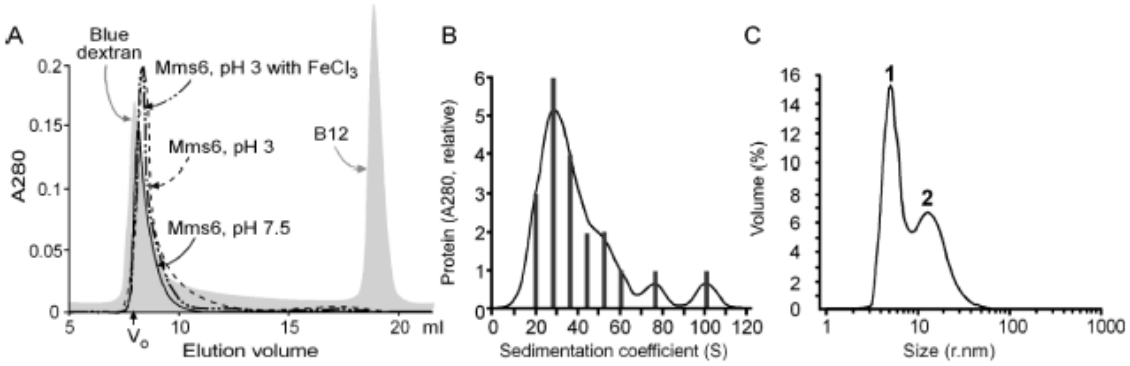


Figure 6.2 Mms6 self-assembles as micelles. Mms6 assembles into large multimers as shown by the following: (A) Size exclusion chromatography of Mms6 at pH 7.5 (solid line) or pH 3 in the presence or absence of 2 mM $FeCl_3$ (dashed lines). Blue Dextran and vitamin B12 were chromophores included to indicate the positions of the void and salt volumes respectively. (B) The sedimentation velocity profile of Mms6. (C) Dynamic light scattering.

### 6.3.2 Visualization of the Self-Assembled Mms6

We visualized the assembled structure of Mms6 by transmission electron microscopy (TEM) using negative staining and atomic force microscopy (AFM) combined with surface immobilization (Figure 6.3). For this latter approach we used a mutant Mms6(A133C) in which the terminal Ala was replaced with Cys by which the protein was attached to the gold surface. We could clearly see from the TEM images that each protein assembly is different from the others. Whereas the wild-type Mms6 appeared as spherical aggregates of a variety of sizes (Figure 6.3B), the Mms6-A131C appeared as a lattice of protein (Figure 6.3C,G) and Mms6-A133C appeared as a combination of worm-like structures and spheres (Figure 6.3D–F). The possibility that the replaced cysteine might form inter-protein disulfide linkages was shown unlikely because the same images were obtained when 20 mM β-mercaptoethanol was included with each protein. The AFM images gave similar interpretations of the assembled structures of the two mutant proteins (Figure 6.3E–H). By TEM, we obtained the diameters of the wild-type protein spheres, which

were 21 nm. This measured diameter is of interest with respect to the size of magnetite particle formed in vitro by Mms6, which is reported as ~30 nm in diameter.

The diameters of the Mms6(A133C) spheres were also measured by TEM and AFM as 27 and 39 nm respectively. Although apparently slightly larger, the difference between the Mms6 and Mms6(A133C) micelles was not significant as the coefficients of variation for these measurements (N > 80) were 14% and 18% for TEM and AFM respectively. Finally, dimensions of the Mms6(A133C) worms and the Mms6(A131C) lattice pieces were found to be the same by TEM and AFM, with the measurements being 15 × 92 nm and 16 × 86 nm respectively. Careful examination of the TEM images of Mms6 showed a number of very small particles, which had dimensions the same (14 nm) as the lattice and worm structures of the two A to C mutants.

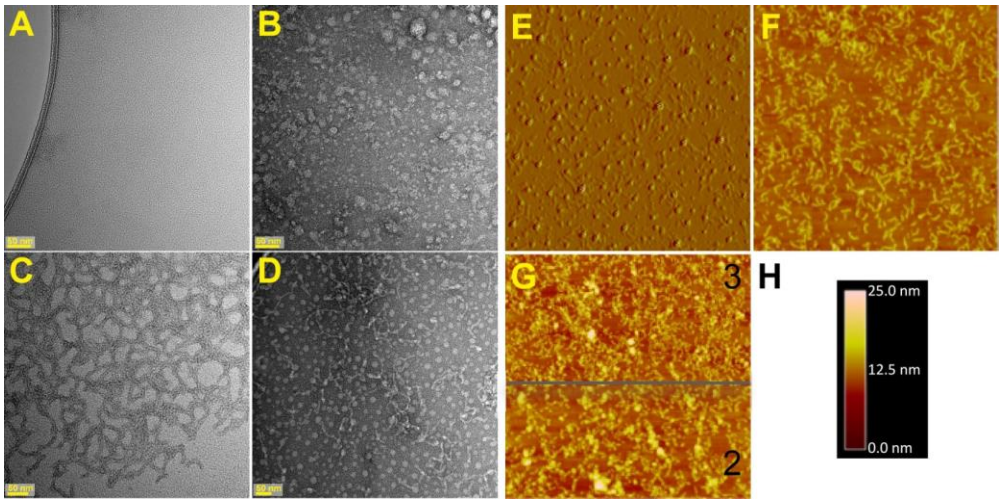


Figure 6.3 Mms6 and mutants visualized by atomic force microscopy (AFM) and transmission electron microscopy (TEM). (A–D) Negatively stained samples at 50 nm resolution of (A) Buffer, (B) Mms6, (C) Mms6(A131C), and (D) Mms6(A133C) were imaged by TEM; (E–H) AFM images of proteins immobilized on gold surfaces by a C-terminal cysteine; (E) Mms6 (A133C) amplitude image, scan area 5 μm × 5 μm, (F) Mms6 (A133C) height image, scan area 5 μm × 5 μm, and (G) Mms6(A131C) height image

with two maximum scale settings (3 μm above and 2 μm below the gray line); (H) Scale relevant to AFM height images in (F) and (G).

### 6.3.2 Optimization of *in vitro* magnetite synthesis with Mms6

Mms6 could form micelles, bind irons, and may have conformational change after iron binding, we believe that these properties will help it promote the bioinspired synthesis of magnetite *in vitro*. Since the mechanism by which Mms6 promote the formation of magnetite in the magnetotactic bacteria is not well understood, we tried different Mms6 concentration in the *in vitro* magnetite nanoparticles synthesis. The TEM results of the magnetite nanoparticles synthesized with different concentration of Mms6 are shown by Figure 6.4. Each image was selected by the criteria of closest to the average of the sample. Under our synthesis condition, the magnetite nanoparticles grown without Mms6 were less than 10 nm in diameter. The presence of Mms6 clearly increased the nanoparticles size. It is shown that as the Mms6 concentration increasing, the particles sizes increased slightly. The magnetite particle edges are clear and clean with the presence of Mms6, which is similar to that in Nature. These observations further confirmed the function of Mms6, and indicating its involvement in the Nature biomineralization process of magnetite.

To better understand the TEM results and get average data on the nanoparticles, we did a bulk materials magnetic measurement study. A ferromagnetic particle becomes "superparamagnetic" below a critical size of the order of 100 nm, depending on the material.[11] Its magnetization becomes thermally fluctuated. When the time between two magnetization fluctuations (Néel relaxation time) is shorter than the time used to measure the magnetization of the nanoparticles, without external magnetic field the magnetization appears to be average zero for the nanoparticles, which is superparamagnetism.[15] Usually, the time used to measure the magnetization is not changing, while the temperature is changing. The blocking phenomenon (and its characteristic

"blocking" temperature, $T_B$) is a signature of the superparamagnetic nanoparticle that depends on the particle size, degree of crystallinity, and interparticle interactions.[11] Below $T_B$, nanoparticles are "blocked", which means that initially random magnetic moments of individual nanoparticles cannot readily align with the applied field. Above $T_B$, the particles fluctuates fast, so the fluctuation time is shorter than the measurement time, thus, shows superparamagnetic property.[15] Experimentally, $T_B$ is marked by the peak in the M(T) curve measured upon warming after a magnetic field was applied at a low temperature to a zero-field-cooled sample (so called ZFC-W procedure). From Figure 6.5, we can see that the magnetite with 20 μg magnetite had the closest behavior to superparamagnetic nanoparticle, qualitatively. The Blocking temperature of each sample is shown by the inserted box in Figure 6.5. A cooperative curve between the blocking temperature and the Mms6 concentration is shown by Figure 6.6. The blocking temperature was increasing as the Mms6 concentration increased, except the one with 20 μg Mms6, which is also the one had the closest superparamagnetic properties. To ensure that the *in vitro* synthesized nanoparticles has larger size and are superparamagnetic, we chose to use 20 μg protein in all the following synthesis of magnetite nanoparticles.

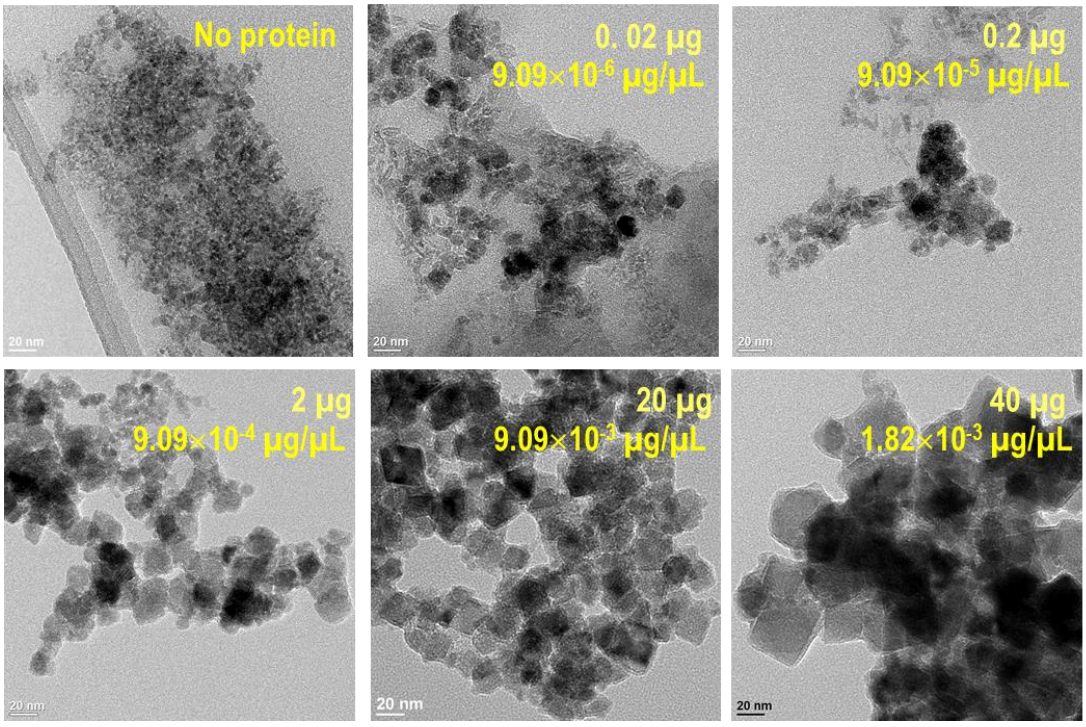


Figure 6.4 TEM images of magnetite nanoparitcles synthesized by co- precipitation method with difference Mms6 concentrations. The total Mms6 amount used in each sample and its concentration is labeled on the image.

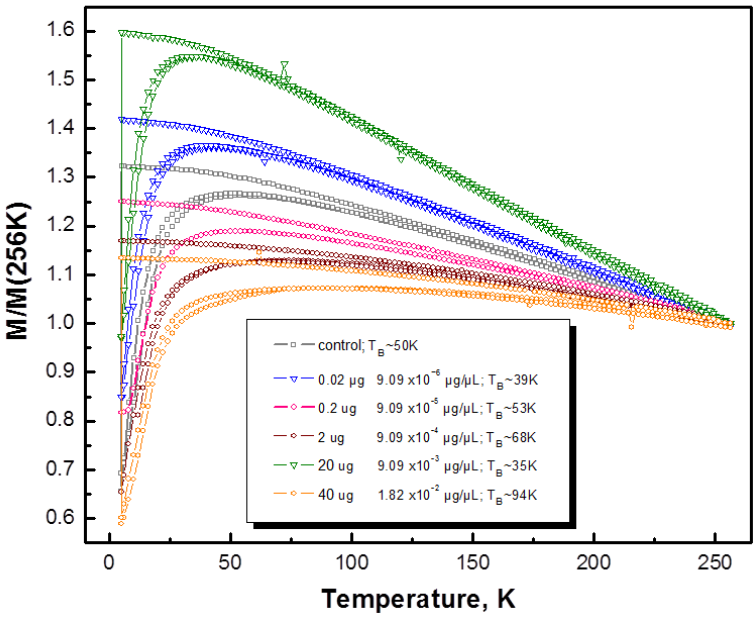


Figure 6.5 Temperature-dependencies of magnetization of the magnetite nanocrystals grown with different amount of Mms6. The blocking temperature for each sample is listed in the inserted box.

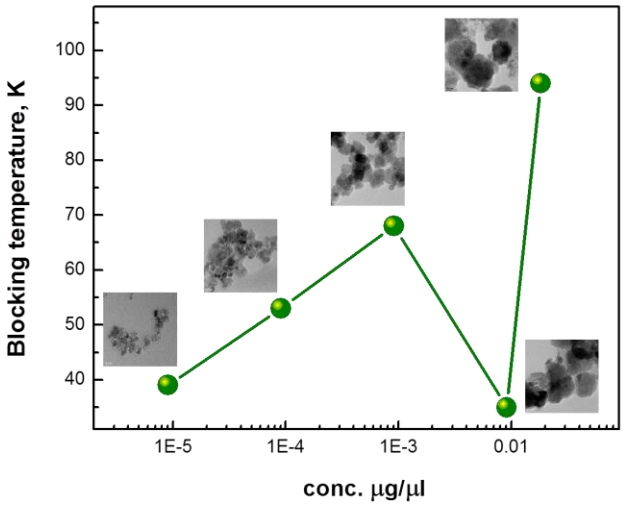


Figure 6.6 The cooperation curve between blocking temperature of the magnetite nanoparticles and Mms6 concentrations.

### 6.3.3 Formation of Magnetic Crystals of Uniform Size and Shape Is Associated with a Defined Arrangement of Carboxyl and Hydroxyl Groups in the C-Terminal Domain of Mms6

Mms6 and the two mutant proteins, m2Mms6 and m3Mms6, were used in the synthesis of magnetite nanoparticle, using the optimized condition. The particles formed were gathered and examined by TEM for morphology and size and by the zero field cooled (ZFC-W) procedure to measure magnetic characteristics. The sizes and shapes of the magnetite nanocrystals grown in the presence of Mms6, m2Mms6, m3Mms6, or no-protein were different, with only the Mms6-grown crystals being large, with evidence of a crystalline lattice (Figure 6.7). Nanoparticles grown with Mms6 showed an elevated blocking temperature ($T_B$), whereas particles grown in the presence of m2Mms6 showed the same profile as samples that contained no protein (Figure 6.7). The Mms6-templated magnetite nanocrystals exhibited the behavior closest to that expected of superparamagnetic magnetite particles. These results suggest that structure of the C-terminal domain is important for stability of the protein function. The mutants cannot promote the formation of magnetite nanoparticles as good as the wild type Mms6, which indicate the C-terminal, or the carboxyl and hydroxyl groups at C-terminal is very important for the function of Mms6.

## 6.4 Conclusions

In conclusion, we investigated the quaternary structure and function of Mms6, a biomineralization protein with 59 amino acids that can promote the formation of magnetite nanoparticles *in vitro*. We demonstrated that Mms6 forms a unique micellar quaternary structure *in vitro* that may provide a surface for magnetite crystal formation. We also quantitatively determined the binding profile of Mms6 with ferric iron and demonstrate that Mms6 has two phases of iron binding, the first is stoichiometric and very high affinity and the second is low affinity, high capacity, and cooperative with respect to iron. We optimized the Mms6 amount for

the *in vitro* synthesis of 30-50 nm magnetite nanoparticles with superparamagnetic properties. We also identified the C-terminal domain of Mms6 to be the functional domain. Taken together, these in vitro studies provide valuable insight toward understanding the mechanism of magnetite nanoparticle formation promoted by Mms6.

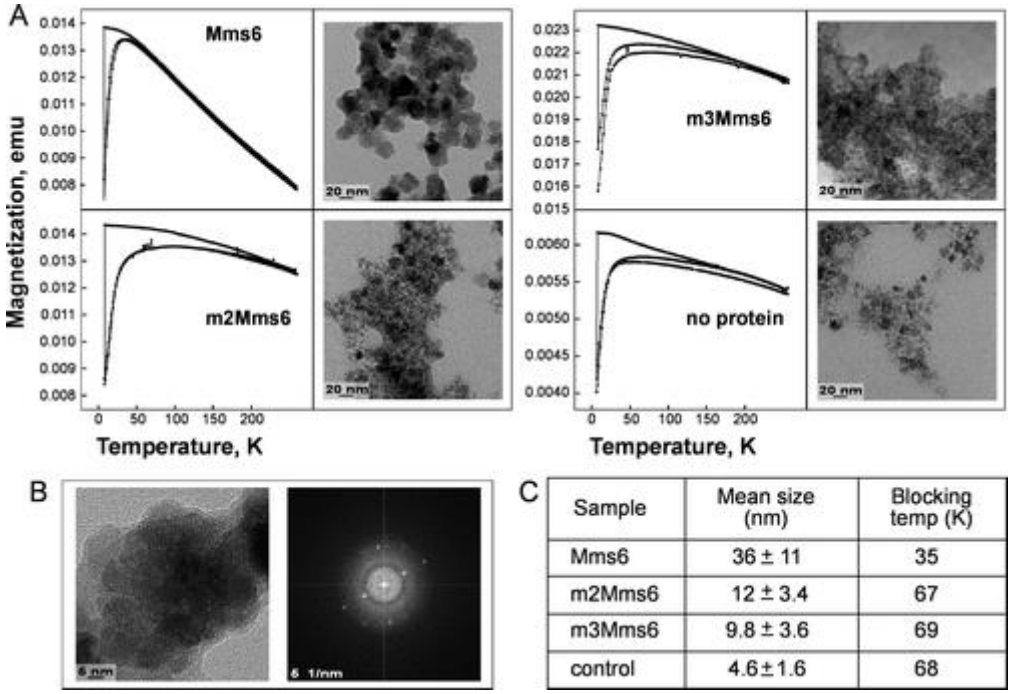


| Sample | Mean size (nm) | Blocking temp (K) |
|---|---|---|
| Mms6 | 36 ± 11 | 35 |
| m2Mms6 | 12 ± 3.4 | 67 |
| m3Mms6 | 9.8 ± 3.6 | 69 |
| control | 4.6 ± 1.6 | 68 |

Figure 6.7 Mms6 promotes the formation of superparamagnetic nanoparticles of uniform size and shape. (A) Temperature-dependencies of magnetization of the magnetite nanocrystals grown in the presence of Mms6, m2Mms6, m3Mms6, or no-protein and TEM images showing their sizes and shapes. (B) Image of magnetite nanocrystals formed in the presence of Mms6 taken at 360000-fold magnification, along with the Fast Fourier Transform that reveals the presence of a crystalline lattice. (C) Mean sizes and blocking temperatures of the particles shown in A. The analysis of magnetite crystal size was performed on numerous micrographs (total > 1000 particles measured) obtained in the bright field mode. Shown are the mean values and the standard deviation of the mean.

## Acknowledgements

This work was supported by the U.S. Department of Energy, Office of Basic Energy Science, Division of Materials Sciences and Engineering. The research was performed at the Ames Laboratory. Ames Laboratory is operated for the U.S. Department of Energy by Iowa State University under Contract No. DE-AC02-07CH11358.

## References

(1) Bazylinski, D. A.; Frankel, R. B. Magnetosome formation in prokaryotes. *Nat Rev Micro* **2004**, *2*, 217–230.

(2) Tanaka, M.; Mazuyama, E.; Arakaki, A.; Matsunaga, T. MMS6 Protein Regulates Crystal Morphology during Nano-sized Magnetite Biomineralization in Vivo. *J. Biol. Chem* **2011**, *286*, 6386–6392.

(3) Arakaki, A.; Webb, J.; Matsunaga, T. A Novel Protein Tightly Bound to Bacterial Magnetic Particles in Magnetospirillum magneticum Strain AMB-1. *Journal of Biological Chemistry* **2003**, *278*, 8745 –8750.

(4) Prozorov, T.; Mallapragada, S. K.; Narasimhan, B.; Wang, L.; Palo, P.; Nilsen-Hamilton, M.; Williams, T. J.; Bazylinski, D. A.; Prozorov, R.; Canfield, P. C. Protein-Mediated Synthesis of Uniform Superparamagnetic Magnetite Nanocrystals. *Adv. Funct. Mater.* **2007**, *17*, 951–957.

(5) Bulte, J. W. .; Cuyper, M. D. Magnetoliposomes as Contrast Agents. In *Liposomes, Part C*; Academic Press, 2003; Vol. Volume 373, pp. 175–198.

(6) Kuhara, M.; Takeyama, H.; Tanaka, T.; Matsunaga, T. Magnetic Cell Separation Using Antibody Binding with Protein A Expressed on Bacterial Magnetic Particles. *Anal. Chem.* **2004**, *76*, 6207–6213.

(7) Miltenyi, S.; Müller, W.; Weichel, W.; Radbruch, A. High gradient magnetic cell separation with MACS. *Cytometry* **1990**, *11*, 231–238.

(8) Pérez, J.; Ros, A. Properly embedded minimal annuli bounded by a convex curve. *Journal of the Institute of Mathematics of Jussieu* **2002**, *1*, 293–305.

(9) Kawai, N.; Ito, A.; Nakahara, Y.; Futakuchi, M.; Shirai, T.; Honda, H.; Kobayashi, T.; Kohri, K. Anticancer effect of hyperthermia on prostate cancer mediated by magnetite cationic liposomes and immune-response induction in transplanted syngeneic rats. *The Prostate* **2005**, *64*, 373–381.

(10) Babincová, M.; Čičmanec, P.; Altanerová, V.; Altaner, Č.; Babinec, P. AC-magnetic field controlled drug release from magnetoliposomes: design of a method for site-specific chemotherapy. *Bioelectrochemistry* **2002**, *55*, 17–19.

(11) Prozorov, T.; Palo, P.; Wang, L.; Nilsen-Hamilton, M.; Jones, D.; Orr, D.; Mallapragada, S. K.; Narasimhan, B.; Canfield, P. C.; Prozorov, R. Cobalt Ferrite Nanocrystals: Out-Performing Magnetotactic Bacteria. *ACS Nano* **2007**, *1*, 228–233.

(12) Casula, M. F.; Jun, Y.; Zaziski, D. J.; Chan, E. M.; Corrias, A.; Alivisatos, A. P. The Concept of Delayed Nucleation in Nanocrystal Growth Demonstrated for the Case of Iron Oxide Nanodisks. *J. Am. Chem. Soc.* **2006**, *128*, 1675–1682.

(13) Park, J.; An, K.; Hwang, Y.; Park, J.-G.; Noh, H.-J.; Kim, J.-Y.; Park, J.-H.; Hwang, N.-M.; Hyeon, T. Ultra-large-scale syntheses of monodisperse nanocrystals. *Nature Materials* **2004**, *3*, 891–895.

(14) Wang, L.; Prozorov, T.; Palo, P. E.; Liu, X.; Vaknin, D.; Prozorov, R.; Mallapragada, S.; Nilsen-Hamilton, M. Self-Assembly and Biphasic Iron-Binding Characteristics of Mms6, A Bacterial Protein That Promotes the Formation of Superparamagnetic Magnetite Nanoparticles of Uniform Size and Shape. *Biomacromolecules* **2011**, *13*, 98–105.

(15) Bean, C. P.; Livingston, J. D. Superparamagnetism. *Journal of Applied Physics* **1959**, *30*, S120–S129.

# Chapter 7 Iron-induced structural change of the biomineralization protein Mms6 in solution

Xunpei Liu, Honghu Zhang, Wenjie Wang*, Shuren Feng, David Vaknin, Mufit Akinc, Marit Nilsen-Hamilton, and Surya K. Mallapragada*

This chapter is modified from a paper to be submitted to *Biomacromolecules.* My contribution to this work includes experimental design, dynamic light scattering (DLS) measurements and analysis, transmission electron microscopy (TEM), and small angle X-ray scattering (SAXS) measurements. The SAXS analysis was done by our collaborator.

## Abstract

Magnetotactic bacteria produce magnetic nanocrystals with uniform shapes and sizes in Nature. The formation of such uniform magnetic nanocrystals under physiological conditions has inspired the use of the biomineralization protein Mms6 to promote the formation of uniform sized magnetite nanocrystals *in vitro*. To better understand the role of Mms6 in the nanocrystal formation *in vitro*, and to investigate the interactions between the protein and iron, we designed small angle X-ray scattering (SAXS) experiments to study the protein in the presence of iron. Dynamic light scattering (DLS) and transmission electron microscopy (TEM) were also used as complementary tools. By fitting and analyzing the SAXS data, it is found that before adding iron ions, the Mms6 protein exists as spherical micelles in solution with a diameter of around 10 nm. Adding iron ions to the Mms6 solution induced a structural change in the protein. Aggregates with sizes larger than 75 nm formed after adding iron ions to Mms6 solution, which were probably due to the self-assembly of protein and iron. This investigation provides direct evidence of interactions between Mms6 and iron. The change in the size and shape of the protein is also important for understanding the Mms6 mineralization mechanism *in vitro* and optimizing the synthesis conditions.

Key words: Mms6, SAXS, DLS, TEM, aggregates

## 7.1 Introduction

Many organisms in Nature have the capability of creating hierarchical inorganic structures that they use for a variety of purposes such as supporting, protection, and direction.[1] In this class of organisms, magnetotactic bacteria produce magnetic nanocrystals with uniform shapes and sizes to direct themselves to move under local geomagnetic field lines.[2] The formation of such uniform magnetic nanocrystals under physiological conditions has inspired researchers to develop bioinspired approaches involving biological macromolecules from magnetotactic bacteria for the *in vitro* room-temperature synthesis of many different magnetic nanomaterials.[2–5]

Mms6 is a biomineralization protein found associated with the magnetite nanocrystals inside the magnetosomes of *Magnetospirillum magneticum* AMB-1, and it has been shown to promote the formation of superparamagnetic magnetite nanocrystals under room temperature and mild conditions *in vitro*.[3] In fact, in addition to the formation of uniform magnetite nanocrystals *in vitro*, Mms6 has been found to promote the room temperature synthesis of other uniform magnetic nanocrystals such as cobalt ferrite in vitro.[4] This is particularly interesting, since cobalt ferrite nanocrystals do not occur in nature in magnetotactic bacteria or in other living organisms. Such magnetic nanoparticles have many applications, such as contrast agents in magnetic resonance imaging (MRI), high density data storage, drug targeting and delivery.[3] Therefore, many research efforts have been focused on synthesizing different kinds of magnetic materials *in vitro* in the presence of Mms6, and understanding the biomineralization mechanisms of Mms6. Tanaka et al proposed that Mms6 forms a scaffold in the magnetosome membrane that brings together proteins responsible for forming the magnetic particles *in vivo*.[6] Additional progress has been made recently in understanding the structure and properties of Mms6 *in vitro*. Mms6 is an amphiphilic protein with a hydrophobic N-terminal domain and a hydrophilic C-terminal domain.

The protein self-assembles into micelles in solution and the C-terminus can bind iron with very high affinity.[7]

However, the role of Mms6 in the formation of magnetic nanocrystals *in vitro* is still unknown, although the first successful synthesis of magnetite nanocrystals using Mms6 was reported a while ago.[3,8] It is very challenging to study the interactions between the protein and the iron precursor in solution without significantly impacting their state and composition. Most recently, due to the development of synchrotron sources, small angle X-ray scattering (SAXS) has attracted much interest because of its unique advantages in the study of comprehensive structural characterization of biological macromolecular complexes in solution.[9] It provides overall three-dimensional structures and allows to quantitatively characterize equilibrium mixtures or flexible systems.[10] Compared to other structural characterization techniques, SAXS can be performed near physiological conditions without damaging the samples, which is very critical to characterize biological samples.

In this study, we investigate the interactions of the Mms6 protein with iron precursors under the conditions involved in magnetite nanocrystal formation *in vitro*, and characterize the solution system using SAXS, and by dynamic light scattering (DLS) and transmission electron microscopy (TEM) as complementary characterization techniques. The hypothesis is that Mms6 micelles are mobile in solution, and in the presence of iron ions, Mms6 drives the fusion and formation of larger protein and iron islands that can eventually facilitate nanocrystal formation. Our results show that in the presence of iron ions, larger protein-iron aggregates formed, which is probably the reason why Mms6 promotes the formation of larger superparamagnetic magnetite nanocrystals *in vitro*. This study opens up a new perspective of understanding the biomineralization mechanism of Mms6 and is very crucial in being able to developing synthetic analogs of the Mms6 biomineralization protein.

## 7.2 Experimental Section

### 7.2.1 Solution sample preparation for SAXS and DLS

To investigate the interactions between Mms6 and iron ions in solution, we prepared two sets of samples with varying iron ion or with varying protein concentrations. For the samples with fixed iron ion concentrations but varying protein concentrations, the final $FeCl_3$ and $FeCl_2$ concentrations were maintained at 83 mM and 42 mM, respectively, while the final protein concentrations were either 0.067, 0.2, 0.33, or 0.67 mg/ml. For the samples with fixed protein concentration, which was set at 0.2 mg/ml, the iron ion concentrations were diluted 10, 100, and 1000 times compared to the other set of samples with fixed iron ion concentrations. All samples were in Tris buffer with 6.67 mM Tris and 33.33 mM KCl. The samples were stored under 4 ˚C, and brought up to room temperature for 2 hours before measurements.

### 7.2.2 SAXS measurements

SAXS measurements were conducted using synchrotron radiation at beamline 12ID-B, Advanced Photon Source (APS), Argonne National Laboratory. Sample solutions were loaded into a flow cell (capillary tube, 1 mm in diameter) that is vertically mounted and normal to the X-ray beam. During the X-ray exposure period, the solutions flowed up and down at a constant rate controlled by a Hamilton Microlab 600 diluter. Detector Pilatus 2m, pixel size 0.172 mm, X-ray energy 14.0 keV and sample-to-detector distance 2027.66 mm were used to collect the data. Exposure times were carefully chosen to avoid apparent radiation damage while still give good signal/noise ratio. The data was averaged from 20 single measurements for each sample. The two-dimensional (2D) data, after correction (normalization of incident beam intensity, background subtraction, and so forth), were integrated to a one-dimensional intensity function, I(q), where the scattering wave vector $q = 4 \pi \sin(\theta)/ \lambda$, $2\theta$ being the scattering angle and $\lambda$ being the X-ray wavelength.

### 7.2.3 DLS measurement

The size of the nanostructures in the solution were determined using quasi-elastic light scattering (Zetasizer Nano, Model: ZEN3690, Malvern Instruments Ltd.) with laser irradiation at 633 nm. These solutions were placed in cuvettes to measure the scattering. Each measurement consisted of 17 acquisitions of 10 s. The DTS (Nano) software was used to obtain the number percentages of different sized structures in each sample.

### 7.2.4 TEM imaging

To directly visualize the assembled structure of Mms6, proteins were examined by transmission electron microscopy (TEM) with negative staining achieved by using the single droplet procedure.[11] Because high iron concentrations result in TEM samples that are too thick too for electron transmission, a diluted $Fe^{3+}$: Mms6 molar ratio of 1:8 was used to observe any iron induced change in Mms6 using TEM. Briefly, 10 µL of 0.067, 0.2 or 0.67 mg/ml concentration protein samples in 2 mM Tris-HCl (pH 7.5) were individually applied to carbon coated 200 mesh copper grids. After 3 min, most of the protein solution was wicked off with a filter paper and the spot covered by a droplet of fresh 1% Sodium Silicotungstate (NaSiW). Excess NaSiW was removed after 30 s and the grids were air-dried at room temperature. TEM imaging was performed using a Tecnai G2 F20 Scanning Transmission Electron Microscope (STEM) (FEI Company) at an operating voltage of 200 kV. Multiple areas of each sample were examined. Measurements of structure sizes were determined by using Nano Measurer software from TEM images with at least 200 different micelles measured for each sample.

## 7.3 Results and analysis

### 7.3.1 DLS

DLS measurements (Figure 7.1) show that the filtered solution containing iron ions has a peak around 1 nm, which is consistent with the SAXS data. The three thinner dashed lines in Fig.1 stand for the Mms6 solution with different concentrations, 0.067, 0.2 and 0.67 mg/ml, and the corresponding average structure sizes are 12.5, 10.3, and 10.0 nm, respectively. Generally, the Mms6 micelles have an average diameter about 10 nm, and concentration has little impact on the micelles' size. These results are also consistent with the DLS data reported earlier, where the 0.5 mg/ml mms6 had average structure size of 10.2 nm.[2]

Adding iron ions to the Mms6 solution caused a significant size increase, as shown in Fig.1. The mixtures of Mms6 and iron ions with Mms6 concentrations of 0.067, 0.2 and 0.67 mg/mg have average nanoparticle sizes of 40.4, 76.1, and 86.2 nm, respectively. Iron ions caused the Mms6 micelles to self-assemble and form larger aggregates, which may help the magnetite formation mediated by Mms6 *in vitro*.[2] This shows that iron ions can introduce nanostructure changes of the protein in solution, and these changes occur prior to the addition of sodium hydroxide to grow magnetite nanocrystals *in vitro*. The formation of the larger Mms6/irons aggregates in solution also explains the reason for larger magnetite nanocrystals formed in the presence of Mms6.[2,3] We can see that for all the Mms6 concentrations, the size distribution gets larger up on addition of iron ions, which may be due to the high iron ions concentrations used, and may also be due to a single Mms6 protein cannot work as efficient as the protein complexes inside the magnetotactic bacteria.

Besides, the DLS results are very consistent with the SAXS data fitting indicating Mms6 micelles' sizes with or without iron ions. SAXS is a powerful tool to study the micelles that are less than 30 nm in solution, and DLS provides good supplementary data for larger size ranges.

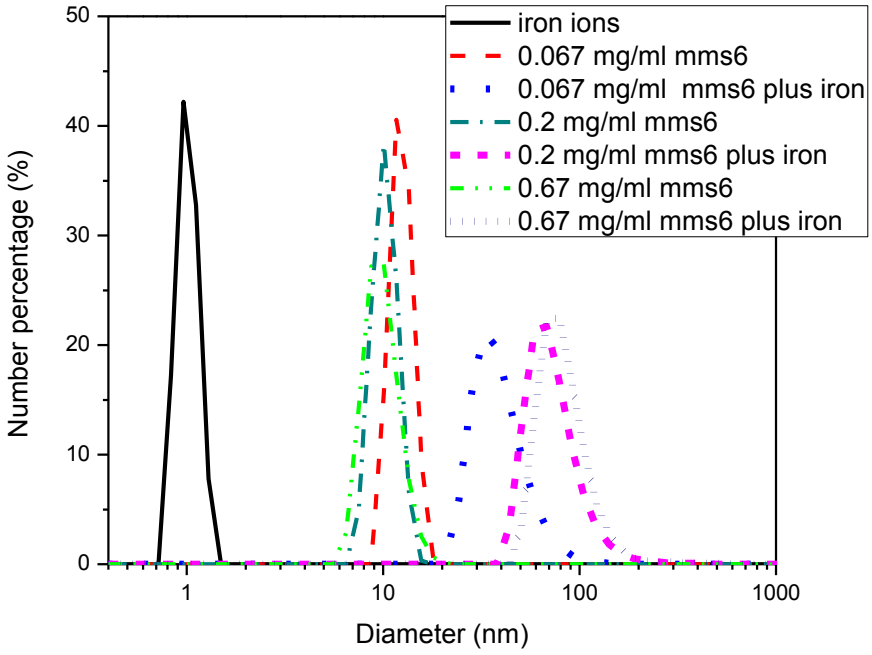


Figure 7.1 Dynamic light scattering measurements of iron ionss solution, different concentrations of Mms6 solutions and solution mixtures of iron and Mms6. For the samples with iron, the final $FeCl_3$ and $FeCl_2$ concentration are 83 mM and 42 mM, respectively.

### 7.3.2 TEM

Due to the limitation of TEM with respect to high iron ion concentrations, we used $Fe^{3+}$:Mms6 molar ratios of 1:8 in our TEM samples. We have reported earlier that only $Fe^{3+}$ binds Mms6, and has very high affinity.[2,12] This ratio was chosen because we have previously observed a structural change in Mms6 in the presence of iron ions at this ratio using Circular Dichroism spectroscopy.[7] Figure 2 shows the TEM images of Mms6 micelles in the presence and absence of iron ions for the highest (0.67 mg/ml) and lowest protein concentrations (0.067 mg/ml). The average micelles' sizes for Fig.2 A, B, C, and D are 13.4±3.1, 18.2±3.6, 13.1±3.5, and 26.3±9.5 nm, respectively.

The TEM results are very consistent with the DLS studies that show that the presence of the iron ions caused the micelles sizes to increase, although for the TEM studies, the increase was not as pronounced because of the much lower iron ion concentrations used; and the iron ions also caused a wider size distribution. The average sizes for the pure Mms6 protein suggested by DLS and TEM are also very close for each sample. The average sizes for the mixture of Mms6 and iron suggested by TEM is less than that suggested by DLS, which is due to the much lower iron concentration used for the TEM samples. Figures 7.2C and D have much higher micelle concentrations than Figures 7.2A and B, because of the higher Mms6 concentration. TEM provides a direct visualization of the micelles, and is a good complementary technique for the scattering experiments.

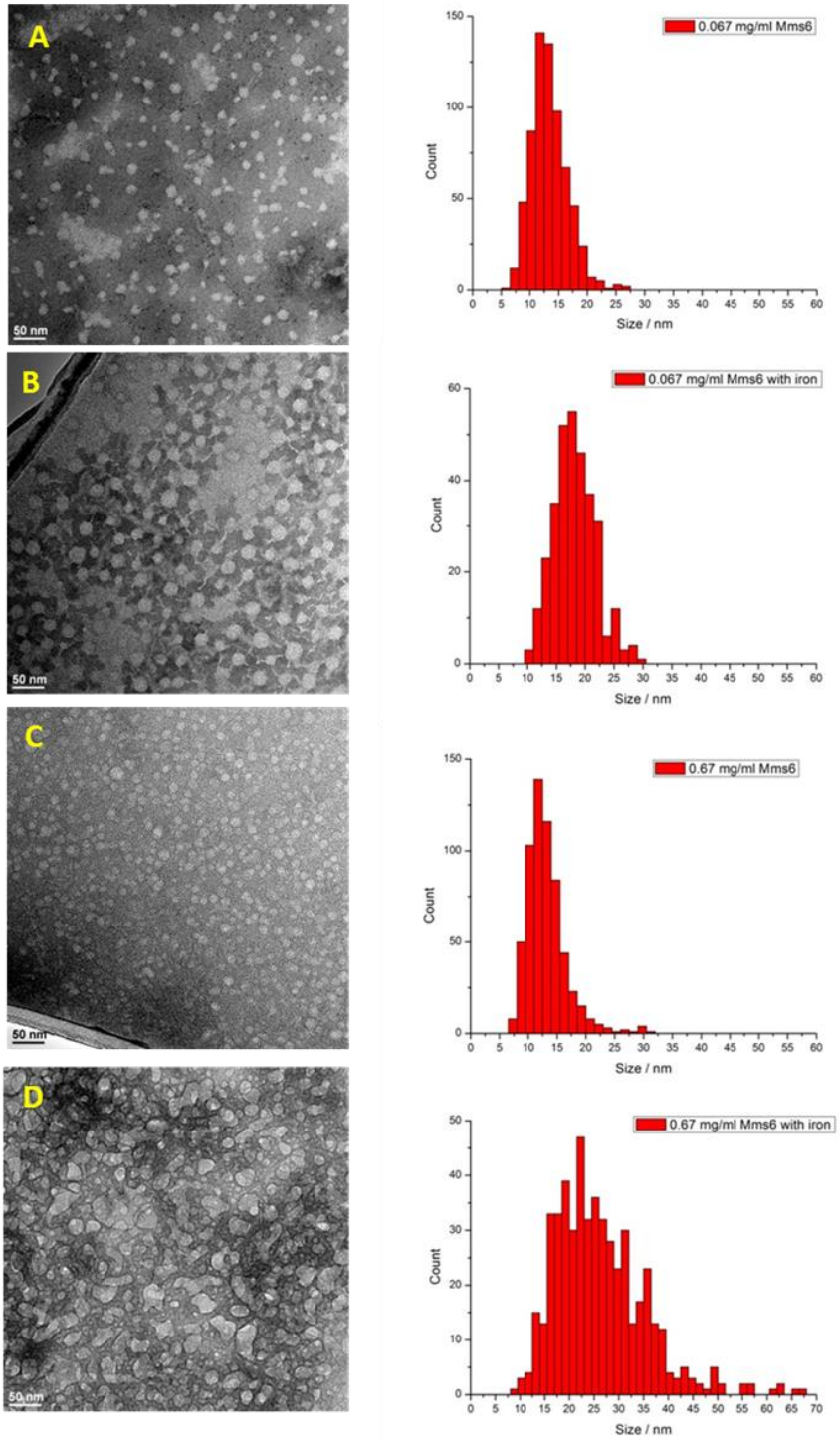
A
50 nm
0.067 mg/ml Mms6
Count
Size / nm
B
50 nm
0.067 mg/ml Mms6 with iron
Count
Size / nm
C
50 nm
0.67 mg/ml Mms6
Count
Size / nm
D
50 nm
0.67 mg/ml Mms6 with iron
Count
Size / nm

Figure 7.2 TEM images of A) 0.067 mg/ml Mms6; B) 0.067 mg/ml Mms6 with iron; C) 0.67 mg/ml Mms6; D) 0.67 mg/ml Mms6 with iron. The diameter size distribution is on the right of each image. The scale bar is 50 nm.

### 7.3.3 SAXS

SAXS data for Mms6 solution at three concentrations, 0.20, 0.33, and 0.67 mg/mL, are presented in Figure 3 (a). To estimate the size of the Mms6, the Mms6 micelles are assumed as spherical and uniform in scattering length density (SLD), and characterized with hypothetical radii distributions accounting for polydispersity. Figure 3 (b) presents a Gaussian distribution and Schultz distribution that can best-fit SAXS data in (a), suggesting the micelles' radii are $R \approx 51 \pm 11$ Å, which is almost identical to the diameter measured from dynamic light scattering.

The SAXS from the mixture of 83 mM $FeCl_3$ and 42 mM $FeCl_2$ (high iron ions concentration) solution is displayed in Figure 3(c) and is much lower than SAXS from Mms6 at intermediate-q range. Assuming there are no interactions between Mms6 and iron, the mixture of iron and Mms6 would be the sum of the SAXS from each. The sum of scattering from each component (iron and Mms6) is also shown in (c), comparing with the actual scattering obtained from the mixture. The data shows that the mixture of $Fe^{3+}$ /$Fe^{2+}$ and Mms6 enhance the SAXS within the measured q-range, as shown in Figure 3 (c), suggesting that interactions do occur upon mixing Mms6 and iron. The SAXS from the mixture features a power-law behavior within the intermediate q-window, where Guinier-law is valid for Mms6 in the absence of iron. We argue that if the probed SAXS still originates from Mms6, it would correspond to a much larger globular structure with its Guinier law region shifted to a much lower q-range thus out of current q-window.

Therefore, we propose that adding iron ions to the Mms6 solution introduced formation of aggregates in the solution, due to the protein and iron interaction0introduced self-assembly, and

the estimated lower limit of the aggregates diameter is 75 nm, assume the aggregates are close to spherical structure. This is quite close to the dynamic light scattering results.

Figure 3(d) shows the enhancement of SAXS intensity within current q-window as a function of iron concentration. With very dilute iron concentration (1/1000 dilution), there are already perceivable changes at low-q, indicating as a small bending up. At 1/100 dilution and 1/10 dilution, SAXS enhancements are clearly seen, which confirmed the protein-iron interaction.

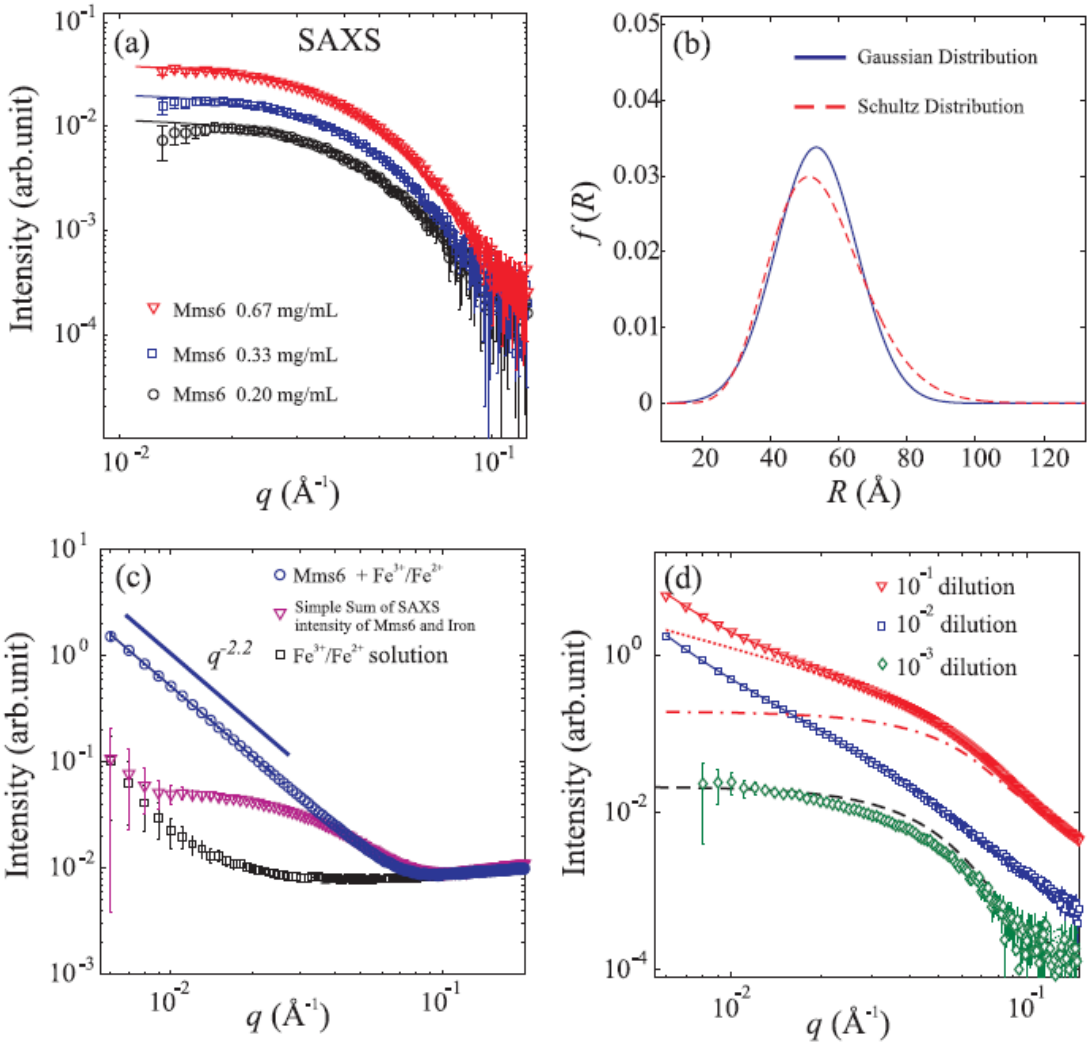

Figure 7.3 (a) SAXS data for solutions of Mms6 at concentration of 0.2, 0.33 and 0.67 mg/ml as indicated by symbols of circles, squares, and triangles, respectively. (b) Hypothetical radii distribution function *f* (R) that best fit the SAXS data in (a). (c) The SAXS data of an iron solution and its sum with that of Mms6 solution as a hypothetical intensity from their mixture if each of them scatters independently. The experimental intensity data from such a mixture manifest a power- law behavior. (d) SAXS data of Mms6 solutions at 0.2 mg/ml with different amount of iron ions. The initial $FeCl_3$ and $FeCl_2$ concentration were maintained at 83 mM and 42 mM, respectively, and diluted 10, 100, and 1000 times. The dashed-line represents the SAXS data in the absence of iron. Solid lines are the best fit. Dotted-line and dashed-dotted line are the form factor P(q) for the structure factor s=1 and s=0 for iron concentration at 1/10 dilution, respectively.

## 7.4 Conclusions

SAXS, DLS and TEM were used to investigate the interaction between Mms6 and iron ions in solution, to investigate the size and shape change in the iron binding process. It is found that before adding iron ions, the Mms6 protein existed as spherical micelles in solution with the diameter of around 10 nm, which confirmed by DLS, SAXS and TEM. Iron induced the protein structure change in solution, confirmed by SAXS. Large aggregates with sizes larger than 75 nm formed after adding iron ions to the Mms6 solution, indicated by the SAXS data, and DLS and TEM also clearly showed the nano structure size increasing after adding iron ions. The conditions of this study were designed to be identical with the magnetite nanocrystals synthesis in the presence of Mms6 *in vitro*; therefore, it provides direct evidence of Mms6 and iron interaction, and size and shape change information that is important for understanding the Mms6 mineralization mechanism *in vitro* and optimizing the synthesis conditions.

## Acknowledgements

We thank Xiaobin Zuo at beamline 12ID-B of APS for technical support and helpful discussion. Research supported by the U.S. Department of Energy, Office of Basic Energy

Sciences, Division of Materials Sciences and Engineering (X-ray scattering studies). Ames Laboratory is operated for the U.S. Department of Energy by Iowa State University under Contract No. DE-AC02-07CH11358. Use of the Advanced Photon Source, an Office of Science User Facility operated for the U.S. Department of Energy (DOE) Office of Science by Argonne National Laboratory, was supported by the U.S. DOE under Contract No. DE-AC02-06CH11357.

## References

(1) Liu, X.; Mallapragada, S. In *On Biomimetics*; Pramatarova, L., Ed.; InTech, 2011.
(2) Wang, L.; Prozorov, T.; Palo, P. E.; Liu, X.; Vaknin, D.; Prozorov, R.; Mallapragada, S.; Nilsen-Hamilton, M. *Biomacromolecules* **2011**, *13*, 98–105.
(3) Prozorov, T.; Mallapragada, S. K.; Narasimhan, B.; Wang, L.; Palo, P.; Nilsen-Hamilton, M.; Williams, T. J.; Bazylinski, D. A.; Prozorov, R.; Canfield, P. C. *Adv. Funct. Mater.* **2007**, *17*, 951–957.
(4) Prozorov, T.; Palo, P.; Wang, L.; Nilsen-Hamilton, M.; Jones, D.; Orr, D.; Mallapragada, S. K.; Narasimhan, B.; Canfield, P. C.; Prozorov, R. *ACS Nano* **2007**, *1*, 228–233.
(5) Prozorov, T.; Bazylinski, D. A.; Mallapragada, S. K.; Prozorov, R. *Mater. Sci. Eng. R Reports*.
(6) Tanaka, M.; Mazuyama, E.; Arakaki, A.; Matsunaga, T. *J. Biol. Chem.* **2011**, *286*, 6386–6392.
(7) Feng, S.; Wang, L.; Palo, P.; Liu, X.; Mallapragada, S.; Nilsen-Hamilton, M. *Int. J. Mol. Sci.* **2013**, *14*, 14594–14606.
(8) Amemiya, Y.; Arakaki, A.; Staniland, S. S.; Tanaka, T.; Matsunaga, T. *Biomaterials* **2007**, *28*, 5381–5389.
(9) Rambo, R. P.; Tainer, J. A. *Annu. Rev. Biophys.* **2013**, *42*, 415–441.
(10) Petoukhov, M. V.; Svergun, D. I. *Int. J. Biochem. Cell Biol.* **2013**, *45*, 429–437.
(11) Harris, J. R.; Plückthun, A.; Zahn, R. *J. Struct. Biol.* **1994**, *112*, 216–230.
(12) Wang, W.; Bu, W.; Wang, L.; Palo, P. E.; Mallapragada, S.; Nilsen-Hamilton, M.; Vaknin, D. *Langmuir* **2012**, *28*, 4274–4282.

# Chapter 8 Conclusions and future work

## 8.1 Conclusions

A family of self-assembling tri- and pentablock copolymers and their conjugates with biomineralization proteins and peptides were synthesized and used as templates for biomineralization. In aqueous media, these templates can self-assemble into nanoscale micelles or macroscale gels depending on the changes in temperature and pH.

We have focused on bioinspired self-assembling calcium phosphate nanocomposites using self-assembling block copolymers as templates and adding a small amount of citrate to control the nanocrystal size. By using similar concentrations of citrate as seen in native bone, we have successfully produced apatite nanocrystals of similar sizes and morphologies as in natural bone. We have shown that citrate stabilizes HAp over other calcium phosphate species without disturbing the supramolecular structure of the polymer gel. The crystal size of HAp can be fine-tuned on the nanometer scale by varying the citrate concentration, similar to that seen in native bone.

Using a very similar biomineralization method, we synthesized mesoporous zirconia, using the block copolymer- lysozyme conjugate and pentablock copolymer as templates. The mesoporous zirconia synthesized with our templates showed much higher surface area, smaller crystal size, and improved thermal stability, than that synthesized without template. To the best of our knowledge, this is also the first report of synthesis of mesoporous zirconia in completely aqueous media. This will further extend the use of biomolecules and bioinspired method for zirconia synthesis.

We have developed and optimized a novel, room-temperature bioinspired route to synthesis of fairly uniform magnetic nanoparticles *in vitro*, using the recombinant protein, Mms6, found in the

magnetosomes of magnetotactic bacteria. We have investigated the structure and mechanism of action of Mms6. The protein forms micelles in aqueous media, with 20-40 protein units. Mms6 has two phases of ferric iron binding, the first is stoichiometric and very high affinity and the second is low affinity, high capacity, and cooperative with respect to iron. Understanding the behavior of Mms6 is important in using this protein for other magnetic materials synthesis, as well as for developing potential synthetic analogs of the biomineralization proteins.

## 8.2 Future work

Ongoing and future work is focused on magnetic nanocrystal synthesis based on Mms6 and block copolymer templates. In the future, we will continue to use the protein Mms6 to promote shape and size selective synthesis of more complex magnetic materials. As we have successfully synthesized cobalt ferrite in the presence of Mms6 *in vitro*,[1] we will expand our work to synthesis of other magnetic organic-inorganic nanocomposites to explore the bioinspired synthesis of complex multifunctional oxides in the presence of Mms6, such as magnetic materials with included rare earth elements, and manganese ferrite. We will also try to create reversible assembly/disassembly of the magnetic nanocrystals on surfaces, based on the Mms6 mediated synthesis of magnetite nanoparticles. This will enable the formation of tunable and dynamic "smart" structures with different hierarchical structures and magnetic properties in response to different environmental stimuli. The first step in forming the dynamic structures is to find an appropriate surface for the attachment/detachment of protein Mms6, and synthesize magnetite nanoparticles on surfaces.

### 8.2.1 Magnetic metal complex materials

#### 8.2.1.1 Rare earth elements included magnetic materials synthesis

Nanocrystalline rare-earth orthoferrites $LnFeO_3$ (Ln = lanthanide elements) have drawn great attention because of their excellent physical and chemical properties for various applications. These compounds with perovskite structures can be used as catalysts, cathodes in solid oxide fuel cells, sensor materials, magneto-optic materials, and so on.[2,3] These compounds are usually synthesized by heating the corresponding metal oxides in a stoichiometric ratio at relatively high temperatures (600 ˚C to 1000 ˚C).[2] We are exploring the use of the mineralization protein Mms6 and our bioinspired synthesis method to synthesize magnetic materials that include rare earth elements. We hypothesize that Mms6 can help to form magnetic complex materials at relatively low temperatures, with controlled size and shape. We have evidence showing that protein Mms6 can bind the ion $La^{3+}$, especially at higher pH (about 7).[4] We have also explored using gadolinium ions ($Gd^{3+}$) to replace some of the $Fe^{3+}$ ions, and the XRD results showed that the sample with Mms6 shows formation of more gadolinium oxide containing nanocrystals, as shown by Figure 8.1.

Based on the evidence and the initial studies, we will continue to optimize the synthesis conditions for forming magnetic complexes at relatively low temperatures. Figure 8.2 shows the method we used to synthesize magnetite nanoparticles in Chapter 6. Rare-earth elements will bind to Mms6 and precipitate at relatively high pH (about 6-7), while the iron will precipitate at lower pH (about 2-3). The method shown in Figure 8.2 would create a pH gradient, which could cause the separate precipitation of gadolinium and iron ions. In the future, we will use a reverse order of mixing the reagents. Instead of injecting NaOH into the precursor mixture, we will inject the $Ln^{3+}$ and $Fe^{3+}$ ions into the NaOH solution. In this way, we anticipate that the different ions could co-precipitate and form a compound. If necessary, we will heat the reaction system.

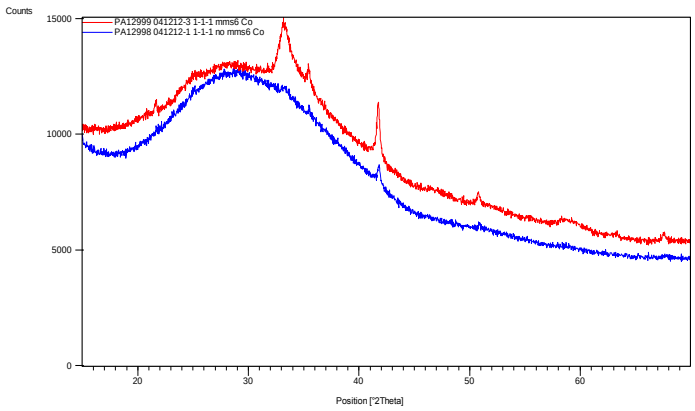


Figure 8.1 XRD of Gd-Fe oxides synthesized at room temperature: with Mms6 (red &top line) and without Mms6 (blue & lower line)

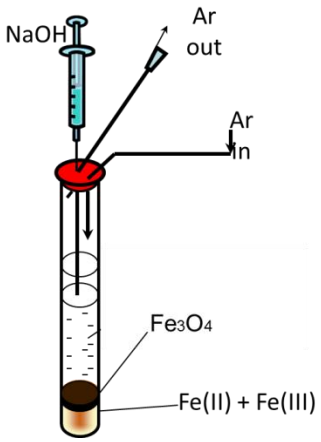


Figure 8.2 Scheme for the method used for synthesis of magnetite in Chapter 6.

### 8.2.1.2 Manganese ferrite synthesis

Spinel-type ferrite nanoparticles ($MFe_2O_4$, where M= Fe, Co, Mn, etc.) have outstanding properties such as large surface area to volume ratio, superparamagnetic behavior, and high saturation magnetization.[5] We have successfully synthesized shape and size selective magnetite

($Fe_3O_4$) and cobalt ferrite ($CoFe_2O_4$) nanocrystals mediated by the mineralization protein Mms6.[1] $MnFe_2O_4$ has been widely used in electronic applications and contrast-enhancement agents in magnetic resonance imaging (MRI) technology.[6] We have successfully synthesized $MnFe_2O_4$ using the bioinspired method we developed before, without the presence of Mms6, as the XRD result shown by Figure 8.3. We will add Mms6 to the synthesis, and try to control the magnetic nanoparticle size and shape.

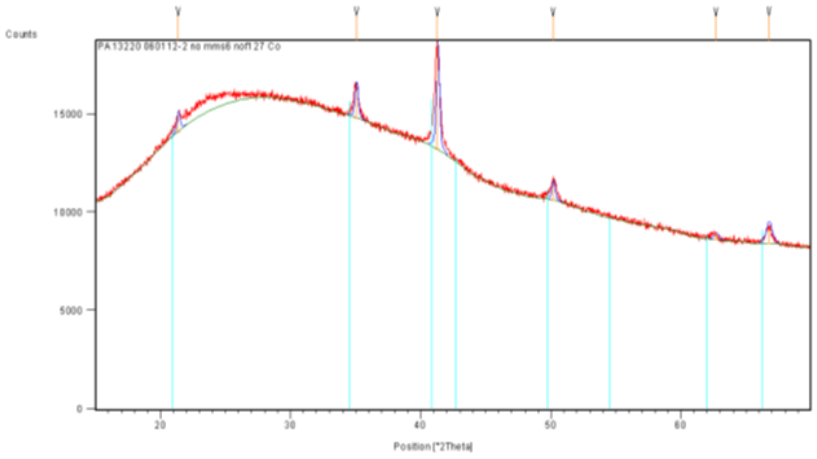


Figure 8.3 XRD of the $MnFe_2O_4$ synthesized without the presence of Mms6

### 8.2.2 Synthesis of magnetite nanoparticles on surfaces

While most of the work on bioinspired synthesis in this doctoral thesis has focused on bulk synthesis, extending these approaches for magnetic nanocrystal synthesis to the surface can allow for control of patterning of nanocrystals on different surfaces and for the development of reversible dynamic nanostructures.

#### 8.2.2.1 Copper coated glass surface

The first kind of surface we chose for Mms6 attachment is a copper coated glass slide (MicroSurfaces, Inc.), shown as Figure 8.4. The Mms6 has a Polyhistidine-tag (his-tag), which is

used for affinity purification of the recombinant Mms6 by nickel column. The copper can bind to the his-tag stronger than nickel. Thus, the Mms6 could be linked to the surface using the his-tag without much interaction with the amino acid sequence of the protein, to help maintain the function of Mms6.

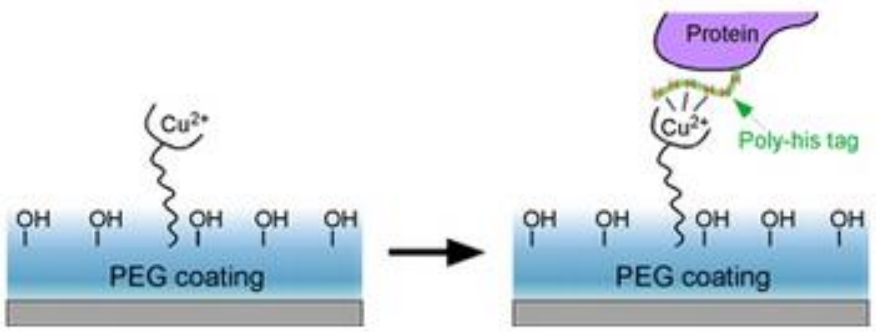


Figure 8.4 Copper coated surface for Mms6 attachment

We have synthesized magnetite on the copper surface with and without protein, and the atomic force microscopy (AFM) images are shown in Figure 8.5. We can see that there are many particles on the surface with protein Mms6, as it can promote the size and shape selective synthesis of magnetite. The protein also acted as glue, binding to the nanoparticles; therefore, the magnetite nanoparticles could not be washed away from the surface.

The future work in this direction will include controlled deposition of the Mms6 protein layer, and characterization of the nanoparticles by TEM and XPS. We can see from Figure 8.5 that the nanoparticles were not uniformly distributed on the surface, which may due to the uncontrolled method of adding the protein solution onto the surface, and due to the micelles formed by Mms6. We will reduce the concentration of the precursor chemicals used in the synthesis of magnetite, as there are too many nanoparticles seen in the left images of Figure 8.5, even after washing. XPS

and TEM techniques will help to confirm the formation, shape and size of the magnetite nanoparticles.

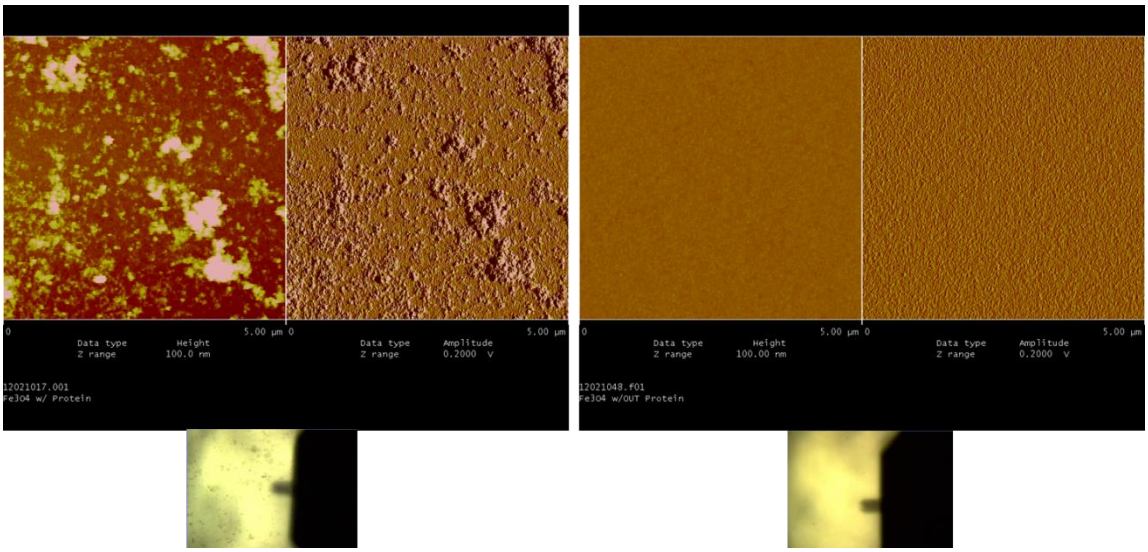


Figure 8.5 AFM images of magnetite synthesized on the copper coated surfaces with the precence of Mms6 (left), and without Mms6 (right). The downside are the bright microscope images taken at the surface. AFM scan size: 5µm×5µm

### 8.2.2.2 Gold coated glass surface

The second kind of surface we chose for attaching the Mms6 is a flat gold surface. Recently, there is increasing research attention paid to using gold as substrate for protein microarrays and microsensors.[7,8] The thiol-gold linkage is widely used to attach proteins and peptides to gold. Our collaborator, Dr. Nilsen-Hamilton, has synthesized two mutants of Mms6, changing the 64$^{th}$ or the 62$^{th}$ amino acid to cysteine, which has an –SH function group for gold linkage. We have used the two mutants in our solution synthesis of magnetite nanoparticles, to ensure that the mutants retain the native protein's function. The TEM images shown in Figure 8.6 show that these mutants generated magnetite nanoparticles very similar to those generated in the presence of the wild type Mms6. Magnetic measurements also led to the same conclusion.

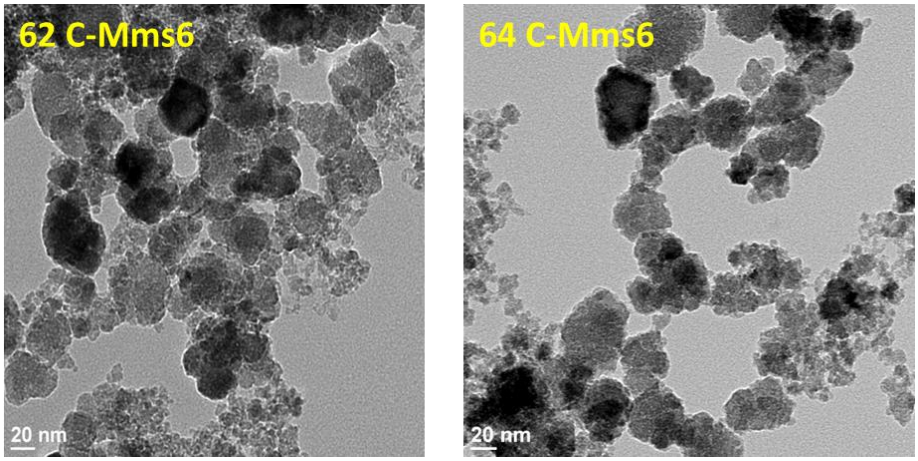


Figure 8.6 TEM images of the magnetite nanoparticles mediated by 62C-Mms6 and 64C-Mms6

In the future, we would first fabricate a flat gold surface, then deposit the –SH mutants to the surface, or deposit a Mms6 protein pattern on the gold surface. The gold coated surface with immobilized Mms6 can be used to create a magnetite nanoparticle layer or a magnetite nanoparticles pattern. To achive the reversible linkage between Mms6 and the gold surface, thiol modified DNA molecules will be used as a reversible linker for the Mms6 attachment/detachment to the DNA surface, as shown by Figure 8.7.[9-12]

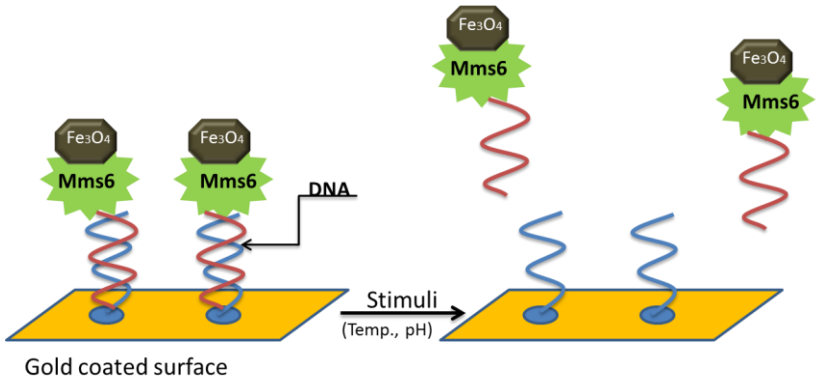


Figure 8.7 DNA as a reversible linker between gold surface and Mms6

Since Mms6 is an amphiphilic membrane protein with a hydrophobic N-terminus and a hydrophilic C-terminal end, we investigated the effect of surface hydrophobicity on Mms6 structure and function on surfaces. We modified the gold surface with 1-octadecanethiol (ODT), which genetarated a very hydrophobic surface. The hypothesis is that the N-terminal groups of Mms6 protein in Nature are embeded in the phosphate lipid bilayer in the memberane, and C-terminals interact with the iron ions and promote the formation of magnetite nanoparticles. Our eailer results also showed that C-terminal is binds iron ions, and is very important for the *in vitro* magnetite growth in the presence of Mms6.[13] We incubated the Mms6 or M2 (a mutant with carboxyl and hydroxyl group switched in the C-terminals of Mms6) on the hydrophilic (gold) or hydrophobic surface (ODT coated gold) overnight under 4 ˚C, and then washing off the excess protein. The M2 has been shown in earlier studies (chapter 6) to not promote the formation of surperparamagnetic magnetite nanocrystals *in vitro* in the bulk, unlikethe wild type Mms6. The proteins were physically adsorpted onto the surface. The magnetite nanoparticles were synthesized on the different kinds of surfaces under aqueous and room temperature conditions.

We can see that Mms6 formed micelles on the hydrophilic gold surface (Figure 8.8 D), very similar to its structure in aqueous solution as we reported before; while it formed larger aggragates, similar to a network on the ODT coated gold surface (Figure 8.8 E). On the ODT coated hydrophobic surface, there might be more interactions between the Mms6 proteins, and the protein may have mobility inside the network. The mutant M2 only formed very small micelles/structures on both the gold and ODT surfaces, which indicated that the original structure and function may have changed in the mutant, and which might suggest the importance of the network structure in the formation of the surperpapramagnetic nanocrystals.

Figure 8.9 shows the AFM images of magnetite formed on different kinds of surfaces. We can see that the magnetite formed in the presence of Mms6 (Figure 8.9 A,B) had larger size than

that without Mms6 (Figure 8.9 C). This confirmed Mms6's function of promoting magnetite growth. Comparing Figures 8.9 A and B, the magnetite nanoparticles formed on the ODT surfaces are larger, which is probably corelated to the Mms6 forming larger protein network on the ODT surface, and this structure being closer to its role as a membrane protein in Nature.

This investigation is very important for further understanding the Mms6 biomineralization mechnism and optimizing the condition of magnetite nanoparticles's formation on surface, and eventually fabricating the patterned magnetic arrays on surfaces.

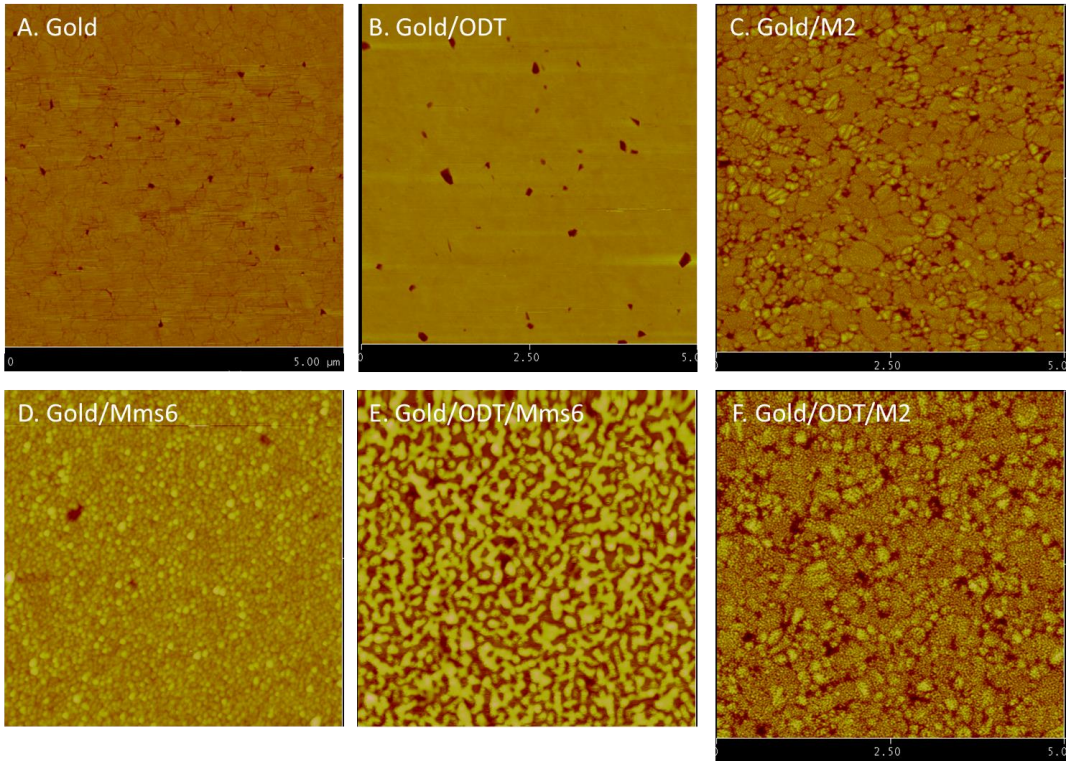


Figure 8.8 AFM images of A) gold surface; B) ODT coated gold surface; C) M2 on gold surface; D) Mms6 on gold surface, scan size 2μm×2μm; E) Mms6 on ODT coated gold surface; F) M2 on ODT coated gold surface. Scan size is 5μm× 5μm for image A), B), C), and F).

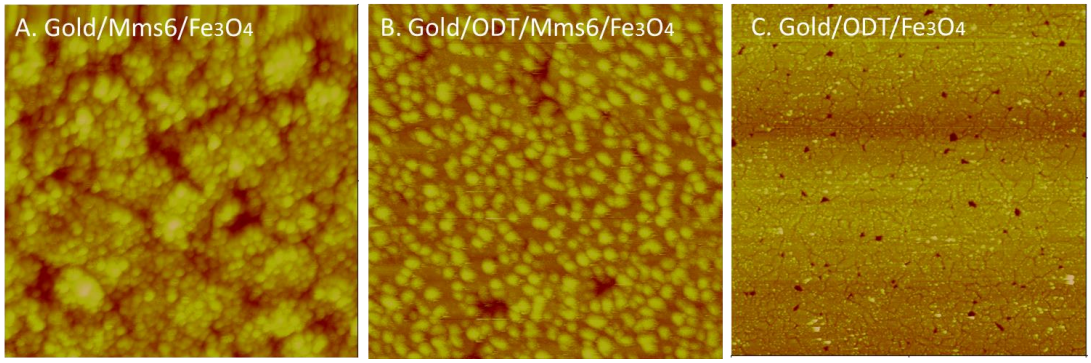


Figure 8.9 AFM images of magnetite nanoparticles synthesized on A) Mms6 coated gold surface; B) Mms6 and ODT coated gold surface; C) ODT coated gold surface

These future studies will therefore focus on the synthesis of complex magnetic materials using the bioinspired approaches, both in bulk as well as the surface. The ability of the magnetic nanocrystals to bind to the Mms6 will be exploited for patterning of magnetic nanocrysals on surfaces using a variety of different linkages. The use of DNA and other linkages will potentially allow for reversible assembly/disassembly of nanoparticles at surfaces, providing dynamic nanostructures.

In summary for this doctoral thesis, we were able to design tailored functional organic templates for room-temperature bioinspired synthesis. We have developed a robust method with control over the formation as well as placement of an inorganic phase in the nanocomposite structure, for a variety of different inorganic nanoparticles, such as calcium phosphate, zirconia and magnetic nanoparticles. The future work will be focused on using biominerlization proteins to create functional dynamic magnetic materials and nanostructures both in solution and on surfaces.

## References


(1) Prozorov, T.; Palo, P.; Wang, L.; Nilsen-Hamilton, M.; Jones, D.; Orr, D.; Mallapragada, S. K.; Narasimhan, B.; Canfield, P. C.; Prozorov, R. Cobalt Ferrite Nanocrystals: Out-Performing Magnetotactic Bacteria. *ACS Nano* **2007**, *1*, 228–233.

(2) Xu, H.; Hu, X.; Zhang, L. Generalized Low-Temperature Synthesis of Nanocrystalline Rare-Earth Orthoferrites LnFeO3 (Ln = La, Pr, Nd, Sm, Eu, Gd). *Crystal Growth & Design* **2008**, *8*, 2061–2065.

(3) Bedekar, V.; Jayakumar, O. D.; Manjanna, J.; Tyagi, A. K. Synthesis and magnetic studies of nano-crystalline GdFeO3. *Materials Letters* **2008**, *62*, 3793–3795.

(4) Wang, W.; Bu, W.; Wang, L.; Palo, P. E.; Mallapragada, S.; Nilsen-Hamilton, M.; Vaknin, D. Interfacial Properties and Iron Binding to Bacterial Proteins That Promote the Growth of Magnetite Nanocrystals: X-ray Reflectivity and Surface Spectroscopy Studies. *Langmuir* **2012**, *28*, 4274–4282.

(5) Pereira, C.; Pereira, A. M.; Fernandes, C.; Rocha, M.; Mendes, R.; Fernández-García, M. P.; Guedes, A.; Tavares, P. B.; Grenèche, J.-M.; Araújo, J. P.; Freire, C. Superparamagnetic MFe2O4 (M = Fe, Co, Mn) Nanoparticles: Tuning the Particle Size and Magnetic Properties through a Novel One-Step Coprecipitation Route. *Chem. Mater.* **2012**.

(6) Zhang, D.; Zhang, X.; Ni, X.; Song, J.; Zheng, H. Low-temperature fabrication of MnFe2O4 octahedrons: Magnetic and electrochemical properties. *Chemical Physics Letters* **2006**, *426*, 120–123.

(7) Kenseth, J. R.; Harnisch, J. A.; Jones, V. W.; Porter, M. D. Investigation of Approaches for the Fabrication of Protein Patterns by Scanning Probe Lithography. *Langmuir* **2001**, *17*, 4105–4112.

(8) O'Brien, J. C.; Stickney, J. T.; Porter, M. D. Self-Assembled Double-Stranded DNA (dsDNA) Microarrays for Protein:dsDNA Screening Using Atomic Force Microscopy. *J. Am. Chem. Soc.* **2000**, *122*, 5004–5005.

(9) Zhou, X.; Xia, S.; Lu, Z.; Tian, Y.; Yan, Y.; Zhu, J. Biomineralization-Assisted Ultrasensitive Detection of DNA. Journal of the American Chemical Society 2010, 132, 6932–6934.

(10) Lockett, M. R.; Weibel, S. C.; Phillips, M. F.; Shortreed, M. R.; Sun, B.; Corn, R. M.; Hamers, R. J.; Cerrina, F.; Smith, L. M. Carbon-on-Metal Films for Surface Plasmon Resonance Detection of DNA Arrays. J. Am. Chem. Soc. 2008, 130, 8611–8613.

(11) Müller, J.; Niemeyer, C. M. DNA-directed assembly of artificial multienzyme complexes. Biochem. Biophys. Res. Commun. 2008, 377, 62–67.

(12) Zhang, J.; Liu, Y.; Ke, Y.; Yan, H. Periodic Square-Like Gold Nanoparticle Arrays Templated by Self-Assembled 2D DNA Nanogrids on a Surface. Nano Letters 2006, 6, 248–251.

(13) Wang, L.; Prozorov, T.; Palo, P. E.; Liu, X.; Vaknin, D.; Prozorov, R.; Mallapragada, S.; Nilsen-Hamilton, M. Biomacromolecules 2011, 13, 98–105.